INFORMATION TO USERS

This manuscript has been reproduced from the microfilm master. UMI films the text directly from the original or copy submitted. Thus, some thesis and dissertation copies are in typewriter face, while others may be from any type of computer printer.

The quality of this reproduction is dependent upon the quality of the copy submitted. Broken or indistinct print, colored or poor quality illustrations and photographs, print bleedthrough, substandard margins, and improper alignment can adversely affect reproduction.

In the unlikely event that the author did not send UMI a complete manuscript and there are missing pages, these will be noted. Also, if unauthorized copyright material had to be removed, a note will indicate the deletion.

Oversize materials (e.g., maps, drawings, charts) are reproduced by sectioning the original, beginning at the upper left-hand corner and continuing from left to right in equal sections with small overlaps.

Photographs included in the original manuscript have been reproduced xerographically in this copy. Higher quality 6" x 9" black and white photographic prints are available for any photographs or illustrations appearing in this copy for an additional charge. Contact UMI directly to order.

ProQuest Information and Learning
300 North Zeeb Road, Ann Arbor, MI 48106-1346 USA
800-521-0600

High-Resolution Surface Plasmon Resonance Biosensing

Garet Glenn Nenninger

A dissertation submitted in partial fulfillment of the requirement for the degree of

Doctor of Philosophy

University of Washington

2001

Program Authorized to Offer Degree: Department of Electrical Engineering

In presenting this dissertation in partial fulfillment of the requirements for the Doctoral degree at the University of Washington, I agree that the Library shall make its copies freely available for inspection. I further agree that extensive copying of the dissertation is allowable only for scholarly purposes, consistent with "fair use" as prescribed in the U.S. Copyright Law. Requests for copying or reproduction of this dissertation may be referred to Bell and Howell Information and Learning, 300 North Zeeb Road, Ann Arbor, MI 48106-1346, to whom the author has granted "the right to reproduce and sell (a) copies of the manuscript in microform and/or (b) printed copies of the manuscript made from microform."

Signature Janet Glenn Hennings

Date 12 August 2001

University of Washington
Graduate School

This is to certify that I have examined this copy of a doctoral dissertation by

Garet Glenn Nenninger

and have found that it is complete and satisfactory in all respects,
and that any and all revisions by the final
examining committee have been made.

Chairs of the Supervisory Committee:

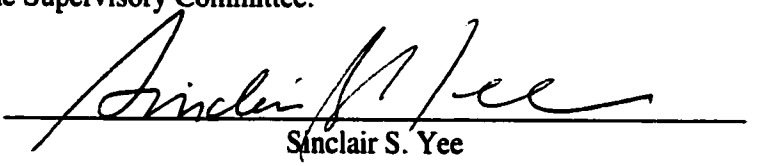

Sinclair S. Yee

Jiří Homola

Reading Committee:

Karl F. Böhringer

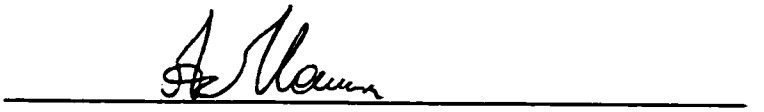

Alexander V. Mamishev

Date: 1 August 2001

University of Washington

Abstract

High-Resolution Surface Plasmon Resonance Biosensing

Garet Glenn Nenninger

Chairs of the Supervisory Committee:
Professor Sinclair S. Yee
Research Associate Professor Jiří Homola

Department of Electrical Engineering

Surface plasmon resonance (SPR) sensors are optically-interfaced devices that detect the refractive index of a thin layer of analyte in contact with the sensor surface. For biosensing applications such as food toxin or biological warfare agent detection, high-resolution detection of the target species provides an improvement in the detection limit of the SPR sensor.

We present the design, modeling, and implementation of an improved SPR biosensor based on long-range surface plasma wave (LRSPW) spectroscopy. An LRSPW consists of two surface plasma waves coupled across a thin metal layer. The LRSPW has lower attenuation than a single surface plasma wave, producing a narrower absorption minimum in the sensor spectral response. This narrower minimum results in improved resolution due to reduced uncertainty in the position of the minimum.

Theoretical design curves presented for an LRSPW sensor using a Teflon AF buffer layer and gold metal layer show that the sensor can have sensitivity as high as 1×10^{5} nm RIU^{-1}, an order of magnitude or more improvement over conventional SPR sensors. Results of a biosensing experiment conducted with the LRSPW sensor showed a resonance width of only 15 nm (full-width at half-minimum), a sensitivity of 3.1×10^{4} nm RIU^{-1}, and a corresponding resolution of 1.9×10^{-7} RIU. Compared

with a similar experiment conducted using a conventional SPR sensor, the LRSPW sensor had 25 times better resolution.

To further improve the resolution of SPR sensor systems, we also present methods for evaluating the performance of data-processing algorithms for analyzing SPR spectra, including a method for predicting the instrument resolution based on measured system and detector noise. A new interpolated tracking centroid data-processing algorithm is presented, and its performance in terms of resolution, linearity, and resistance to environmental drift is shown to be superior to that of a simple centroid algorithm.

TABLE OF CONTENTS

LIST OF FIGURES

LIST OF TABLES

ACKNOWLEDGMENTS

This research was supported by the United States Department of Defense under contract DAAD13-99-C-0032 and by the Center for Process Analytical Chemistry, University of Washington under grant 66-9938.

I would like to acknowledge my family for their continued support and encouragement: Lisette, Brendan, Garet L. and Kathleen Nenninger, and Anthony and Maria Lambregts.

My appreciation goes to my advisors, Prof. Jiří Homola and Prof. Sinclair Yee, and to the members of my committee. Many thanks to those at I have worked with directly during the course of my research. At the University of Washington: Christina Boozer, Dr. Tai Chen, Prof. Timothy Chinowsky, Prof. Clem Furlong, Scott Jorgensen-Soelberg, Dr. Hongbo Lu, Mimi Mar, Dr. Alexei Naimushin, and Thomas Notides. At the Institute of Radio Engineering and Electronics, Prague, Czech Republic: Jakub Dostálek, Marek Piliarik, and Petr Tobiška.

I give a note of gratitude to my grade school and high school teachers, especially: Terry Brandhorst (chemistry), Calvin Kaneshiro (general science, marine science, and master of the science fair project), Linda Rawlings (English), and Elsie Tanaka (English). With you, I had a running start.

And special thanks to those who served as mentors in other ways: Prof. Dr. Durk van Willigen of Reeuwijk in South Holland, and Irish author and explorer Tim Severin, whose books gave me a refreshing and necessary escape.

Chapter 1: Introduction to Surface Plasmon Resonance

Surface plasmon resonance (SPR) is an optically-based phenomenon which has an important application in evanescent wave sensing. SPR sensors have been used for a variety of physical, chemical, and biological sensing applications. However, the majority of published SPR sensing papers involve optically-based biosensing [1].

Since the first application of surface plasmon resonance to biosensing in 1983 [2], the use of surface plasmon resonance sensors has expanded greatly. In 1999 alone, nearly a thousand articles reported data collected using SPR sensors [3]. SPR sensors have become the prevalent sensor for the measurement of kinetic and equilibrium constants in biomolecular interaction studies.

The primary advantage of SPR sensors over other biosensor technologies is the real-time measurement of unlabeled binding reactions. Unlike fluorescent and radio-labeled biomolecular interaction assays, the binding reaction is detected directly and in solution by measuring the refractive index change caused by molecular receptors in solution binding to ligand immobilized on the sensor surface [4].

Because SPR detects the bound molecules directly, there is a lower limit to the size and concentration of directly-detectable molecules. However, recent advances in SPR sensor technology have allowed the direct detection of molecules with molecular weights as low as 200 Daltons [5, 6]. Further improvements in the instrument resolution of SPR biosensors therefore have direct impact on current SPR biosensing applications.

Biosensing applications fall into two major categories: 1) the study of biomolecules and biomolecular interaction analysis (BIA), and 2) biological analyte detection applications. Biomolecular interaction analyses include kinetic studies of binding interactions, drug discovery, epitope mapping, and protein studies. BIA experiments represent the bulk of SPR literature, largely because surface plasmon

resonance sensors are the primary means for conducting such studies [7]. Detection applications represent an emerging field for SPR sensors. The unlabeled real-time detection of target species provided by SPR sensors has led to many detection applications, including: immunoglobulins, proteins, toxins, drugs, allergens, viruses, DNA, and bacteria [8].

Recent concern over food safety and biological warfare agents have created the need for sensors which can detect low concentrations of biological agents rapidly and accurately. Surface plasmon resonance sensors are one of a few methods being developed for these applications.

Commercial SPR sensor platforms include: the BIACORE series (Biacore AB, Uppsala, Sweden), IBIS (Intersens Instruments, Amersfoort, Netherlands), SPR-670 (Nippon Laser and Electronics Laboratory, Hokkaido, Japan), and Spreeta (Texas Instruments, Dallas, TX, USA). Of these, the Biacore sensors are most frequently cited in literature, with ninety percent of 1999 SPR biosensor papers [3]. However, the Biacore platforms are large units designed for laboratory applications. There is currently growing interest in the development of field-use SPR biosensors for the emerging applications of food safety and biological warfare agent detection.

A primary goal of biosensors proposed for food safety and biological warfare detection applications is the rapid detection of low concentrations of the agents. The detection limit of SPR biosensors is constrained in part by the affinity of the antibodies or recognition elements, and ultimately by the noise-based resolution of the SPR instrument itself. Therefore, improving the resolution of SPR biosensors is vital for reducing the detection limit.

In this dissertation, we present two methods for improving the resolution of SPR biosensors: through the use of long-range surface plasma waves as a transduction mechanism, and the use of improved data-analysis algorithms. Long-

range surface plasma waves have only recently been used for sensor applications [9], and this work represents their first application to biosensing.

Notes for Chapter 1

[1] J. Homola, S.S. Yee, G. Gauglitz, Surface plasmon resonance sensors: review, Sensors and Actuators B 54 (1999) 3-15.

[2] B. Liedberg, C. Nylander, I. Lundström, Surface plasmon resonance for gas detection and biosensing, Sensors and Actuators 4 (1995) 299-304.

[3] R.L. Rich, D.G. Myszka, Survey of the 1999 surface plasmon resonance biosensor literature, Journal of Molecular Recognition 13 (2000) 388-407.

[4] D.G. Myzka, R.L. Rich, Implementing surface plasmon resonance biosensors in drug discovery, Pharmaceutical Science and Technology Today 3 (2000) 310-317.

[5] D.G. Myszka, Kinetic analysis of macromolecular interactions using surface plasmon resonance biosensors, Current Opinions in Biotechnology 8 (1997) 50-57.

[6] R. Karlsson, R. Stahlberg, Surface Plasmon Resonance Detection and Multispot Sensing for Direct Monitoring of Interactions Involving Low-Molecular-Weight Analytes and for Determination of Low Affinities, Analytical Biochemistry 228 (1995) 274-280.

[7] D.G. Myszka, Survey of the 1998 optical biosensor literature, Journal of Molecular Recognition 12 (1999) 390-408.

[8] W.M. Mullet, E.P.C. Lai, J.M. Yeung, Surface Plasmon Resonance-Based Immunoassays, Methods 22 (2000) 77-91.

[9] G.G. Nenninger, P. Tobiška, J. Homola, S.S. Yee, Long-range surface plasmons for high-resolution surface plasmon resonance sensor, Sensors and Actuators B 74 (2001) 145-151.

Chapter 2: Theory and Implementation of Surface Plasmon Resonance Sensors

2.1 Surface Plasmon Resonance Theory

An understanding of the electromagnetic basis for surface plasmon resonance is needed for predicting and understanding the behavior of surface plasma waves in sensor design.

2.1.1 Plasma Theory

The electrons within a metal may be thought of as a plasma with a plasma frequency, ω_p, given by the equation [1]:

$$\omega_p = \sqrt{\frac{4\pi N q^2}{m\varepsilon_0}} \tag{2.1}$$

where q is the electron charge, N is the electron density, m is the mass of the electron, and ε_0 is the permittivity of free space. In turn, the plasma dielectric constant of the electron gas in a metal as a function of frequency, ω, in the collisionless case, is described by the relationship [2]:

$$\varepsilon_p(\omega) = 1 - \frac{\omega_p^2}{\omega^2} \tag{2.2}$$

Below the plasma frequency, the refractive index is complex and a plane wave decays exponentially in the metal. However, above the plasma frequency, the refractive index becomes largely real and positive, and an electromagnetic wave can propagate through the metal. The plasma frequency for metals typically occurs in the

ultraviolet region, so this phenomenon is termed the ultraviolet transparency of metals [3].

2.1.2 Electromagnetic Theory of Surface Plasmons

A surface plasmon is a collective charge-density oscillation which may exist at the interface between a metal and a dielectric. Conduction electrons in metal are able to move freely through the metal lattice and may at times move away from the surface of the metal due to their kinetic energy. When an electron moves away from the surface, a restoring force caused by the altered charge distribution in the lattice acts to pull the electron back into the lattice. The average motion of the electrons at the surface normal to the surface occurs at a quantized frequency, analogous to a harmonic oscillator.

A surface plasma wave (SPW) is a nonradiative transverse magnetic (TM) solution (so that the magnetic field vector is parallel to the surface, perpendicular to the direction of propagation) to Maxwell's equations at the interface between a material with a negative real component of permittivity (typically a metal) and a dielectric with a positive real permittivity [4]. The SPW propagates along the interface and exponentially decays into both media in a direction perpendicular to the interface. The propagation constant, β, of the SPW is given by:

$$\beta = k_o \sqrt{\frac{\varepsilon_d \varepsilon_m}{\varepsilon_d + \varepsilon_m}} \tag{2.3}$$

where k_o is the free space wave number (the angular frequency ω divided by the speed of light in vacuum), ε_d is the permittivity of the dielectric, and ε_m is the permittivity of the metal.

To use surface plasmons in a sensor, the surface plasma wave must be optically interrogated, which means that the wave vector of the interrogating light

must be matched to the surface plasma wave vector. The dispersion relationship for $\kappa_{z,SPW}$, the wave vector component of a surface plasma wave propagating in the z direction along the interface between the metal and dielectric regions is equal to the real part of the SPW propagatioin constant, β, and is given by:

$$\begin{aligned} \kappa_{z,SPW} &= \mathrm{Re}[\beta] \\ &= \mathrm{Re}\left[k_o\sqrt{\frac{\varepsilon_d\varepsilon_m}{\varepsilon_d+\varepsilon_m}}\right] \end{aligned} \tag{2.4}$$

In order to transfer energy from interrogation light to a surface plasma wave, the illuminating electromagnetic wave must have the same energy, and the same momentum, $p_z = \hbar\kappa_z$, as the plasmon. Therefore, the real wave vector components κ_z and $\kappa_{z,SPW}$ must be equal. Furthermore, since $\kappa_{z,SPW}$ must have a real component for a surface plasma wave to exist, it follows from Eq. (2.4) that the optical properties of the metal must satisfy the condition $\mathrm{Re}(\varepsilon_m) < -\mathrm{Re}(\varepsilon_d)$. Metals which meet this condition in the visible region include gold, silver, copper, and aluminum.

Light incident on the metal-dielectric interface from the dielectric will have a wave vector with a z-component given by:

$$\kappa_{z,light} = k_o\sqrt{\varepsilon_d}\sin\theta \tag{2.5}$$

where θ is the incident angle, measured normal to the surface. An illustration of this wave vector matching between the incident light and the surface plasma wave is provided in Fig. 2.1

As shown in Fig. 2.2, the wave number or momentum of the surface plasma wave will always be higher than that of an optical wave incident from the dielectric. Therefore, there is no method for direct optical excitation of a surface plasma wave on a smooth planar surface. However, it is possible to increase the momentum of the optical wave by using an attenuated total reflection (ATR) prism, a waveguide, or a

diffraction grating. The ATR prism is the prevalent SPR sensor geometry, and so will be discussed here.

2.2 Attenuated Total Reflection Geometries for Surface Plasmon Resonance Detection

Since it is not possible to couple optically to a surface plasma wave on a planar surface directly, two main ATR geometries have been developed which use a higher refractive index material to match the optical wave vector to that of the plasma wave. These two geometries are the Otto configuration and the Kretschmann configuration. As with other ATR applications, the surface plasmon resonance appears as an attenuated reflection.

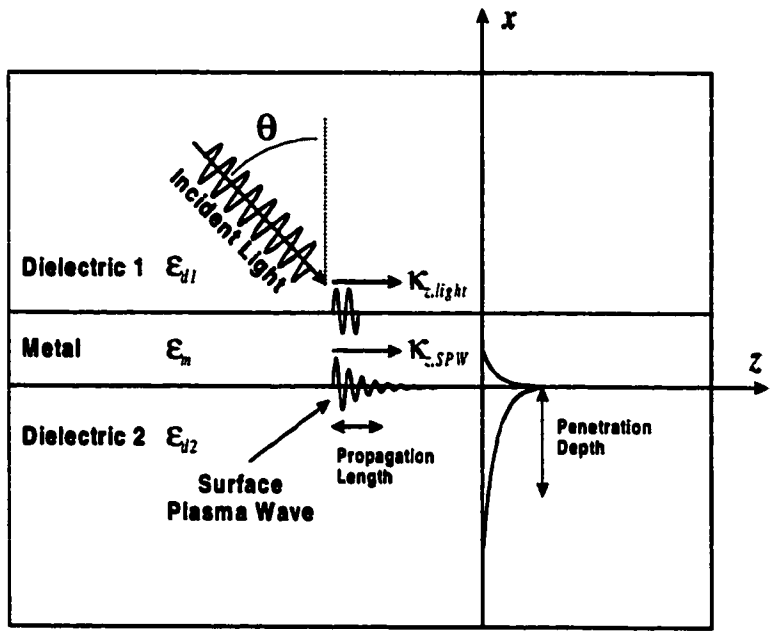

Fig. 2.1. Wave vector matching between incident light and a surface plasma wave.

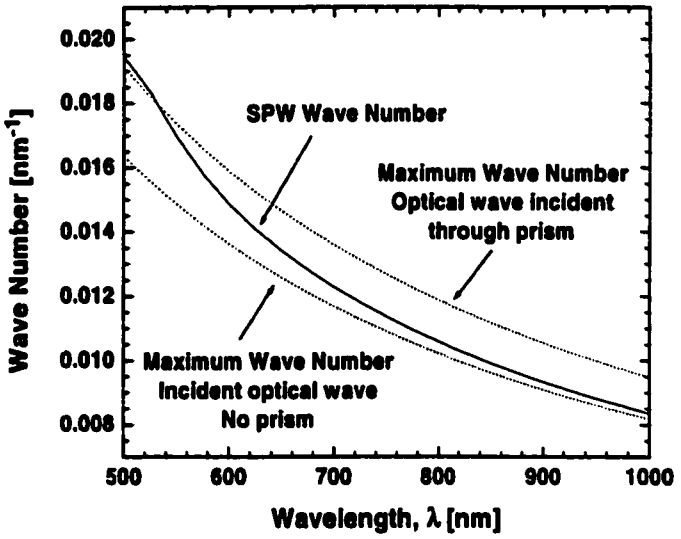

Fig. 2.2. Matching the wave number of a surface plasma wave (SPW) with that of an incident optical wave using a prism. Without a prism, the optical wave number can never be high enough to match the SPW. Adding a prism increases the wave number of the incident light so that a component of the light can couple with the SPW for some incident angles. Figure shows: BK7 glass, gold metal layer, $n = 1.3$ analyte.

2.2.1 Otto Configuration

In 1968, Andreas Otto developed the first technique for optically exciting a surface plasma wave on a smooth surface [4]. This configuration, commonly referred to as the Otto configuration or Otto geometry, uses a prism to create a total internal reflection of the incident light beam within the prism, as illustrated in Fig. 2.3. The prism is separated from the metal by a thin gap of low-index material, typically air or vacuum. At the prism-air interface, an evanescent wave penetrates across the air gap to excite a surface plasma wave at the air-metal interface.

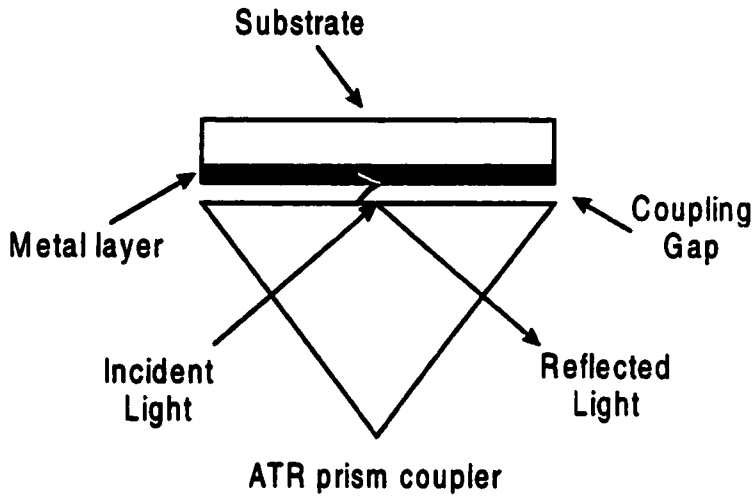

Fig. 2.3. Otto configuration for optically exciting a surface plasma wave.

As the size of the gap increases, the coupling from the prism to the metal surface decreases, so that the resonance depth also decreases. However, if the gap is too small, then the plasma wave emits light back into the prism, causing a higher reflectivity at the resonance minimum. For visible light, the optimum gap is on the order of 500 nm.

2.2.2 Kretschmann Configuration

Kretschmann made a fundamental change to the Otto configuration when he realized that the metal itself could provide the coupling gap required to transfer energy from the incident light to the surface plasma wave via an evanescent wave [5, 6]. As shown schematically in Fig. 2.4, the air gap of the Otto configuration has been replaced with a thin layer of metal in the Kretschmann configuration. Evanescent waves created at the prism-metal interface penetrate the metal film to excite a surface plasma wave at the metal-dielectric interface. A clear advantage of the Kretschmann configuration is that the sensing surface now faces away from the prism and optics, so that sensor configurations are now possible.

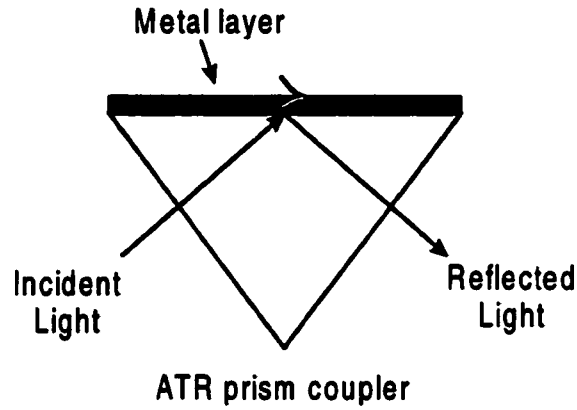

Fig. 2.4. Kretschmann configuration for optically exciting a surface plasma wave.

The metal film thickness for the Kretschmann configuration must be chosen carefully in order to obtain efficient optical coupling to the surface plasma wave. Since the electric field of the energy penetrating the metal film decays exponentially in a direction perpendicular to the interface, the interaction strength is a function of the metal layer thickness. However, if the metal film is too thin, then the interaction will be too strong and some of the optical energy will be reradiated rather than absorbed by the surface plasma wave, resulting in higher reflectivity at the surface plasmon resonance minimum.

2.3 Surface Plasmon Resonance Sensors

Surface plasmon resonance sensors are ideal for many sensing applications because they are sensitive to the refractive index of a thin layer of dielectric material in contact with the surface of the sensor. The ability to couple optically to a surface plasma wave provides a method for interrogating an SPR sensor using a variety of optical techniques.

2.3.1 Surface Sensitivity

The electromagnetic field of a surface plasma wave is highly concentrated in the dielectric and has a penetration depth on the order of 400 nm into the dielectric for a wavelength of 800 nm, making a surface plasmon resonance sensor surface sensitive [7]. SPR sensors are therefore ideal for thin-film measurements. Specificity of detection is provided by a functionalizing layer applied to the surface of the SPR sensor. The functionalizing layer is designed to bind specifically to the target species, thereby increasing the refractive index of the analyte in the vicinity of the sensor surface.

2.3.2 Surface Plasmon Resonance Detection

The TM-polarized reflectivity of an SPR sensor chip is a function of both incident angle and wavelength, so that there are many combinations of these parameters which transfer energy from the incident optical beam to the surface plasma wave. The TM-polarized reflectivity for an SPR sensor is shown in Fig. 2.5 for various combinations of incident angle and wavelength.

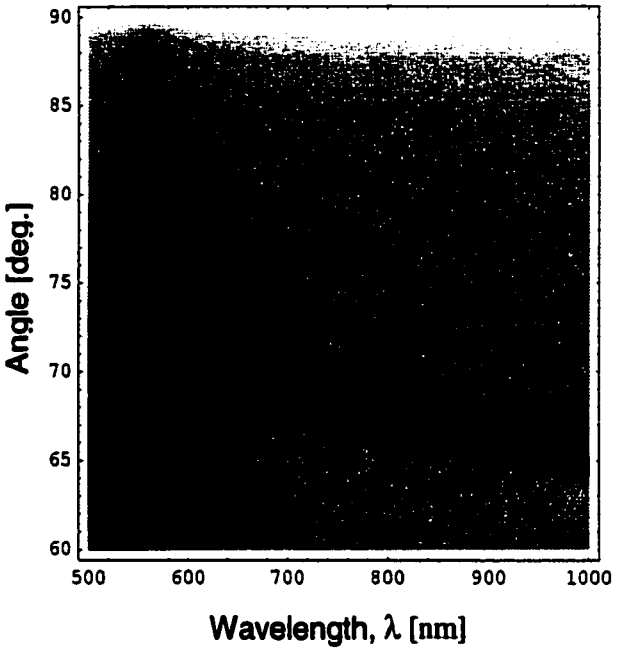

Fig. 2.5. TM-polarized reflectivity for an SPR sensor for various angles and wavelengths. Dark areas indicate low reflectivity, hence transfer of energy from the incident optical beam to the surface plasma wave. Sensor configuration: BK7 glass, 2 nm chromium, 50 nm gold, water.

The most common methods of detection for SPR sensors are wavelength [8] and angular [9] detection. Many early SPR sensors used intensity [10] detection because of its simplicity, but the limitations of this method in terms of signal-to-noise ratio have limited its application. Recently, SPR sensor systems have been made using phase [11, 12] and polarization [13] detection of the SPR. Theoretical plots of the reflection spectra for a wavelength-modulated SPR sensor and an angle-modulated SPR sensor are provided in Fig. 2.6 and Fig. 2.7, respectively.

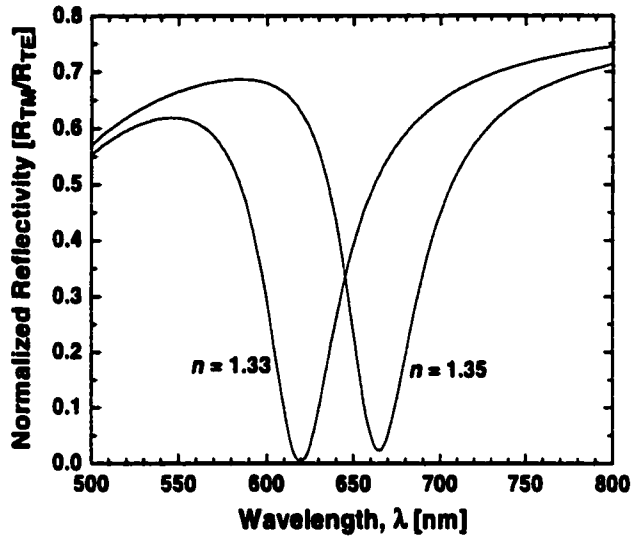

Fig. 2.6. Wavelength detection of surface plasmon resonance. Predicted detection for a sensor consisting of BK7 glass, 2 nm chromium, 50 nm gold, analyte. Incident angle is 72 degrees.

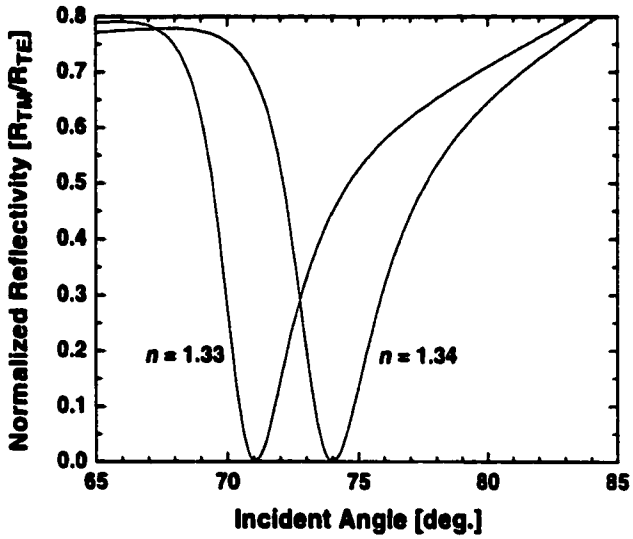

Fig. 2.7. Angular detection of surface plasmon resonance. Predicted detection for a sensor consisting of BK7 glass, 2 nm chromium, 50 nm gold, analyte. Operating wavelength is 633 nm.

For practical implementations of SPR sensors, the metal layer is deposited on a replaceable glass substrate rather than directly on the TIR prism. The sensor chip, comprising the substrate and metal active surface, is index-matched to the TIR prism using index match fluid, gel, or other material. The use of removable sensor chips allows the sensor surface to be easily replaced between experiments. A figure showing this configuration is provided in Fig. 2.8.

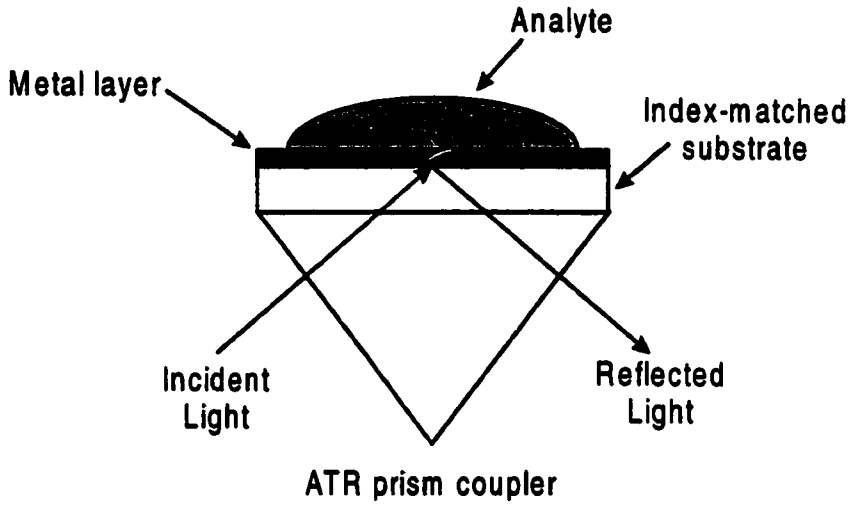

Fig. 2.8. Practical implementation of an SPR sensor, using an index-matched replaceable sensor chip.

2.4 Terminology

For consistency, we will define the following terms used throughout the text:

resonance width: the full width of the SPR minimum in the reflection spectrum, as measured at the half-minimum (FWHM), in units of the measurement parameter (typically angle or wavelength). See Fig. 2.9.

resonance depth: the lowest value of the normalized TM-polarized reflectivity at full resonance. See Fig. 2.9.

sensitivity: the change in the position of the resonance for a given change in the refractive index of the analyte, usually defined for a bulk change in

refractivity. Units are in measured parameter per refractive index change. See Fig. 2.9.

resolution: the smallest resolvable change in the measurement parameter, usually determined by the standard deviation of the data (units of the measurement parameter). Resolution expressed in refractive index units is useful for comparing different SPR sensor systems; this may be calculated by dividing the resolution in measurement parameter units (*e.g.*, resonant wavelength) by the sensitivity.

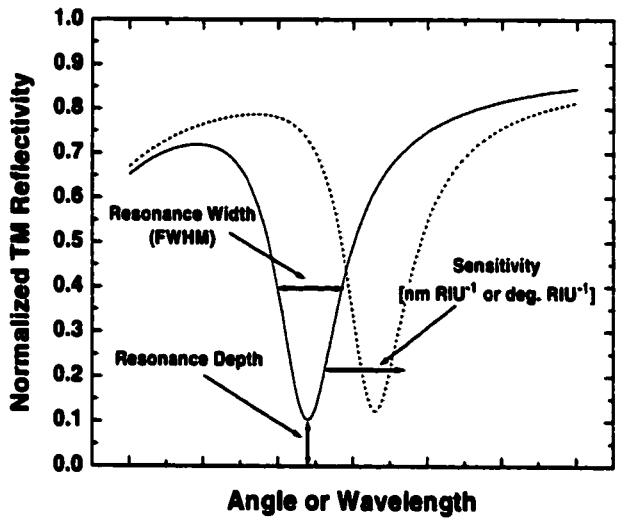

Fig. 2.9. Illustration of SPR resonance width, resonance depth, and sensitivity.

Notes for Chapter 2

[1] J.I. Pankove, Optical Processes in Semiconductors, Dover Publications, New York, 1985.

[2] E. Hecht, Optics, Addison-Wesley Publishing Company, Reading, MA, 1987.

[3] J.D. Jackson, Classical Electrodynamics, Wiley, New York, 1975.

[4] A. Otto, Excitation of nonradiative surface plasma waves in silver by the method of frustrated total reflection, Zeitschrift für Physik 216 (1968) 398-410.

[5] E. Kretschmann, H. Raether, Radiative decay of non-radiative surface plasmons excited by light, Zeitschrift für Naturforsch 23A (1968) 398-410.

[6] E. Kretschmann, Die bestimmung optisher konstanten von metallen durch anregung von oberflächenplasmaschwingungen, Zeitschrift für Physik 241 (1971) 313-324.

[7] J. Homola, S.S. Yee, G. Gauglitz, Surface plasmon resonance sensors: review, Sensors and Actuators B 54 (1999) 3-15.

[8] R.C. Jorgenson, S.S. Yee, A fiber-optic chemical sensor based on surface plasmon resonance, Sensors and Actuators B 12 (1993) 213-220.

[9] K. Matsubara, S. Kawata, S. Minami, Optical chemical sensor based on surface plasmon measurement, Applied Optics 27 (1988) 1160-1163.

[10] C. Nylander, B. Liedberg, T. Lind, Gas detection by means of surface plasmon resonance, Sensors and Actuators 3 (1982) 79-88.

[11] S.G. Nelson, K.S Johnston, S.S. Yee, High sensitivity surface plasmon resonance sensor based on phase detection, Sensors and Actuators B 35, (1996) 187-191.

[12] P.I. Nikitin, A.A. Belaglazov, V.E. Kochergin, M.V. Valeiko, T.I. Kzenevich, Surface plasmon resonance interferometry for biological and chemical sensing, Sensors and Actuators B 54 (1999) 43-50.

[13] A.A. Kruchinin, Y.G. Vlasov, Surface plasmon resonance monitoring by means of polarization state measurement in reflected light as the basis of a DNA probe biosensor, Sensors and Actuators B 30 (1996) 77-80.

Chapter 3: Long-Range Surface Plasma Wave Sensors

A long-range surface plasma wave (LRSPW) consists of coupled surface plasma waves existing on opposite sides of a thin metal film suspended between two dielectrics [1]. The attenuation of an LRSPW can be one or more orders of magnitude lower than that of a conventional surface plasma wave (SPW). For sensor applications, this reduced attenuation causes a decrease in the width of the resonance minimum detected in the reflected spectrum, thereby reducing the uncertainty of the position of the resonance and improving the resolution of the sensor. As an added benefit, the LRSPW dispersion is closer to that of water, resulting in higher sensitivity than the equivalent conventional SPR sensor operating at the same wavelength.

Long-range surface plasma waves have been observed experimentally [2] and several potential applications have been described. These applications include electro-optic modulators [3, 4, 5] and nonlinear optics [6]. However, there have been few successful attempts to create a sensor based on the use of an LRSPW. Matsubara *et al.* presented experimental verification of an angle-modulated version of an LRSPW-based sensor in 1990 [7], but there was no reported work involving wavelength-modulated LRSPW-based sensors prior to the publication of our work in 2001 [8].

3.1 Long-Range Surface Plasma Wave Theory

If a thin metal layer surrounded by dielectric and supporting a surface plasma wave on both surfaces is made thin enough, the two surface plasma waves will couple and exhibit more complex coupled behavior. Specifically, the effective refractive index of the single surface plasma wave splits into two bound eigenmodes as the metal thickness decreases, as illustrated in Fig. 3.1. These two eigenmodes have symmetric and antisymmetric bound magnetic field profiles, as seen in the field

profiles of Fig. 3.2. These modes are characterized by low (symmetric) and high (antisymmetric) losses, and are referred to as "long-range" and "short-range" surface plasma waves, a reference to their relative propagation lengths [9]. The longer propagation length of the long-range surface plasma wave reduces the width of its absorption minimum when an LRSPW-based sensor is used in a total internal reflection configuration.

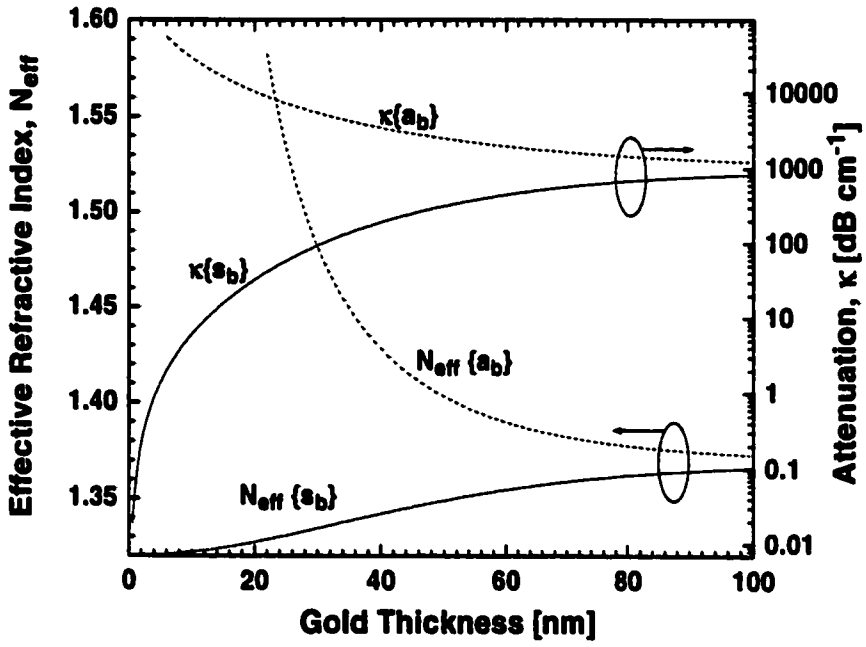

Fig. 3.1. Behavior of coupled surface plasma waves as metal thickness varies. Both symmetric bound (s_b) and antisymmetric bound (a_b) modes are supported. Note the drop in attenuation for the symmetric bound (long-range) mode as the metal thickness decreases. Calculated for a wavelength of 800 nm, with a gold layer bound on both sides with dielectric of n = 1.32. Figure courtesy J. Homola.

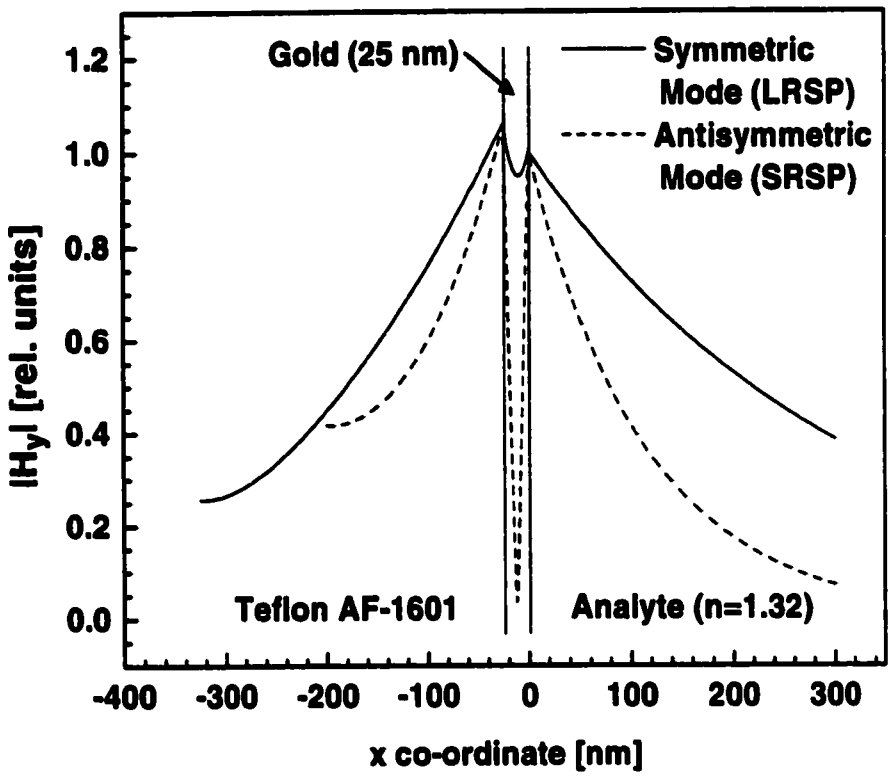

Fig. 3.2. Modulus of the complex magnetic field profile (magnetic field component in the plane of the interface, perpendicular to the direction of SPW propagation) for symmetric and antisymmetric bound surface plasma waves on a 25 nm thick gold layer. (symmetric mode structure: SF14 prism, 300 nm Teflon AF 1601, 25 nm gold, n = 1.32 analyte; 531 nm light, θ = 49.5 deg., antisymmetric mode structure: SF14 prism, 175 nm Teflon AF 1601, 25 nm gold, n = 1.32 analyte; 702 nm light, θ = 70 deg.)

The theoretical plots of Fig. 3.3 illustrate the matching between the wavevector of the light incident through the prism and the wavevector of the long-range surface plasma wave, showing resonant wavelength shifts in opposite directions in two different operating regions. The high sensitivity possible for the LRSPW-based sensor results from the low angle between the dispersion curves for the long-range surface plasma wave and the incident light. The exact nature of the sensitivity

and direction of wavelength shift with a change in refractive index of the analyte is highly dependent upon the relative dispersion of the sensor materials used. Therefore, accurate refractive index models are required to effectively predict the operating behavior of a sensor based upon long-range surface plasma waves.

The LRSPW effective refractive index in Fig. 3.3 is the symmetric bound mode solution of a three-layer dispersion relationship, where the three layers are Teflon AF 1601, 20 nm gold, and analyte (water, or water plus ethylene glycol to increase the refractive index by 0.002 RIU), so the effect of the prism has been ignored [10]. Simulations suggest that such an approximation is valid if the active gold layer is well separated from other materials such as the sensor chip substrate.

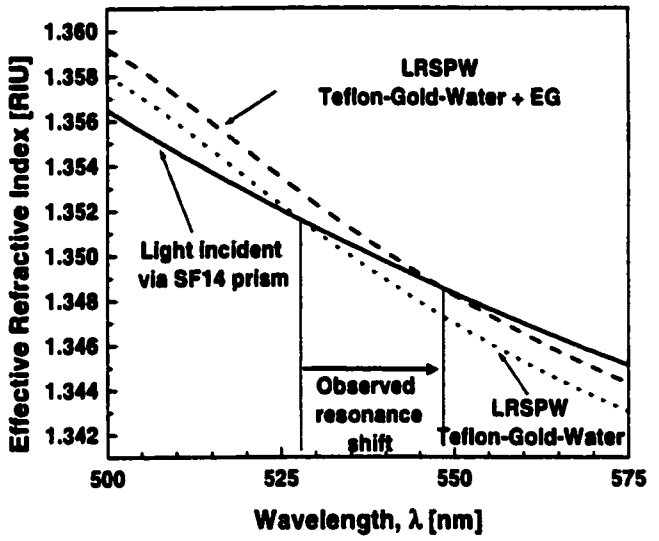

(a)

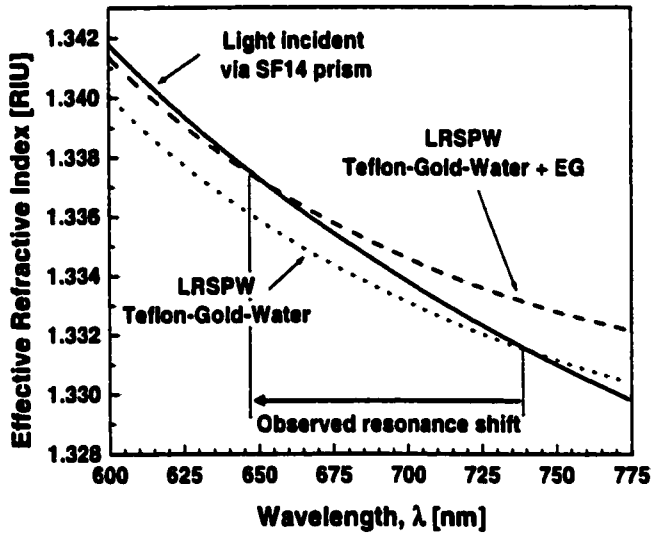

(b)

Fig. 3.3. Illustration of wavevector matching for a long-range surface plasma wave (LRSPW) supported on a 20 nm thick gold layer suspended between a Teflon AF 1601 buffer and analyte: water (dotted line) or a water-ethylene glycol mixture to raise the refractive index by 0.002 RIU (dashed line). In (a), an increase in refractive index causes an increase in resonant wavelength, while in (b), the resonant wavelength decreases. Both (a) and (b) are shown for an angle of incidence of 49.67 degrees. In this unique case, there are two wavelengths where the wave vectors can be matched.

3.2 Long-Range Surface Plasma Wave Sensor Buffer Layer

To create an LRSPW sensor, the metal layer must be separated from the coupling prism by a dielectric buffer layer with a lower refractive index than the prism, as illustrated in Fig. 3.4. Part of the difficulty in creating an LRSPW sensor is the selection of an appropriate buffer material. Ideally, the buffer-metal-analyte structure will be symmetrical, so that the buffer and analyte have the same refractive index. However, coupled plasma waves may exist on asymmetric structures [11], which has been demonstrated experimentally [12]. Indeed, controlled asymmetry of the structure may increase the propagation length of the LRSPW [13]. However, there is a limit to the amount of asymmetry in a structure supporting an LRSPW, so the buffer material should have a refractive index similar to that of the intended analyte. The refractive index of the buffer layer material is therefore an important parameter for LRSPW sensor design. For biosensors, the analyte is typically aqueous, with a thin layer of protein on the surface (functionalization material plus bound target molecules); thus, a buffer layer with a refractive index near water is required. Since dielectric materials are in general not available in a continuous range of refractive indices, selection of the buffer layer refractive index may be limited.

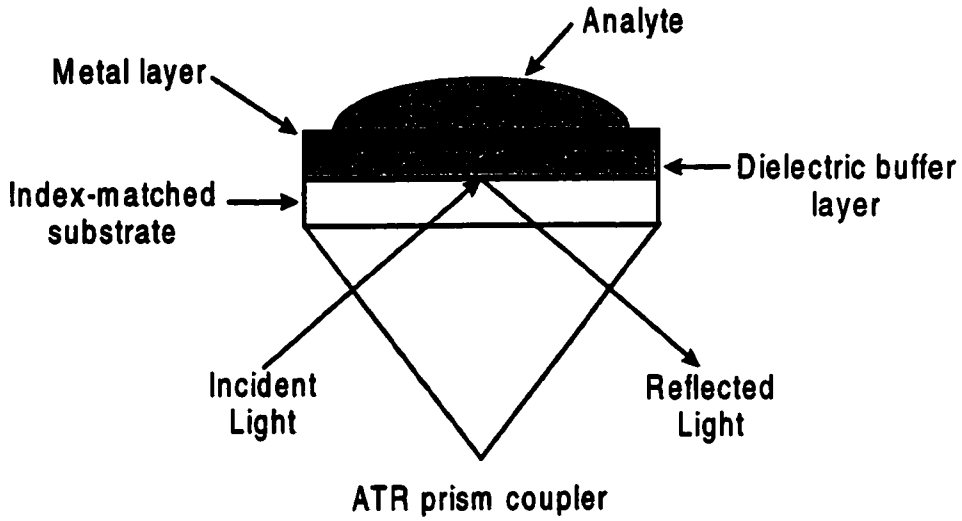

Fig. 3.4. Configuration of an LRSPW-based sensor using a removable sensor substrate.

3.2.1 Buffer Layer Materials

Two possible choices for an LRSPW sensor buffer layer material with a refractive index near that of water include amorphous perfluorinated fluoropolymers and magnesium fluoride.

Amorphous fluoropolymers are stable, chemically inert materials with good optical properties and low refractive index, approximately 1.3 RIU. Two commercially-available amorphous perfluorinated fluoropolymers are Teflon AF 1601® (DuPont Fluoroproducts, Wilmington, Delaware, USA) and CYTOP® (Asahi Glass Company, Japan). Both are available as resins dissolved in a solvent and may be applied by spin-coating.

Magnesium fluoride is commonly used to create anti-reflection coatings on lenses. It has a higher refractive index than the amorphous fluoropolymers, near 1.38 RIU. Magnesium fluoride is typically evaporated using vacuum thermal evaporation.

3.2.1.1 Teflon AF

Teflon AF is a family of amorphous perfluorinated fluoropolymers consisting of a copolymer of 2,2-bistrifluoromethyl-4,5-difluoro-1,3-dioxole (PDD) and tetrafluoroethylene (TFE) manufactured by DuPont Fluoroproducts. Applications for Teflon AF include antireflection coatings for high-power laser optical elements [14], and as tubing for liquid-core waveguides in fiber optic Raman spectroscopy [15] and spectrophotometric sensors [16].

Refractive index measurements for Teflon AF 1600 and AF 2400 series fluoropolymers are available for a range of 460-750 nm [17]. Teflon AF 1601 has low refractive index, n_D = 1.31, as well as low dispersion, with a correspondingly high Abbe number of υ_d = 92.1 [18]. The change in the refractive index of Teflon AF with wavelength is therefore less than BK7 glass (υ_d = 64.17) or SF14 glass (υ_d = 26.53) [19].

A spin curve provides a relationship between the rotational speed of a spin coater and the final thickness of the applied material. Spin curves for Teflon AF depend on the solvent used and the solids concentration of the solution. We have found that Teflon AF 1601S-40 is the best of the available solutions of Teflon AF 1601 for producing high quality spin-coated films of 0.5 μm to 2 μm thickness. A spin curve for Teflon AF 1601S-40 based on data measured by the Micro Actuators, Sensors and Systems Group of the University of Illinois at Urbana-Champaign [20]is reproduced here in Fig. 3.5.

Due to poor adhesion between Teflon AF and bare glass, a fluorosilane treatment of the glass substrate is required. With fluorosilane treatment and proper heat curing steps, the adhesion between Teflon AF and glass is more than sufficient for sensor applications.

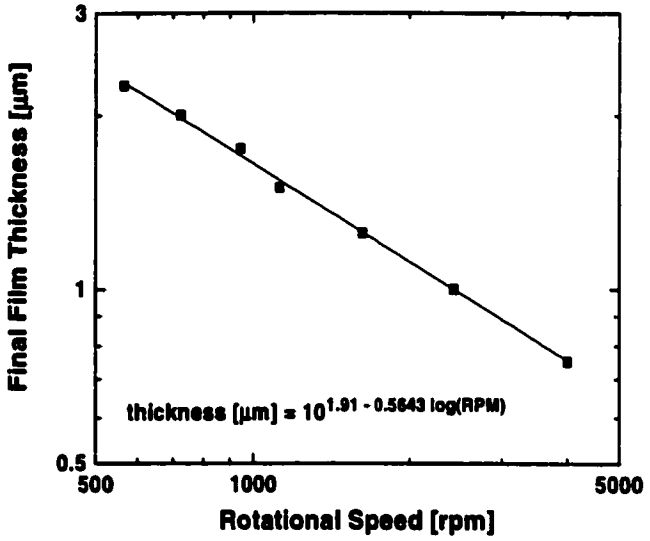

Fig. 3.5. Spin curve for Teflon AF 1601S-40. From data produced by the Micro Actuators, Sensors and Systems Group of the University of Illinois at Urbana-Champaign.

3.2.1.2 CYTOP

CYTOP is an amorphous perfluoropolymer manufactured by the Asahi Glass Company. It is synthesized by cyclopolymerization of perfluoridiene [21]. Like Teflon AF, CYTOP has a low refractive index, $n_D = 1.34$, and low dispersion, with an Abbe number of $\upsilon_d = 90$ [22]. Optical applications of CYTOP include ARCTOP® anti-reflection film, also manufactured by the Asahi Glass Company [23], as well as buffer layers for polymer waveguides [24].

Although the manufacturer of CYTOP provides spin curves for numerous grades of the material, we have been unable to verify the accuracy of this information experimentally, as our own results suggest that the final layer thicknesses are significantly thinner than predicted by the spin curves. Additionally, the power-law relationship of these spin curves is far from the expected –0.5 value of the exponent,

suggesting that the manufacturer's information is not consistent with normal spin-coating models and procedures [25].

The manufacturer also provides the refractive index of CYTOP at several wavelengths in the ultraviolet, but only the index at n_D (yellow sodium line, 589 nm) in the visible and infrared regions. Therefore, further characterization of CYTOP in terms of refractive index and accurate spin curves will be necessary to utilize it in the design of LRSPW-based sensors.

3.2.1.3 Magnesium Fluoride

Magnesium fluoride is a material with a relatively low refractive index of n_D = 1.38, commonly used for antireflection coatings in optical systems. It can be thermally deposited in a vacuum deposition system, producing hard coatings up to 1 μm in thickness. One difficulty with thermally-evaporated magnesium fluoride films is low packing density, which can create internal stresses adversely affecting the optical properties of thicker films [26]. However, magnesium fluoride has been demonstrated as a buffer layer for LRSPW-based sensors by researchers at the Institute of Radio Engineering and Electronics (IREE), Academy of Sciences of the Czech Republic, as we have reported [8].

3.2.2 Buffer Layer Thickness

For thin buffer layers, the properties of an LRSPW predicted using a semi-infinite dielectric-metal-dielectric model are affected by reradiation of the energy of the SPW back into the glass substrate and prism. The perturbing effect of the glass substrate becomes more pronounced as the buffer layer becomes thinner, causing the resonant wavelength to shift or preventing the LRSPW from being supported in some wavelength ranges.

The effect of the finite thickness of the buffer layer is demonstrated in Fig. 3.6. In the infinitely-thick buffer case, the long-range surface plasma wave mode is supported through a wavelength of approximately 825 nm, while in the case of a 1.1 μm thick Teflon AF 1601 buffer layer, the mode is supported only through 675 nm.

Fig. 3.7 illustrates the relationship between these mode predictions and the TM-polarized reflection spectrum when the LRSPW sensor chip is used in an SPR sensor system. Both the short-range and long-range surface plasma waves appear as an attenuation in the reflection spectrum.

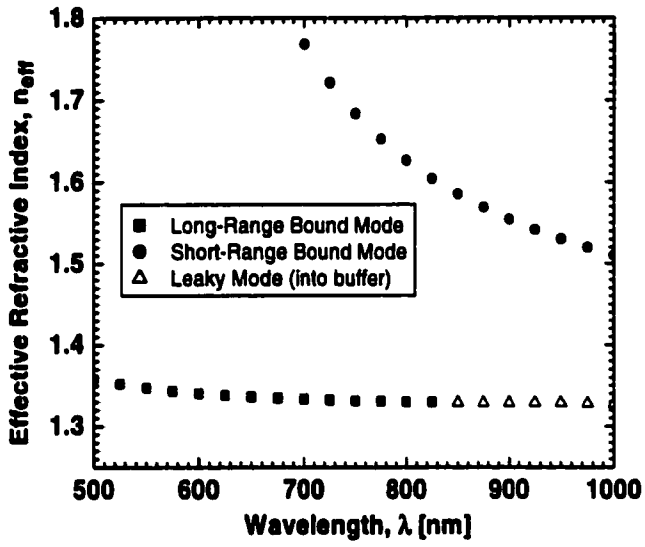

(a)

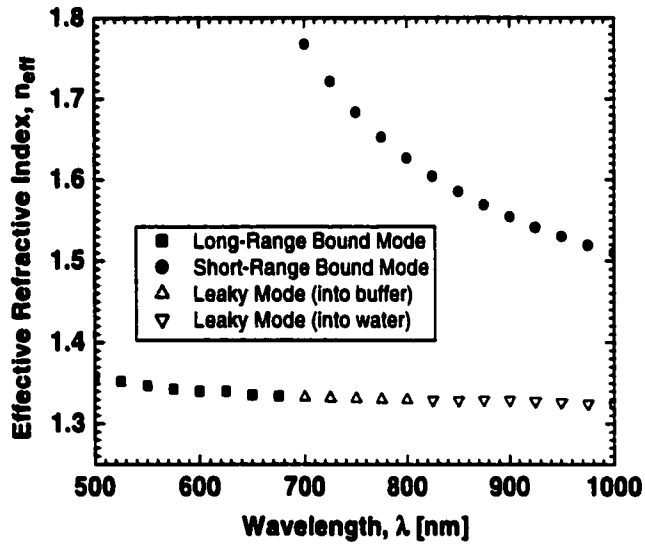

(b)

Fig. 3.6. Effect of perturbation of the long-range surface plasma wave caused by the proximity of the glass substrate. The eigenmodes are shown with an infinitively thick buffer layer (a) and a 1.1 μm buffer layer (b). Mode predictions courtesy P. Tobiška. (structure: SF14 glass, Teflon AF 1601, 20 nm gold, water)

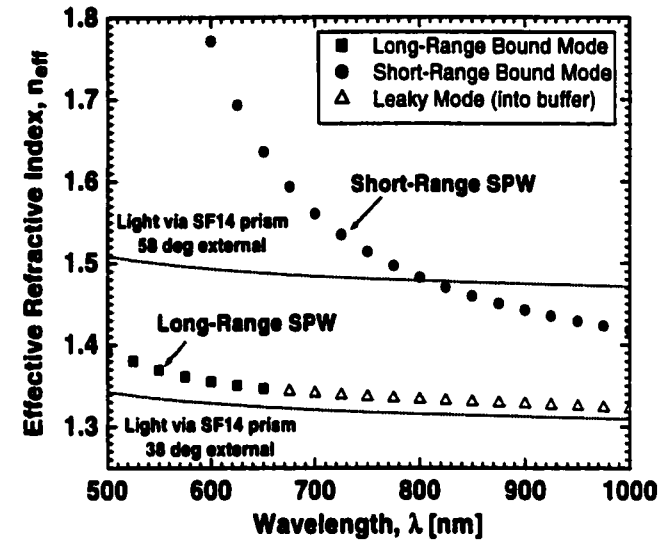

(a)

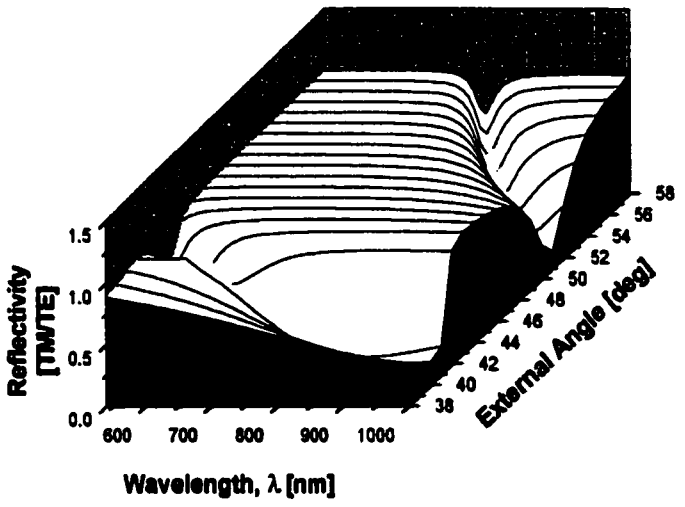

(b)

Fig. 3.7. (a) Predicted mode structure for a sensor consisting of an SF14 substrate, 500 nm Teflon AF, 30 nm gold, and water. Both long-range and short-range surface plasma wave modes are supported, as are leaky modes. The solid lines show the effective refractive index of light incident through a 60 degree SF14 prism for two angles of incidence, indicating the angular range of (b). Predicted normalized TM-polarized reflectivity of the same structure is shown in (b). Mode predictions courtesy P. Tobiška.

3.3 LRSPW-Based Sensor Design and Modeling

The behavior of a long-range surface plasma wave sensor depends upon a number of design parameters, such as: refractive index of the glass substrate, buffer layer, metal, and analyte; thickness of the buffer and metal layers; operating angle; and operating wavelength. Due to the high sensitivity of the sensor characteristics to all of these parameters, the design of an LRSPW-based sensor is more challenging than the design of a conventional surface plasmon resonance sensor. Therefore, accurate models of the sensor are required to determine the parameter values for the desired operating regime of the sensor. With these models, summary design figures may be produced to enable the designer to optimize resonant wavelength, resonance width and depth, and sensor sensitivity.

3.3.1 Refractive Index Models

In an angle-modulated SPR sensor, a single refractive index value for each material in the sensor chip is required for accurate modeling of the sensor system. The case of a wavelength-modulated sensor is more difficult, as a model of the refractive index of each material is required over the entire wavelength range of the sensor. For our sensor applications, refractive index models covering the wavelength range of 500-1200 nm are required. The sources of each of our refractive index models are provided below.

3.3.1.1 Glass Refractive Index Model

Glass substrates are used to construct LRSPW sensor chips. A prism of the same glass is also required to provide the attenuated total internal reflection (ATR) configuration required to interrogate the surface plasma wave. Schott Glass Technologies (Duryea, PA, USA) provides refractive index information for its glasses in terms of the Sellmeier formula (λ in μm):

$$n^2(\lambda) = 1 + \frac{B_1\lambda^2}{\lambda^2 - C_1} + \frac{B_2\lambda^2}{\lambda^2 - C_2} + \frac{B_3\lambda^2}{\lambda^2 - C_3} \tag{3.1}$$

For various SPR sensor designs, we have used BK7, SF2, and SF14 glass substrates. For reference, the constants for these glasses are provided in Table 3.1 [19].

Table 3.1. Sellmeier formula constants for BK7, SF2 and SF14 glass.

Constant	BK7	SF2	SF14
B1	1.03961212	1.40301821	1.69182538
B2	2.31792344×10^{-1}	2.31767504×10^{-1}	2.85919934×10^{-1}
B3	1.01046945	9.39056586×10^{-1}	1.12595145
C1	6.00069867×10^{-3}	1.05795466×10^{-2}	1.33151542×10^{-2}
C2	2.00179144×10^{-2}	4.93226978×10^{-3}	6.12647445×10^{-2}
C3	1.03560653×10^{2}	1.12405955×10^{2}	1.18405242×10^{2}

3.3.1.2 Teflon AF 1600 Refractive Index Model

A refractive index model for Teflon AF 1600 series fluoropolymers was made by fitting published data [17] with the Schott glass formula (a version of the Cauchy formula which is ironically no longer used by Schott Glass), which is a power series approximation of the Sellmeier dispersion model [27, 28]. A plot of the curve for the Teflon AF data and model is provided in Fig. 3.8.

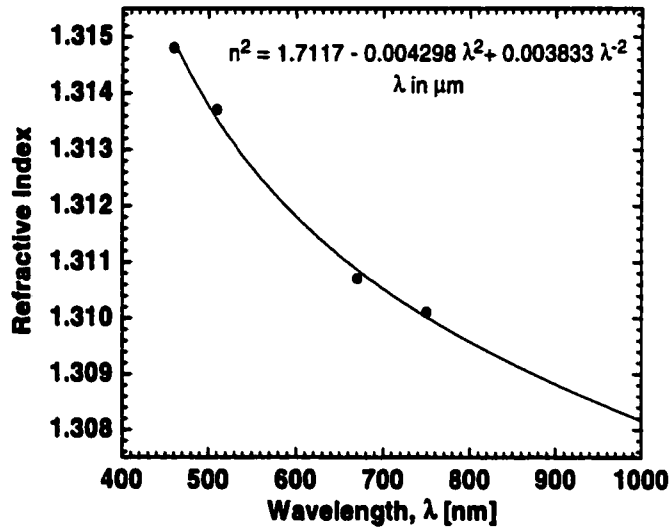

Fig. 3.8. Refractive index of Teflon AF 1601, along with Schott glass equation curve fit and data.

3.3.1.3 Magnesium Fluoride Refractive Index Model

Magnesium fluoride is a birefringent material, so the refractive index depends upon the axis of the crystal. For a thermally-evaporated thin film, averaging the refractive indices of the two axes is appropriate due to the mixed-crystalline nature of the thin film. The Sellmeier constants for magnesium fluoride are provided in Table 3.2 and are based on the data of Reference [29].

Table 3.2. Sellmeier formula constants for magnesium fluoride.

Constant	ordinary axis	extraordinary axis
B1	0.48755108	0.41344023
B2	0.39875031	0.50497499
B3	2.3120353	2.4904862
C1	0.04338408	0.03684262
C2	0.09461442	0.09076162
C3	23.793604	23.771995

3.3.1.4 Gold Refractive Index Model

The refractive index model for gold is based on data for an unannealed vacuum-evaporated gold film [30]. A simple polynomial fit, with both real and imaginary components is provided here (λ in nm):

$$n_{Au}^2 = 30.116475 - 0.064537\lambda - 4.855654\times10^{-6}\lambda^2 + j\left(16.1994265 - 0.04248\lambda + 2.888509\times10^{-5}\lambda^2\right) \tag{3.2}$$

3.3.1.5 Water Refractive Index Model

The water refractive index model is based upon data for 25 C water by R.W. Austin and G. Halikas, as reported in Reference [31]. Using this tabular data, J. Homola made a polynomial curve fit and shifted the data to correspond to a temperature of 20 C using the data of Reference [32]. The resulting refractive index model for water is (λ in nm):

$$n_{water} = 1.429331 - 4.03306\times10^{-4}\lambda + 6.50493\times10^{-7}\lambda^2 - 4.87305\times10^{-10}\lambda^3 + 1.37143\times10^{-13}\lambda^4 \tag{3.3}$$

3.3.2 Fresnel Thin-Film Model

A convenient method for modeling surface plasmon interaction is to use a Fresnel thin-film model based on the use of transmission matrices, as described by Ishimaru [1991]. The method of transmission matrices is applicable to many phenomena, such as transmission-line problems, multi-layer optical interaction, and acoustic interaction with layered medium. In this method, a 2×2 transmission matrix is used to relate the tangential electric and magnetic fields on either side of a layer of material. If the transmission matrices representing each layer of a stack of layers are multiplied together, the result is a 2×2 transmission matrix for the entire stack. Thus, the model may be used to describe an arbitrary number of layers.

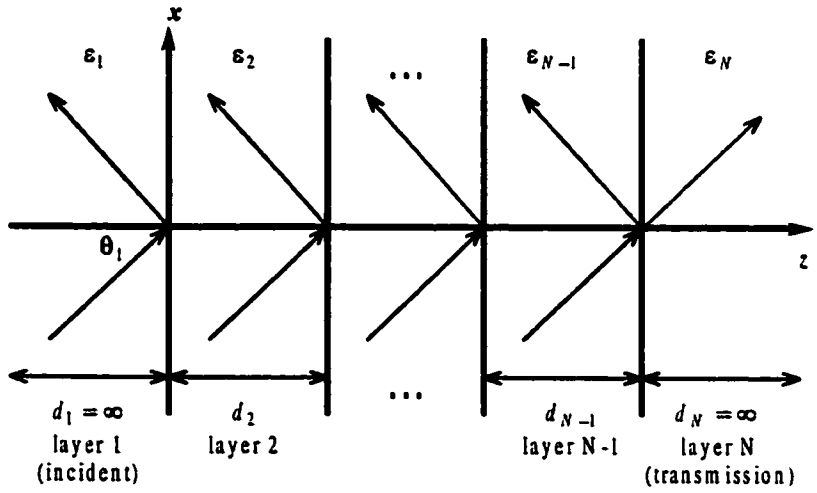

Fig. 3.9. Generalized layered thin-film structure used in the Fresnel thin-film model.

The transmission matrix model applies Maxwell's equations to the electric and magnetic fields throughout the layered media. The boundary conditions on each layer are that the tangential component of the electric and magnetic fields at each interface must be continuous across the interface. Consider the N-layer case illustrated in Fig. 3.9, noting that the axes are defined with the z-axis perpendicular to the interfaces. This nomenclature is commonly used for such thin-film models since

the on-axis light is usually of the most interest. However, it is common to define the z-axis for a surface plasma wave as the direction of the plasma wave propagation, which is parallel to the interface, so it is important to consider which nomenclature is being used. The first and last (Nth) layers are assumed to be of infinite thickness. The model assumes that all layers in an N-layer stack have both transmitted and reflected plane waves except for the Nth layer, which has only a transmitted wave, since there is no further interface to produce a reflection.

For the TM-polarized case, the fields at the end of the first region are related to the fields at the beginning of the last region by the following equation:

$$\begin{bmatrix} E_{x,d} \\ H_{y,d} \end{bmatrix}_1 = \prod_{m=2}^{N-1} \begin{bmatrix} \cos \kappa_{z,m} d_m & jZ_{TM,m} \sin \kappa_{z,m} d_m \\ \dfrac{j \sin \kappa_{z,m} d_m}{Z_{TM,m}} & \cos \kappa_{z,m} d_m \end{bmatrix}_m \begin{bmatrix} Z_{TM,N} H_{y,0} \\ H_{y,0} \end{bmatrix}_N \tag{3.4}$$

The parameters in Eq. (3.4) are defined as:

$$\kappa_{z,m} = \sqrt{\kappa_0^2 \varepsilon_m - \kappa_0^2 \varepsilon_1 \sin^2 \theta_1}$$

$$= \text{component of wave vector } \kappa_m \text{ in the } z\text{-direction}$$

$$\kappa_m = \kappa_0 n_m = \text{wave vector in layer } m$$

$$d_m = \text{thickness of layer } m$$

$$Z_{TM,m} = \frac{\eta_0 \kappa_{z,m}}{\kappa_0 \varepsilon_m} = \text{wave impedance for layer } m\text{, TM case}$$

$$\eta_0 = \sqrt{\frac{\mu_0}{\varepsilon_0}} = \text{characteristic impedance of free space}$$

$$\kappa_0 = \frac{2\pi}{\lambda_0} = \text{wave number in free space}$$

$$\lambda_0 = \text{wavelength in free space}$$

Once the electric and magnetic fields parallel to the interfaces are determined using Eq. (3.4), the TM-polarized reflectivity may be determined using:

$$R_{TM} = \left| \frac{E_{xd,1} - Z_{TM,1} H_{yd,1}}{E_{xd,1} + Z_{TM,1} H_{yd,1}} \right|^2 \tag{3.5}$$

The case of TE-polarized light may be computed using Eq. (3.4) by making the following substitutions:

- Substitute the TE parallel field components E_y and $-H_x$ for the TM parallel field components E_x and H_y.
- Substitute $Z_{TE,m}$ for $Z_{TM,m}$ as defined by:

$$Z_{TE,m} = -\frac{\eta_0 \kappa_0}{\kappa_{z,m}} = \text{wave impedance for layer } m, \text{ TE case} \tag{3.6}$$

3.3.3 Long-Range Surface Plasma Wave Sensor Design Curves

Once the buffer material is chosen, the primary design parameters are the thickness of the metal layer (typically gold) and the thickness of the buffer layer. The operating angle of the instrument may be varied in order to produce the best coupling between the light and the LRSPW, as indicated by a deep resonance with low TM-polarized reflectivity at the minimum of the resonance. Choosing a design analyte provides an operating point for the sensor. Given these parameters, design curves may be produced displaying the best resonance depth, the resonant wavelength, the width of the resonance minimum, and the sensitivity of the sensor. These plots are based on the Fresnel matrix thin-film model of the sensor structure, with numeric calculations of sensitivity and other performance parameters. Design curves for a sensor operating in water are provided in Fig. 3.10 for Teflon AF 1601 buffer.

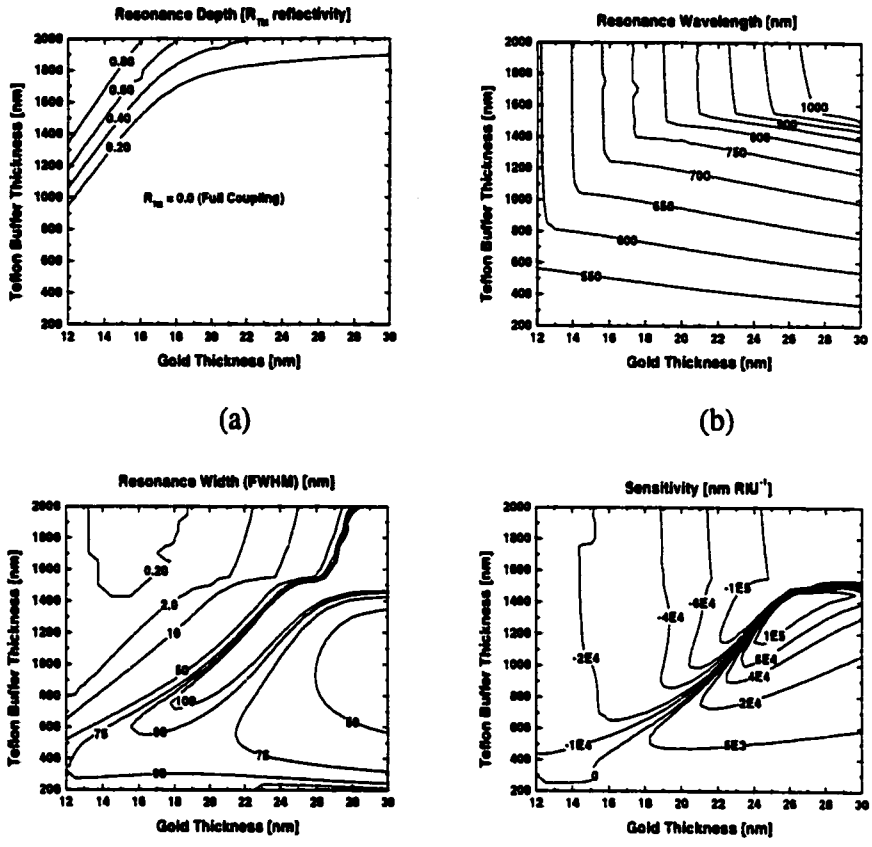

Fig. 3.10. Design curves as a function of metal and buffer thickness for an LRSPW sensor using an SF14 glass substrate and a Teflon AF 1601 buffer layer, with water as the analyte. The operating angle was optimized at each point to achieve the greatest coupling into the resonance (operating wavelength 500-1000 nm). (a) Resonance depth. (b) Resonant wavelength. (c) Resonance width (full width at half-minimum). (d) Sensitivity.

As illustrated in Fig. 3.10(d), the LRSPW sensor exhibits a transition in response from increasing resonant wavelength with refractive index to decreasing wavelength with refractive index. For sensors constructed with a thick gold layer and a thin buffer layer, the resonant wavelength shifts to longer wavelengths as the refractive index of the analyte increases. For sensors constructed of a thin gold layer and a thick buffer layer, the resonant wavelength shifts to shorter wavelengths with an

increase in the refractive index of the analyte. Near the transition between these regimes, the sensitivity is very low. For other specific combinations of gold thickness and buffer thickness, the magnitude of the sensitivity can be extremely high, on the order of 1×10^5 nm RIU^{-1} in the case of this Teflon-based LRSPW sensor. This sensitivity compares with 1.4×10^4 nm RIU^{-1} for a conventional prism-coupled wavelength-interrogation SPR sensor operating at 850 nm.

Another characteristic of the sensor is illustrated in the resonance width curves of Fig. 3.10(c). The sensor shows a broadening of the resonance width over a range of gold thickness and buffer thickness. The broadening of the resonance is caused by matching between the wavevector of the illuminating light and the wavevector of the LRSPW over a range of wavelengths. The exact nature and magnitude of this effect is dependent upon the relative dispersion characteristics of the sensor materials and the analyte. This effect was observed experimentally in the case of the Teflon-based LRSPW sensor.

Although these theoretical predictions show quite narrow resonance widths for very thin gold layers, such narrow widths may not be achievable in practice. The narrow width is achieved by having a long propagation length (low attenuation of the LRSPW along the direction of propagation) for the LRSPW. If the quality of the gold is not sufficient to allow these long propagation lengths, then the observed resonances will be broader than in theory. Thermal evaporation and electron-beam deposition produce continuous films of gold for a thickness greater than about 20 nm, so a thinner layer of gold may limit the propagation length of the LRSPW. Effects such as optical scattering and imperfect boundaries between layers also act to increase the width of the observed resonances. In addition, the characteristics of the spectrometer used to analyze the reflection spectrum are an important factor. Typically, the spectrometer will have a spectral resolution limited by the number of pixels of the

linear detector and the characteristics of the grating and slit used, which may also limit the minimum observable resonance absorption feature width.

Fig. 3.10 does indicate that it should be possible to design and construct an LRSPW-based sensor which should have an order of magnitude better resolution than conventional SPR sensors. Specifically, such a sensor would have full coupling of light into the long-range surface plasmon, sensitivity on the order of 10^5 nm RIU^{-1}, and a theoretical resonance width of approximately 10 nm (compared with approximately 100 nm for a conventional gold SPR sensor).

Furthermore, these theoretical design curves indicate that such performance should occur for a sensor using 20 nm thick gold, which should be thick enough to provide a relatively continuous film. A Teflon thickness of between 1000 and 1800 nm will be required to realize this level of sensor performance.

For comparison, LRSPW-based sensor design curves for a magnesium fluoride (MgF_2) buffer layer are shown in Fig. 3.11. The predicted performance for an LRSPW-based sensor using a MgF_2 buffer layer differs in many aspects from a sensor using a Teflon AF buffer layer. Significantly, the maximum sensitivity is not as high for the sensor using MgF_2, and the resonance width is in general wider.

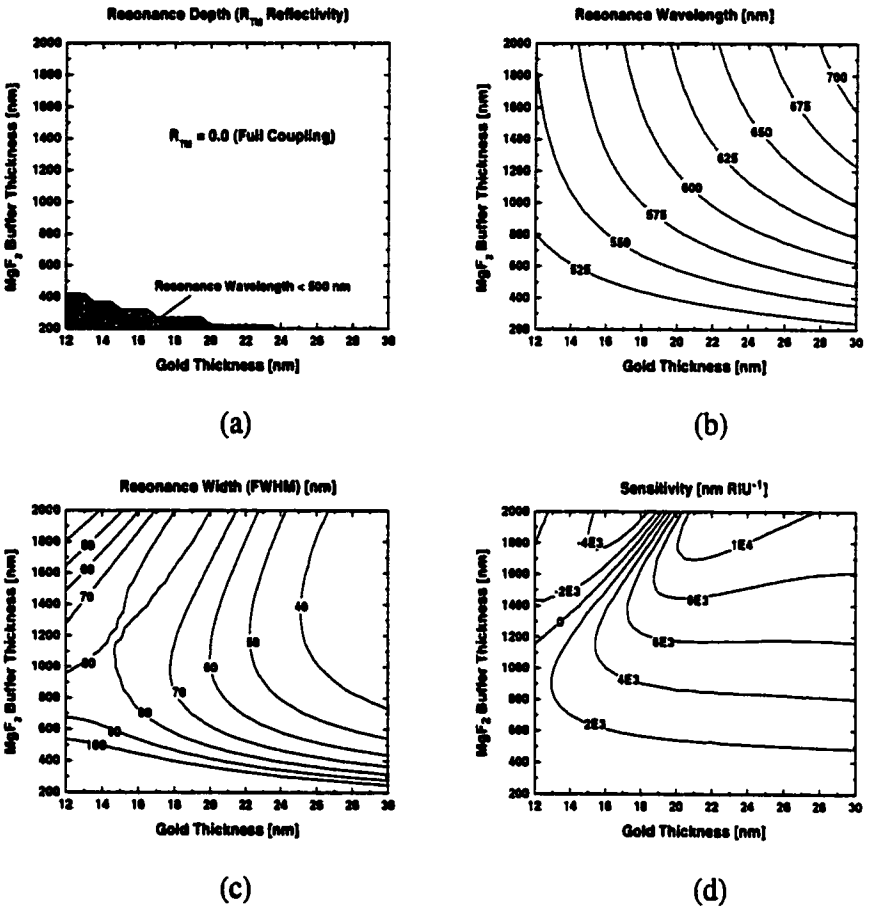

Fig. 3.11. Design curves as a function of metal and buffer thickness for an LRSPW sensor using an SF2 glass substrate and a magnesium fluoride buffer layer, with water as the analyte. The operating angle was optimized at each point to achieve the greatest coupling into the resonance (operating wavelength 500-1000 nm). (a) Resonance depth. (b) Resonant wavelength. (c) Resonance width (full width at half-minimum). (d) Sensitivity.

Notes for Chapter 3

[1] D. Sarid, Long-range surface-plasma waves in very thin metal films, Physical Review Letters 47 (1981) 1927-1930.

[2] J.C. Quail, J.G. Rako, H.J. Simon, Long-range surface-plasmon modes in silver and aluminum films, Optics Letters 8 (1983) 377-379.

[3] C. Plumereau, A. Bouchoux, A. Cachard, Electrooptic light modulator using long-range surface plasmons, Novel Optoelectronic Devices, Proceedings of the SPIE 800 (1987) 79-83.

[4] J.S. Schildkraut, Long-range surface plasmon electrooptic modulator, Applied Optics, 27 (1988) 4587-4590.

[5] P. J. Kajenski, Tunable optical filter using long-range surface plasmons, Optical Engineering 36 (1997) 1537-1541.

[6] G.I. Stegeman, J.J. Burke, D.G. Hall, Nonlinear optics of long-range surface plasmons, Applied Physics Letters 41 (1982) 906-908.

[7] K. Matsubara, S. Kawata, S. Minami, Multilayer system for a high-precision surface plasmon resonance sensor, Optics Letters 15 (1990) 75-77.

[8] G.G. Nenninger, P. Tobiška, J. Homola, S.S. Yee, Long-range surface plasmons for high-resolution surface plasmon resonance sensor, Sensors and Actuators B 74 (2001) 145-151.

[9] J. Čtroký, J. Homola, P.V. Lambeck, S. Musa, H.J.W.M. Hoekstra, R.D. Harris, J.S. Wilkinson, B. Usievich, N.M. Lyndin, Theory and modelling of optical waveguide sensors utilising surface plasmon resonance, Sensors and Actuators B 54 (1999) 66-73.

[10] J.J. Burke, G.I. Stegeman, T. Tamir, Surface-polariton-like waves guided by thin, lossy metal films, Physical Review B 33 (1986) 5186-5201.

[11] J.J. Burke, G.I. Stegeman, T. Tamir, Surface-polariton-like waves guided by thin, lossy metal films, Physical Review B 33 (1986) 5186-5201.

[12] N.M. Lyndin, I.F. Salakhutdinov, V.A. Sychugov, B.A. Usievich, F.A. Pudonin, O. Parriaux, Long-range surface plasmons in asymmetric layered metal-dielectric structures, Sensors and Actuators B 54 (1999) 37-42.

[13] L. Wendler, R. Haupt, An improved virtual mode theory of ATR experiments on surface polaritons, Physica Status Solidi B 143 (1987) 131-148.

[14] N. Bazin, J.E. Andrew, H.A. McInnes, Formation of Teflon AF Polymer Thin Films as Optical Coatings in the High Peak Power Laser Field, Proceedings of the SPIE 3492 (1999) 964-969.

[15] R. Altkorn, I. Koev, M.J. Pelletier, Raman Performance Characteristics of Teflon-AF 2400 Liquid-Core Optical-Fiber Sample Cells, Applied Spectroscopy 53 (1999) 1169-1176.

[16] E. Kaltenbacher, E.T. Steimle, R.H. Byrne, A compact, in-situ, spectrophotometric sensor for aqueous environments: design and applications, IEEE Proceedings of the 2000 International Symposium on Underwater Technology, Tokyo, Japan, May 23-26, 2000.

[17] J.H. Lowry, J.S. Mendlowitz, N.S. Subramanian, Optical characteristics of Teflon AF fluoroplastic materials, Optical Engineering 31 (1992) 1982-1984.

[18] DuPont Fluoroproducts, Properties of Amorphous Fluoropolymers Based on 2,2-Bistrifluoromethyl-4,5-Difluoro-1,3-Dioxole, H-5245-2 (1997).

[19] Schott Glass Technologies, Schott Optical Glass, Schott Glass Technologies, Inc., Duryea, PA, 1992.

[20] M. Khoo, Process Instructions: Teflon AF1601S-40, Micro Actuators, Sensors and Systems Group, University of Illinois at Urbana-Champaign, http://mass.micro.uiuc.edu/.

[21] N. Sugiyama, Perfluoropolymers Obtained by Cyclopolymerization and Their Applications, in J. Scheirs (ed.), Modern Fluoropolymers, John Wiley and Sons, Ltd., New York, 1997, Ch. 28.

[22] Asahi Glass Company, CYTOP Amorphous Fluorocarbon Polymer Technical Information.

[23] Asahi Glass Company, ARCTOP anti-reflection film, http://www.agc.co.jp.

[24] Y.G. Zhao, W.K. Lu, Y. Ma, S.S. Kim, S.T. Ho, T.J. Marks, Polymer waveguides useful over a very wide wavelength range from the ultraviolet to infrared, Applied Physics Letters 77 (2000) 2961-2963.

[25] R.K. Yonkoski, D.S. Soane, Model for spin coating in microelectronic applications, Journal of Applied Physics 72 (1992) 725-740.

[26] A. Macleod, Thin film optical materials, in A.A. Elshabini-Riad, F.D. Barlow III (eds.), Thin Film Technology Handbook, McGraw-Hill, New York, 1998, Ch. 8, pp. 1-41.

[27] S.P. Langley, C.G. Abbot, Annals of the Astrophysical Observatory of the Smithsonian Institution, U.S. Government Printing Office, Washington, 1900, p. 253-254.

[28] M. Bass (ed.), Handbook of Optics, McGraw-Hill, New York, 1995, Ch. 33.

[29] R.W. Waynant, M.N. Ediger (eds.), Electro-Optics Handbook, McGraw-Hill, Inc., New York, 1994, Ch. 11.

[30] D.E. Aspnes, Fourier transform detection system for rotating-analyzer ellipsometers, Optics Communications 8 (1973) 222-225.

[31] P.D.T. Huibers, Models for the wavelength dependence of the index of refraction of water, Applied Optics 36 (1997) 3785-3787.

[32] P. Scheibener, J. Strab, J.M.H. Levelt Sengers, J.S. Gallagher, Refractive Index of Water and Steam as Function of Wavelength, Temperature and Density, Journal of Physical and Chemical Reference Data 19 (1990) 677-716.

Chapter 4: Long-Range Surface Plasma Wave Sensor Construction and Instrumentation

The construction of long-range surface plasma wave (LRSPW) sensor chips is more complicated than conventional surface plasmon resonance (SPR) sensor chips largely due to the need for a dielectric buffer layer separating the metal layer from the substrate. However, the buffer layer may be applied using standard semiconductor wafer-processing equipment and techniques, so that once the protocol has been developed and optimized, the manufacture of LRSPW sensor chips with repeatable, uniform performance is possible.

4.1 Long-Range Surface Plasma Wave Sensor Construction

We have prepared long-range surface plasma wave sensors using both Teflon AF and Cytop buffer layers. However, our Cytop-based long-range surface plasma wave sensors have not been well characterized in terms of refractive index and thickness of the buffer layer. Therefore, preparation instructions and experimental data will be presented only for Teflon AF-based long-range surface plasma wave sensors.

4.1.1 Substrate Preparation

Rectangular SF14 glass substrates 32 mm by 15 mm by 2 mm were custom manufactured by Schott Glass Technologies (Duryea, PA, USA) to an optical quality of 20/10 scratch-dig on the two large faces. These substrates were identical to those used in our SPR instrument for conventional SPR experiments. To identify the final sensors, a small identifying number was scribed on the back side of the substrate in one corner. This numbering was necessary because of the various treatments, buffer materials, and buffer and gold thicknesses used in the development of the LRSPW sensors, but would not be necessary for final production sensors. The substrates were

cleaned for 30 minutes in an ultrasonic cleaner using a standard working solution of Pierce RBS-35 detergent (Rockford, IL, USA) and deionized water. During ultrasonic cleaning, substrates were placed in small open plastic vials in a larger glass beaker containing the cleaning solution. The plastic vials were sized to hold the substrates in an upright position with only the edges of the substrate contacting the vial, allowing solution to circulate across the faces of the substrate and preventing scratching or pitting of the glass.

Following treatment in the detergent, the beaker and vials were drained and refilled with deionized water. The substrates were then ultrasonically cleaned for an additional 30 minutes. After cleaning in the deionized water, the substrates were removed and stored in isopropyl alcohol in preparation for application of a fluorosilane adhesion promoter.

4.1.2 Fluorosilane Treatment to Promote Fluoropolymer Adhesion

A fluorosilane treatment, based on a method recommended by DuPont Fluoroproducts (Wilmington, DE, USA) [1], was used to promote adhesion between the Teflon AF buffer layer and the glass substrate. The ultrasonically-cleaned substrates were placed in boiling isopropyl alcohol for a few minutes. The substrates were removed, blown dry with nitrogen, and then placed into a fluorosilane solution consisting of a 2 percent solution of stock 1H, 1H, 2H, 2H, 2H-perfluorodecyltriethoxy silane [Lancaster Synthesis, Windham, NH, USA] in a mixture of 5 percent water and 95 percent isopropyl alcohol. After treatment in the fluorosilane solution for approximately 5 minutes, the substrates were rinsed with isopropyl alcohol and blown dry with nitrogen. The treated substrates were placed in a glass petri dish sensor-side-up, then baked at 110 C for 10 minutes and allowed to cool.

4.1.3 Teflon AF Spin Coating

A photoresist spin coater (Specialty Coating Systems P-6000, Indianapolis, IN, USA) was used to spin coat the Teflon AF buffer layer onto the silane-treated substrates. Teflon AF is available in different concentrations and with different solvents. The best surface finish was achieved with Teflon AF 1601S40-6 (DuPont Fluoroproducts, Wilmington, DE, USA), which is a 6 percent solution of Teflon AF 1601 solids in Fluorinert FC-40 solvent (3M Chemicals, Saint Paul, MN, USA).

A clean room facility at the University of Washington was used during the application of the buffer layer, which greatly reduced the amount of contamination caused by particles. A custom vacuum chuck was machined out of aluminum to hold the substrates in position during the spin coating. The chuck featured small raised areas to center the substrate on the chuck, while a vacuum applied via a central hole holds the substrate during the coating process, as in Fig. 4.1. One substrate at a time was placed on the vacuum chuck and the vacuum was applied.

With the spin coater stopped, a pipette was used to transfer approximately 200 μl of Teflon AF solution to the surface of the substrate, covering most or all of the surface of the substrate. The spinner was then accelerated to the desired spin speed over a period of approximately 15 seconds. The spinner was allowed to spin at the final speed for 120 seconds. During the spin, much of the solvent evaporated and the Teflon AF layer neared its final thickness. After spin coating, the substrates were allowed to dry at room temperature for one to two hours. Any Teflon AF leaked onto the back face of the substrate was removed using a lint-free tissue and a razor blade if necessary. If such excess Teflon AF was not removed prior to baking, removal become much more difficult following baking, and the substrates sometimes adhered to the glass dish during baking. Any Teflon AF left on the back of the substrate following baking would also interfere with proper index matching of the substrate to the prism in the LRSPW instrument.

The substrates were placed Teflon-side-up into a covered glass petri dish and baked in a series of steps designed to remove solvent, and finally to hard-bake the Teflon AF and produce a slight improvement in the surface quality. These steps are based on recommendations by DuPont Fluoroproducts [1]:

1. Air dry coated substrates for at least 10 minutes.
2. Bake at 107 C for FC-77 Fluorinert solvent (165 C for FC-40 solvent) for 10 minutes. This temperature is the solvent boiling point plus 10 C; 99 percent of the initial solvent is removed by the end of this step.
3. Bake at 165 C for 5 minutes. This temperature is the glass transition temperature (T_g) of Teflon AF 1601 plus 5 C; the remaining solvent is removed by this step.
4. Bake at 330 C for 15 minutes. This step provides enhanced adhesion and better surface quality.

A two-step programmable oven (Telrus Temp-Master L Two-Stage Furnace, New Hyde Park, NY, USA) was used to perform these steps, and was reprogrammed after the first two steps to perform the third and highest-temperature step. After these baking steps, the substrates were removed from the oven and allowed to cool to room temperature.

Spin coating of non-circular substrates is not ideal, as a raised edge bead tends to build up on the two trailing corners of the substrate during the spin. However, the sensors had a large area in the center of the substrate of relatively even thickness which fit easily within the illuminated active area of the instrument.

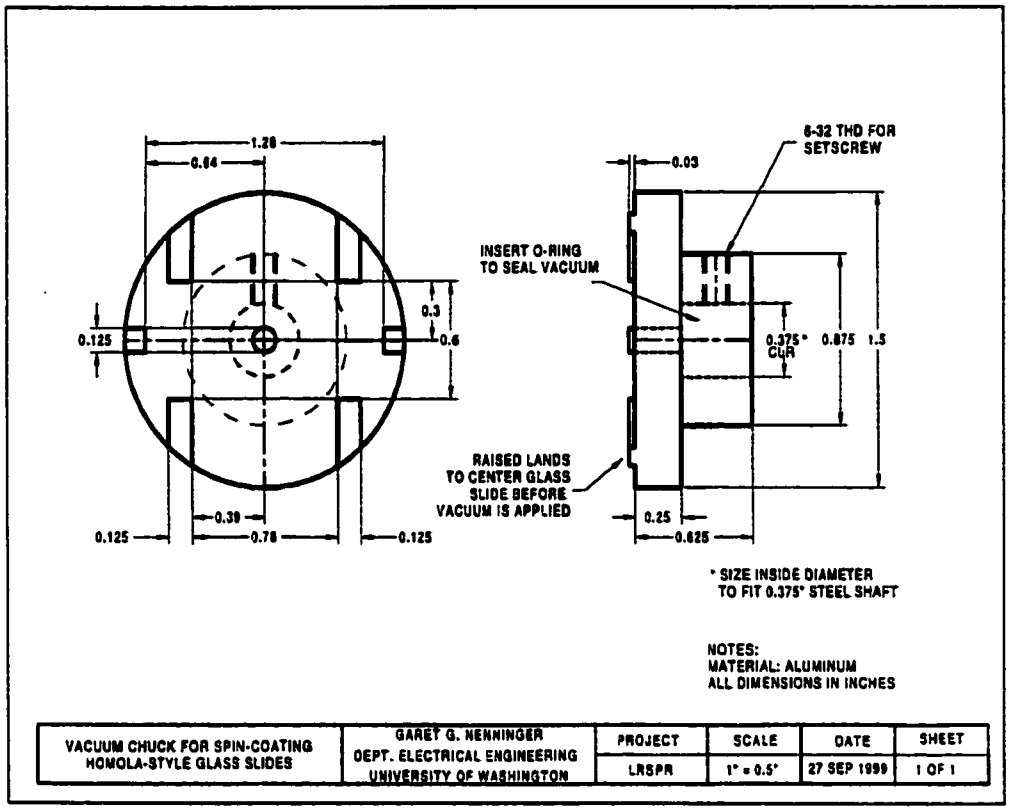

Fig. 4.1. Vacuum chuck for holding sensor substrate during spin coating of the Teflon AF buffer layer. Drawing size has been reduced from the original.

4.1.4 Gold Deposition

Gold was deposited onto the Teflon AF buffer layer using a vacuum thermal evaporation system. No treatment of the buffer layer was performed to increase the gold adhesion.

The substrates were held onto a 102 mm diameter aluminum deposition holder using spring steel wires, as detailed in Fig. 4.2. The deposition holders were designed to fit into a 4 inch waver holder in the deposition system. Five substrates were held in each holder, with three holders used during each deposition, performed with a Consolidated Vacuum Corporation CVC Model CV-18 Resistance Evaporator. Gold of 99.999 percent purity was evaporated from a tungsten dimple boat. A base

pressure of 5×10^{-6} Torr was used for the deposition, with a deposition rate of 0.1 nm/sec. The thickness of the gold was monitored using a crystal deposition monitor. Gold thicknesses between 20 nm and 30 nm were used initially, although later sensors were manufactured only with 20 nm thick gold layers.

Following deposition, the sensor chips were allowed to remain in high vacuum for 2 to 12 hours before being removed and stored in a desiccator under low vacuum.

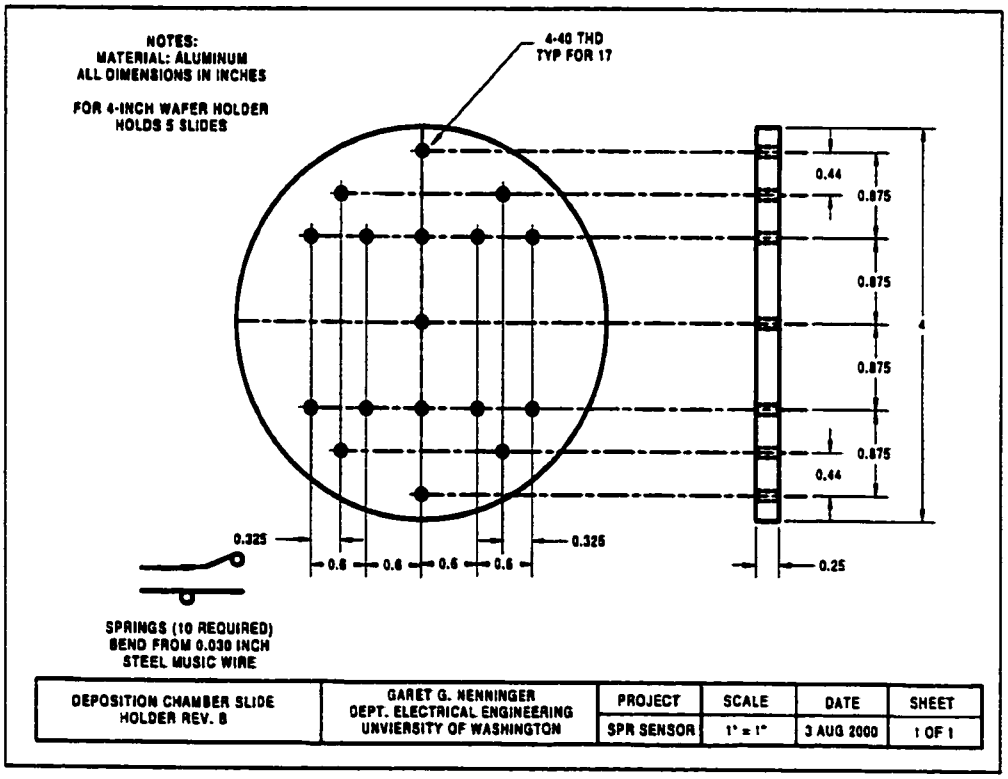

Fig. 4.2. Deposition holder for holding five sensor substrates in a 4-inch wafer holder during vacuum deposition of the gold layer. Drawing size has been reduced from the original.

4.1.5 Storage and Use of Sensor Chips

When not in use, all sensor chips were blown dry and stored in plastic vials placed in a desiccator under low vacuum. Latex gloves were used at all times when handling the chips to prevent damage by skin oils. The Teflon AF films were found to have good adhesion to the glass substrate. A layer of adhesive tape applied to the Teflon AF film will not affect the film when the tape is removed. However, due to the thinness and softness of the Teflon, it is easily scratched and may be severely damaged if rubbed with a standard pencil eraser. The extremely thin gold layer is much more fragile and may be destroyed by rubbing or touching. However, the adhesion of the gold was sufficient to prevent damage caused by the flow of liquids across the surface in the flow cell. No delamination or similar effects were noted, even for sensor chips kept in contact with water for several days.

Following use in the instrument, the chips were removed from the substrate holder and the index match fluid was removed from the back of the sensor using a cotton swab dipped in acetone. The surface of the sensor chip was flushed with deionized water and blown dry with nitrogen. The used chip was then placed in a plastic vial and returned to a vacuum environment for possible reuse or recycling.

4.1.6 Reuse of Sensor Chips and Substrates

During the course of this research, more than 100 LRSPW sensor chips were manufactured using 50 glass substrates, with some substrates reused as many as five times. Although some sensor chips exposed only to water and ethylene glycol were reused without further processing (and were not counted as new chips), in general the sensor surface became degraded with each use due to accumulated damage to the gold layer. However, the glass substrates were frequently reused, and the Teflon AF buffer layer was on occasion reused.

To reuse the sensors without removing the Teflon AF buffer layer, the gold was removed either mechanically by wiping with an alcohol-soaked tissue or by soaking in a gold removal solution used by chemists at the Institute of Radio Engineering and Electronics (IREE), Academy of Sciences of the Czech Republic, Prague to remove gold from SPR sensors [2]. The recipe for the gold-removal solution is provided in Table 4.1. First, the sensor surface was cleaned in acetone. This step helps to remove any index match fluid that may have contaminated the gold surface and may interfere with the proper operation of the gold removal solution. The substrates were then soaked in the solution for a few seconds to a few minutes until the gold was removed. The substrates were rinsed in deionized water and successive rinses of isopropyl alcohol and acetone and then dried with blown nitrogen. Sensor chips with reapplied gold appeared to have been most successful when the gold was removed using the solution rather than mechanical means. Although no damage to the surface was apparent, mechanical removal of the gold may have caused slight degradation to the surface quality of the Teflon AF buffer layer by scratching.

To reuse only the glass substrate of a sensor, the gold was removed mechanically using an alcohol-soaked tissue. The Teflon AF was removed by soaking the substrate in Fluorinert FC-77 solvent, although another grade of Fluorinert could also be used. After soaking in the Fluorinert, the substrates were removed and soaked in fresh Fluorinert. The glass substrates were then dried and were subsequently treated as new glass substrates, starting with ultrasonic cleaning in detergent as described previously. Reclaimed substrates were hydrophobic immediately following removal of the Teflon AF, indicating the presence of residual fluoryl groups on the surface of the glass. However, no differences between reclaimed and new substrates were noted during silane treatment or use of the final sensor chips.

Table 4.1. Solution for removal of gold from substrates.

Gold Removal Solution
1 g Iodine
25 g Potassium Iodide
100 ml Distilled Water

4.2 Long-Range Surface Plasma Wave Sensor Experimental Setup

The instrumentation required to support a long-range surface plasma wave sensor is in many ways similar to that necessary for a conventional SPR sensor. In this way, long-range surface plasma wave sensors have the advantage of using instrumentation and methods common to conventional SPR sensing.

A block diagram of the major components of the apparatus used to test the long-range surface plasmon resonance sensors is shown in Fig. 4.3, which illustrates the optical and electrical components of the instrument. In addition to these parts, a fluid handling system and a mechanical structure providing proper alignment and adjustment of the optical components were used. Fig. 4.4 contains photographs of the optical and mechanical portions of the instrument.

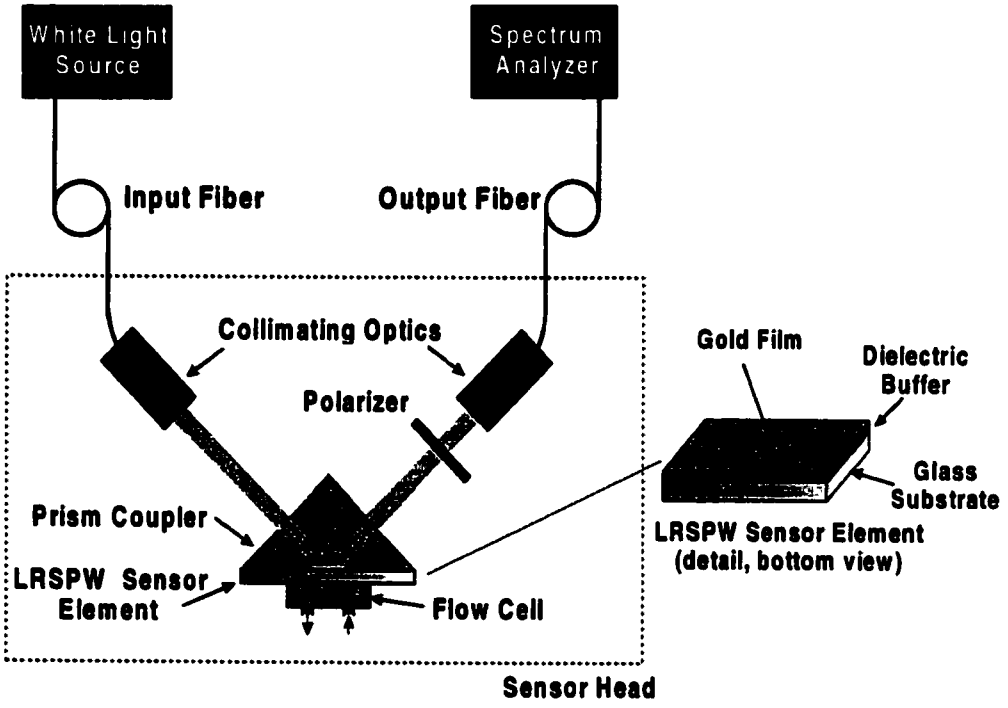

Fig. 4.3. Block-diagram of instrument used to conduct experiments with long-range surface plasma wave sensors.

4.2.1 Light Source

A tungsten-halogen light source was used to provide broadband illumination of the sensor. An Oriel Instruments (Stratford, CT, USA) QTH 250 W Research Light Source fiber optic illuminator was used for most experiments. This source provided up to 250 W to a halogen bulb. In addition, a light-level feedback system, the Oriel Light Intensity Controller, can be used to stabilize the light source to reduce drift over long periods of time.

For some experiments, a modified version of a less-expensive Ocean Optics (Dunedin, FL, USA) LS-1 fiber optic illuminator fitted with a Model LS-1-LL-B long-life bulb (2800 K color temperature) was used when light levels did not need to be as high, such as when using larger diameter input and output fibers. The regulated

5 V power supply of the Ocean Optics source was removed and replaced with an external laboratory power supply, Agilent Technologies Test and Measurement Division (Englewood, CO, USA) programmable DC power supply model E3646A, which allowed the light level to be adjusted by changing the voltage or current settings. Voltage as high as 7 V was used, providing approximately 7 W of electrical power to the lamp.

4.2.2 Input Optical Fiber

The input fiber was either a 200 μm (Model P-200-2-VIS-NIR) or 50 μm (Model P-50-2-VIS-NIR) SMA-terminated patch cable 2 meters in length manufactured by Ocean Optics (Dunedin, FL, USA). The 50 μm fiber produced a better-collimated beam, and so helped to improve the spectral resolution of the instrument for very narrow resonances.

4.2.3 Fiber Optic Collimators

The input and output fiber optic collimators were manufactured by Carl Zeiss (Jena, Germany). The collimators featured a 18 mm diameter lens aperture in a housing 25 mm in diameter made of anodized aluminum. A fitting compatible with an SMA-type fiber optic connector was mounted at the end opposite the lens and fixed in place with a setscrew.

A 1 mm wide slit perpendicular to the plane of incidence at the sensor was mounted to the output of the collimator and used to limit the area of the sensor illuminated by the light source.

4.2.4 Polarizer

SPR is a TM-polarized phenomenon, so it is important to use TM polarization when exciting SPR on the sensor. If non-polarized light is used, there will be a background signal of roughly half the total light level, caused by the non-attenuated

TE-polarized reflection. To select the desired polarization of the reflected light beam, a Polarcor dichroic glass polarizer (Corning Incorporated, Corning, NY, USA) was mounted in an aluminum housing which fit over the input or output collimator. The polarizer housing could be rotated to provide TE or TM polarized light to the spectrometer.

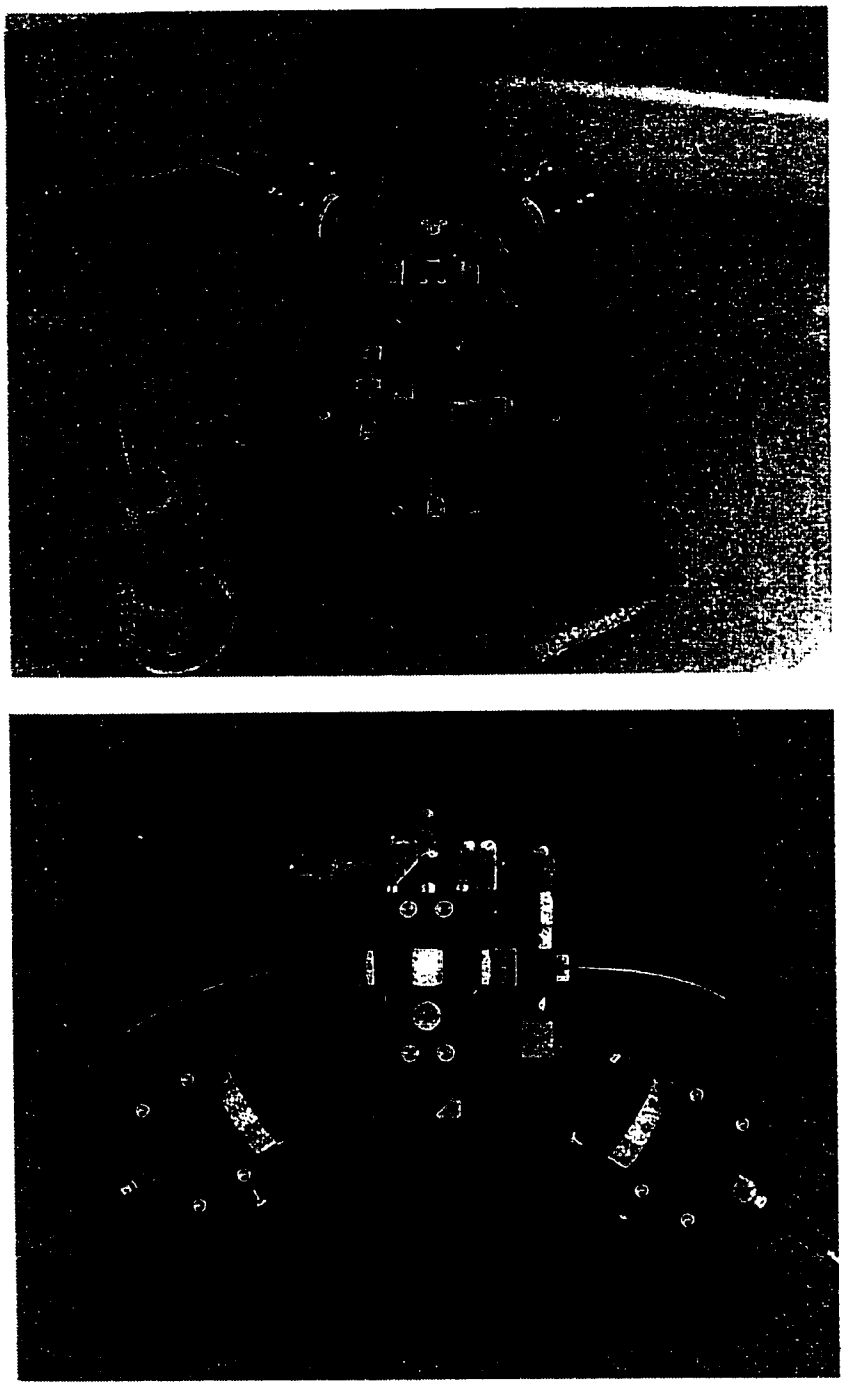

Fig. 4.4. Photographs of the instrument used to conduct long-range surface plasma wave experiments.

4.2.5 Attenuated Total Reflection Prism

R. Matthews Optical Works, Incorporated (Poulsbo, WA, USA) custom-manufactured a 50 degree SF14 prism to which the sensor substrates were index-matched. For some early experiments, as noted in the text, a 60 degree SF14 prism was used. The 60 degree prism was designed for use with conventional SPR sensor chips in this instrument. When used at the approximately 50 degree operating angle required for the SF14/Teflon long-range surface plasma wave sensors, the prism caused wavelength-dependent refraction which needed to be considered when setting the operating angle and interpreting the spectral output.

4.2.6 Output Optical Fiber

As discussed in the previous chapter, the output fiber selection is critical because it affects the spectral resolution of the spectrometer if no input slit is used. For initial alignment, 200 μm and 50 μm optical fibers were used, but for final measurements with long-range surface plasma wave sensors, a specially-manufactured polarization-preserving single-mode optical fiber jumper was used. Polarization-preserving fibers are traditionally terminated using a fiber connector which maintains the rotational alignment of the fiber. However, for compatibility with the existing SPR instrument, two meters of 3.00-3.40 μm mode-field diameter polarization-preserving fiber, type F-SPV (Newport Corporation, Irvine, CA, USA) was jacketed and terminated with standard SMA connectors. To determine the axes of polarization of the fiber, polarized light was launched into the fiber and the light exiting the fiber was passed through a second polarizer. The output polarizer was rotated 180 degrees and the lowest light level observed. The angle of rotation of the fiber at the input was then changed slightly and the rotation of the output polarizer repeated. When the polarization of the input light matched one of the polarization axes of the fiber, then the output polarizer could be adjusted to completely attenuate

the light, as there was no component of the input polarization carried on the orthogonal axis. This axis of the fiber was then marked on both connectors.

When the fiber was installed between the collimator and the spectrometer, the fiber was rotated until the TM-polarized light reflected from the sensor was aligned perpendicular to the plane of incidence of the light on the diffraction grating in the spectrometer. One axis of the fiber was found to carry light to a slightly longer wavelength, and so was used for all measurements. The threaded collar of the fiber optic connector was then tightened to maintain the proper orientation.

4.2.7 Spectrometer

An Ocean Optics (Dunedin, FL, USA) S2000 Fiber Optic Spectrometer was used for most measurements. The S2000 spectrometer uses a charge-coupled device (CCD) detector, which is more sensitive than a photodiode array (PDA) detector, but has significantly higher noise levels. Three spectrometer channels were available but only one was used for these long-range surface plasma wave experiments. A 600 line/mm diffraction grating blazed at 750 nm (Ocean Optics Grating #4) was used to provide a spectral range of 530-1200 nm. When the polarization-preserving single-mode output fiber was used, the usable range was 530-825 nm.

A few measurements were made using an Ocean Optics S1024DW spectrometer, which uses a PDA detector. However, due to the high light levels needed to provide a sufficient detector signal, the polarization-maintaining output fiber could not be used. Substituting a 50 μm output fiber provided better light levels, but caused the spectral resolution of the spectrometer to be degraded, adversely impacting the spectrum for narrow resonances.

4.2.8 A/D Conversion and Data Analysis Hardware

Two different analog-to-digital (A/D) converter boards were used during experimental measurements with the S2000 spectrometer, although for the integration

times used, the boards were functionally identical. Both cards used an ISA-bus interface to the data-collection computer. These converter boards were a 12-bit, 500 kHz A/D converter (Ocean Optics model ADC-500), and a 12-bit, 1 MHz A/D converter (Ocean Optics model ADC-1000).

For the S1024DW spectrometer using a PDA detector, a serially-interfaced 12-bit A/D converter (Ocean Optics model SAD-500) was used, as the ADC-500 and ADC-1000 were not compatible with this spectrometer. However, the serial interface was much slower than the ISA-bus interfaced A/D converter and required much more processor time of the host computer. As a result, the response time of the data processing program became uncomfortably slow under some conditions. We therefore recommend the use of an alternate A/D converter for this spectrometer should one become available in the future.

The A/D boards were installed in data-analysis computers running proprietary data collection software named "SPR-o-Matic" and written by the author. The main operating screen of the software is shown in Fig. 4.5. The software uploads the spectra from the spectrometer, performs dark-current correction, referencing, data analysis, and shows resonant wavelength trends in the two lower strip-chart displays. A variety of data can be recorded to the hard drive, including the resonant wavelength and the spectra over time. Up to four data-analysis channels are supported, which can be supplied by spectral data from up to four source spectrometer channels.

4.2.9 Mechanical Configuration

The mechanical assembly consisted of custom-machined anodized aluminum pieces and stock Melles Griot Photonics Components (Irvine, CA, USA) positioning stages (x-axis, y-axis, z-axis, and a two-axis goniometer). As illustrated in Fig. 4.4, the collimators were mounted on stands which slide along a semicircular track in order to allow adjustment of the operating angle. An angular scale was scribed into

the base plate for reference when adjusting the operating angle. For ease of operation, the replaceable sensor chip could be tightened against the prism without the flow cell in place, allowing the flow cell to be positioned and tightened separately. All adjustments included lock-down bolts to firmly hold the alignment during the course of an experiment.

4.2.10 Fluid Handling

The fluid handling system consisted of a 12-roller peristaltic cartridge pump made by Ismatec SA (Glattbrugg-Zürich, Switzerland), a custom-machined Teflon flow cell, and interconnection tubing. The tubing used was standard 1/16-inch outside diameter chromatography tubing with a 0.030-inch inside diameter. Standard chromatography fittings (Upchurch Scientific, Oak Harbor, WA, USA) were used to join the tubing to the peristaltic tubing and to the flow cell. Fluid switching was performed manually by stopping the pump, replacing the input bottle, and restarting the pump. For continuous-flow experiments, all solutions were degassed to reduce the appearance of air bubbles in the flow cell.

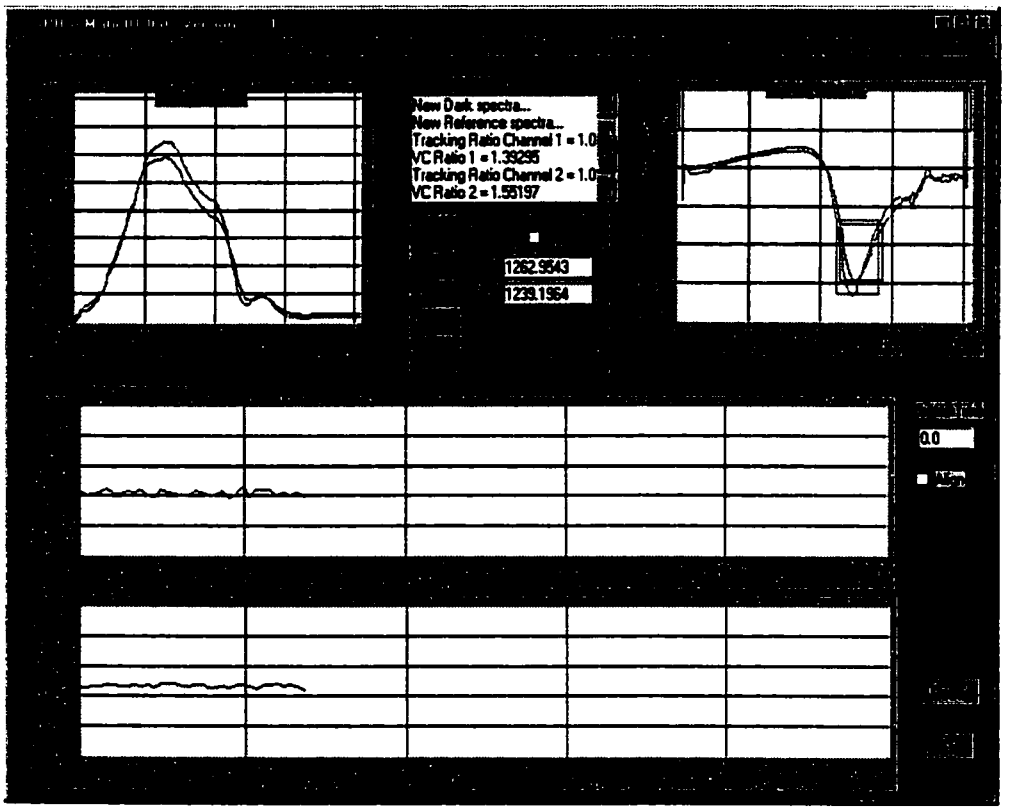

Fig. 4.5. SPR-o-Matic data collection and analysis software.

4.2.11 Sensor Chip Installation, Alignment, and Referencing

During use, the LRSPW sensors were first index-matched to the instrument prism using 1.765 RIU Series M index-matching fluid produced by Cargille Laboratories (Cedar Grove, NJ, USA). Two small drops, approximately 0.5 mm in diameter, were applied to the back, glass face of the sensor substrate using a glass rod. The edge of the substrate was held against the prism and the substrate slowly tilted until the index-matching fluid ran to the substrate-prism interface and began to spread. Without losing contact between the two, the substrate was then tilted to parallel the face of the prism. As the substrate holder was tightened, the index-match fluid evenly distributed between the prism and the substrate. The substrate was

mounted in the instrument with the active sensor surface in a vertical orientation with the long side horizontal. It was important to use the correct amount of index-match fluid. Too little fluid led to an incomplete index-match or air bubbles between the substrate and prism; too much fluid sometimes allowed some to wet the gold surface, which destroyed the gold on the sensor surface.

The input collimator was fixed at the desired operating angle, allowing for refraction at the prism, and the output collimator angle was adjusted to couple the output beam into the output fiber. For alignment purposes, the SPR-o-Matic software features an alignment mode, which provides unaveraged output spectra at an increased rate, up to several spectra per second, depending on integration time. The output collimator would frequently show a good signal over a small range of angles, on the order of 0.1 degree. The peak of the spectrum would shift in wavelength as the angle of the output collimator was varied, so that shorter wavelengths were preferred at one end of the angular range and longer wavelengths at the other. This effect was most likely the result of chromatic aberration at the prism. For consistency, the output light level was maximized using a non-resonant spectrum (TE or air reference), which centered the collimator in the output beam.

Once the collimators were aligned, the source light levels and integration time were set to provide a near full-scale output at the peak wavelength (full scale for a 12-bit A/D converter is 4095 counts). The output spectra were averaged to reduce noise levels, averaging a given number of raw spectra to produce one averaged spectrum. The amount of averaging depended upon the desired resonant wavelength data update rate and the integration time, but typically was 16 to 64 spectra.

Before measurements were made, dark and reference spectra were recorded. These spectra compensated for the background level of the detector and wavelength-dependent variations in the light intensity, respectively. Typical dark and reference spectra are illustrated in Fig. 4.6.

For the dark spectrum, the light was interrupted and a the spectrometer output was recorded. This dark spectrum was subtracted from all further measurements to adjust for the dark current in the detector, which is the leakage current in the absence of light.

Once the dark spectrum was recorded, a reference spectrum was recorded to adjust for the spectral variation in the light intensity. For most SPR sensor applications, a TE-polarized spectrum made an ideal reference, since SPR is a TM-polarized phenomenon. In this case, the polarizer was rotated 90 degrees to the TE-polarized position and the output spectrum is recorded. However, for long-range surface plasma wave sensor experiments using a polarization-preserving single-mode fiber, it was not possible to use the TE polarization, since the diffraction of the spectrometer grating is dependent upon the polarization of the light striking the grating. With a non-polarization-preserving fiber, the orientation of the TM or TE polarization at the input of the fiber is scrambled within the fiber so that the response of the spectrometer does not depend upon the input polarization. Therefore, when the polarization-preserving fiber was used, air or nitrogen was injected into the flow cell so that the long-range surface plasma wave was no longer excited. The air-based spectrum was then recorded as the reference spectrum, and liquid analyte was reintroduced into the flow cell.

Once the reference spectrum was recorded and the polarizer was aligned to TM polarization, it was frequently possible to increase the light level or integration time without causing the portion of the spectrum containing the resonance to go off-scale. Increasing the light level in this manner increased the signal-to-noise ratio and improved the resolution of the sensor. In general, the reference remains valid for small changes in the light level or integration time (doubling), since the spectral intensity scales linearly, although a new dark spectrum should be recorded if the integration time is changed.

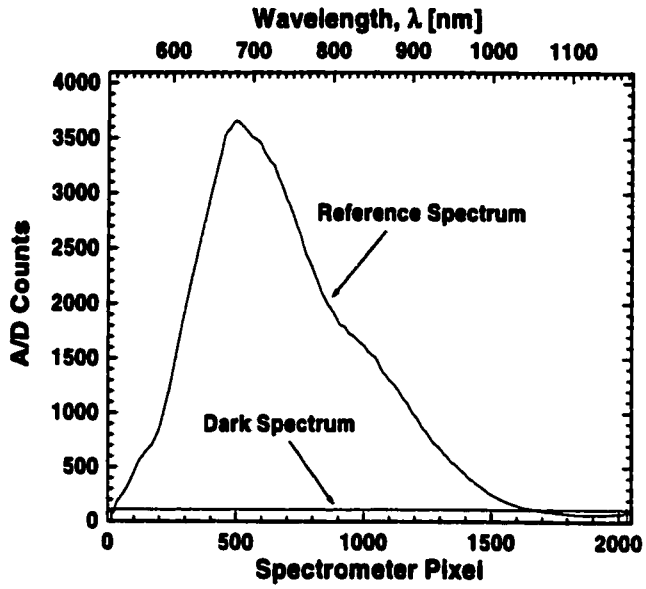

Fig. 4.6. Typical dark and reference spectra for the SPR instrument. The reference spectrum has been adjusted for the dark spectrum level.

Notes for Chapter 4

[1] DuPont Fluoroproducts, Adhesion Information for Teflon AF, Teflon AF Amorphous Fluoropolymers Product Information, H-44585-3 (1998).

[2] J. Homola, University of Washington Department of Electrical Engineering, personal communication, 2000.

Chapter 5: Long-Range Surface Plasma Wave Sensor Experiments

5.1 Observation of Coupled Plasma Wave Mode Structure

Theoretical analysis predicts that a number of electromagnetic modes may be supported by the multilayer metal-dielectric sensor structure of a long-range surface plasma wave sensor. To distinguish the modes from each other, a sample sensor chip consisting of a 500 nm Teflon AF 1601 buffer layer and 30 nm gold layer was prepared and tested with a water sample across a range of incident angles. The normalized spectra (TM-polarized spectrum divided by TE-polarized spectrum) were recorded for analysis and comparison with theoretical predictions.

The experimentally-observed and predicted reflection spectra for this sensor are provided in Fig. 5.1. The experimental spectra showed a good qualitative match with theoretical predictions of both the mode structure and the reflection spectra. The theoretical models used, including a Fresnel thin-film model and dispersive refractive index models for SF14 glass, gold, water, and Teflon AF appear to be sufficiently accurate to use for predicting the behavior of the long-range surface plasma wave sensor.

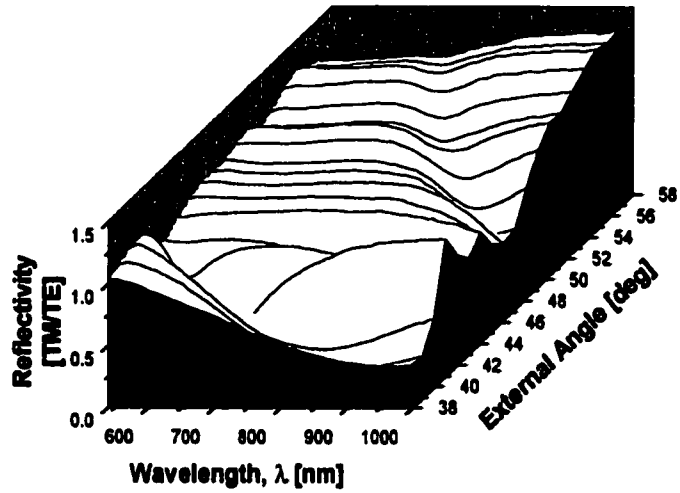

(a)

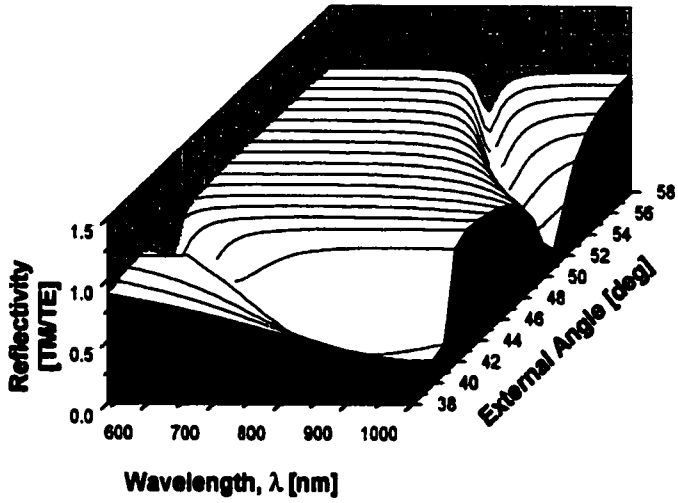

(b)

Fig. 5.1. Experimental (a) and predicted (b) normalized reflection spectra in water for a sensor consisting of SF14 glass, 500 nm Teflon AF, 30 nm gold. Light is assumed to refract through a 60 degree SF14 prism. A long-range surface plasma wave occurs at low angles, with a short-range plasma wave appearing at higher angles.

5.2 Sensor Operating Angle

The operating angle of the LRSPW instrument was varied by adjusting the position of the two collimator supports along a semi-circular track. This arrangement was designed for use with conventional SPR sensors, which are less sensitive to operating angle than LRSPW sensors. Therefore, the adjustment was difficult, particularly when attempting to maximize light coupling in the output fiber. A scale, graduated in degrees, was etched into the base plate of the instrument to assist in determining the external operating angle of the sensor. The internal operating angle was calculated from the external angle by taking into consideration the refraction occurring when the angle is varied from a direction normal to the input face of the prism. A 60 degree prism was used for early experiments, but was replaced with a 50 degree prism specially constructed for use with these LRSPW sensors, which have operating angles near 50 degrees rather than the average 60 degrees for this instrument using conventional SPR sensors on SF14 glass. Using a prism designed for the operating angle reduced the chromatic aberration of the light refracting through the prism.

As illustrated in Fig. 5.2, the behavior of the LRSPW resonance varied with small changes in operating angle. In practice, adjustments finer than 0.1 degree were not repeatable with the apparatus used. For best results, the angle was adjusted to produce a deep and narrow resonance. Longer wavelengths were preferred over shorter wavelengths due to increased sensitivity. For the sensor of Fig. 5.2, refractometric experiments were conducted using an operating angle near 49.2 degrees.

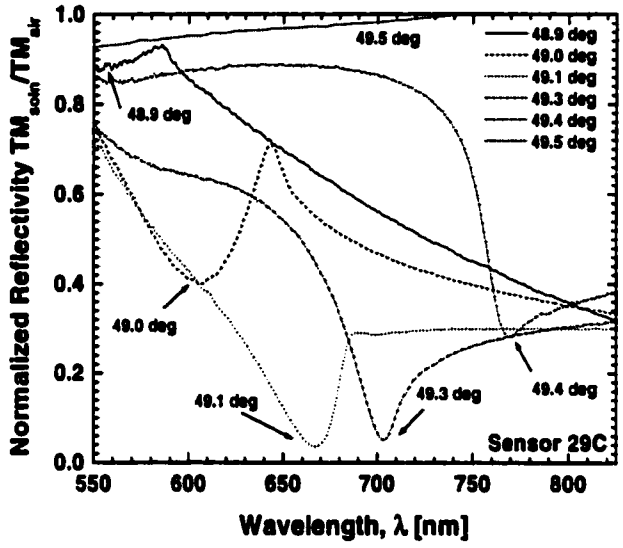

Fig. 5.2. Normalized TM-polarized spectra in water for an LRSPW sensor as the internal operating angle is varied. The sensor consisted of a 1100 nm Teflon AF buffer layer and 20 nm gold layer. The spectra were normalized to TM-polarized spectra in air.

5.3 Long-Range Surface Plasma Wave Sensor Refractometric Experiments

Compared with conventional SPR sensors, the behavior of LRSPW sensors, including the resonance depth, resonance width, and sensitivity, is much more dependent upon the operating angle. In both types of sensors, the wavelength of the resonance may be shifted by adjusting the operating angle of the instrument or by changing the refractive index of the analyte. As with conventional SPR sensors, the magnitude of the sensitivity of the LRSPW sensor using a Teflon AF buffer layer increases with increasing operating wavelength. However, the sensitivity of an LRSPW sensor may vary over a wide range depending upon the thickness of the buffer and gold layers, as shown in the design curves discussed previously. Therefore, a calibration to determine the sensitivity of the LRSPW sensor should be

performed for each new set of design parameters and operating conditions. Refractometric experiments provide a convenient method for calibrating the sensor by determining the sensor sensitivity.

To determine the sensitivity of the LRSPW sensor, standard solutions consisting of mixtures of deionized water and ethylene glycol were used. The refractive indices of these solutions at the wavelength n_D = 589.3 nm, were determined using an Abbe-3L refractometer (Thermo Spectronic, Rochester, NY, USA). The spectra for an LRSPW sensor as the refractive index of the analyte was varied over a small range is shown in Fig. 5.3, and over a larger range in Fig. 5.4.

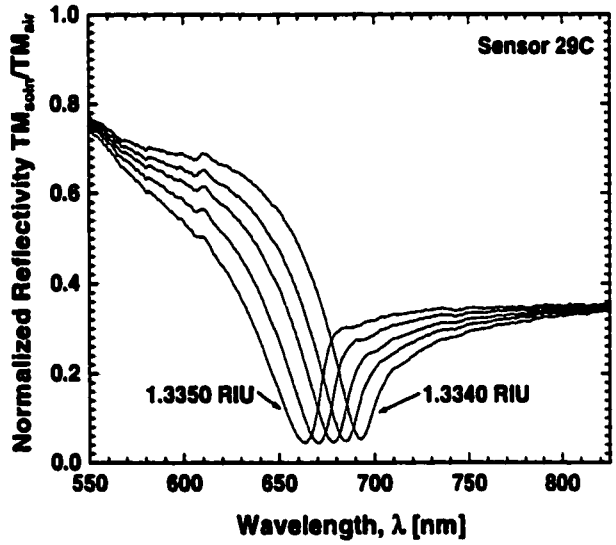

Fig. 5.3. Normalized TM-polarized spectra for analyte consisting of mixtures of water and ethylene glycol for an LRSPW sensor as the refractive index of the analyte is varied from 1.334 to 1.335. The sensor consisted of a 1100 nm Teflon AF buffer layer and 20 nm gold layer. The spectra were normalized to TM-polarized spectra at the same angle in air.

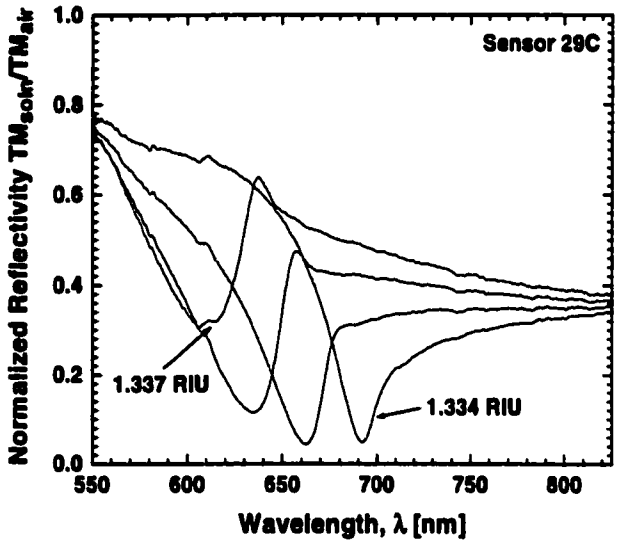

Fig. 5.4. Normalized TM-polarized spectra for analyte consisting of mixtures of water and ethylene glycol for an LRSPW sensor as the refractive index of the analyte is varied from 1.334 to 1.337 in equal steps. The sensor consisted of an 1100 nm Teflon AF buffer layer and 20 nm gold layer. The spectra were normalized to TM-polarized spectra at the same angle in air

The calibration solutions were flowed across the sensor surface by pumping them through the flow cell. Instrument control and analysis software determined the location of the resonance in spectrometer pixels using a centroid method of data analysis and saved the values every five seconds. Post-experiment analysis of the data involved converting the pixel values to wavelength using the spectrometer calibration and then plotting the results over the time of the calibration.

Calibrations were performed in a series of steps, starting with water (1.3340 RIU) and increasing the refractive index, allowing equilibrium to be reached in each new solution. Once the highest refractive index for the calibration was reached, the solution steps were reversed to return to water. The resulting stepped figure provided a method to correct for the instrument drift over the course of the calibration.

Two calibrations of an LRSPW sensor (Sensor 29C) using a 1100 nm Teflon AF buffer layer and 20 nm gold layer are presented in Fig. 5.5 for a refractive index

change of 1×10^{-3} RIU, and in Fig. 5.6 for a refractive index change of 3×10^{-3} RIU. The internal operating angle of the instrument was 49.2 degrees. As expected for this configuration, the resonance moved to a shorter wavelength with increasing refractive index.

To provide quantitative information regarding the sensitivity, the data from the calibration experiments were analyzed using data analysis software. The data from the stable part of each refractive index step as the refractive index was increased were averaged to provide the average wavelength during the step. This value was then averaged with the average value of the wavelength from the second step at this refractive index, measured later in the calibration as the refractive index was reduced. Averaging the values in this manner reduced the effect of instrument drift over the time of the calibration experiment. For each refractive index step, the change in wavelength was divided by the change in the refractive index to produce the sensitivity in units of nm RIU^{-1}.

Table 5.1 lists the sensitivity calibration for Sensor 29C at an internal operating angle of 49.2 degrees. As shown in Fig. 5.7, the relationship between the resonant wavelength and the refractive index may be plotted to provide a conversion between these two units for the specific conditions of the sensor (buffer and gold layer thicknesses, operating angle, refractive index range). The sensitivity is largely a factor of the relative dispersions of the materials, and so is a function of the resonant wavelength but not the operating angle. Many combinations of operating angle and analyte refractive index can produce the same resonant wavelength.

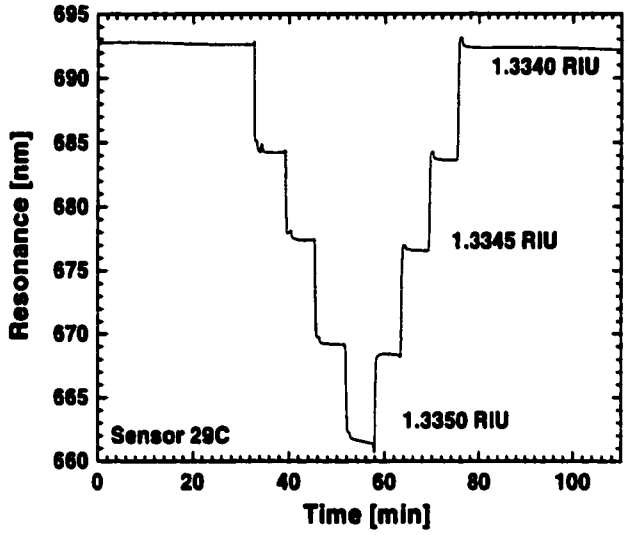

Fig. 5.5. Calibration over a 1×10^{-3} RIU range of an LRSPW sensor consisting of an 1100 nm Teflon buffer layer and 20 nm gold layer with an internal operating angle of 49.2 degrees. Calibration solutions consisted of a mixture of deionized water and ethylene glycol.

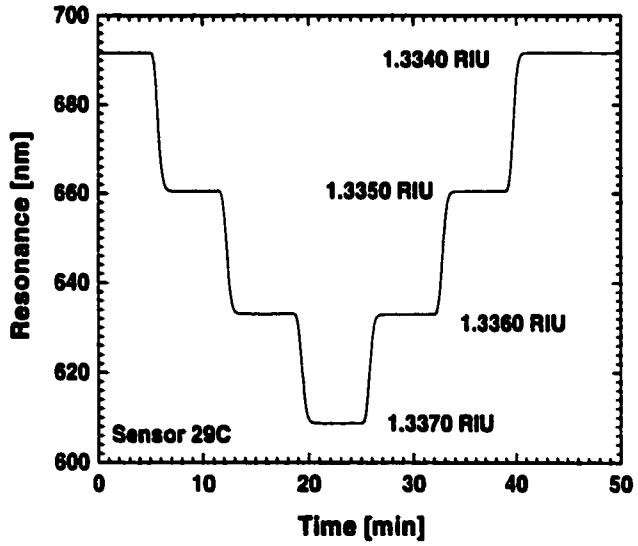

Fig. 5.6. Calibration over a 3×10^{-3} RIU range of an LRSPW sensor consisting of an 1100 nm Teflon buffer layer and 20 nm gold layer with an internal operating angle of 49.2 degrees. Calibration solutions consisted of a mixture of deionized water and ethylene glycol.

Table 5.1. Sensitivity of an LRSPW sensor (Sensor 29C at an internal operating angle of 49.2 degrees).

Wavelength Range [nm]	Refractive Index Range [RIU] (theta = 49.2 deg)	Change in Wavelength [nm]	Sensitivity [nm RIU^{-1}]
691.65 – 660.52	1.3340 - 1.3350	-31.1	31 100
660.52 – 633.02	1.3350 - 1.3360	-27.5	27 500
633.02 – 608.72	1.3360 - 1.3370	-24.3	24 300

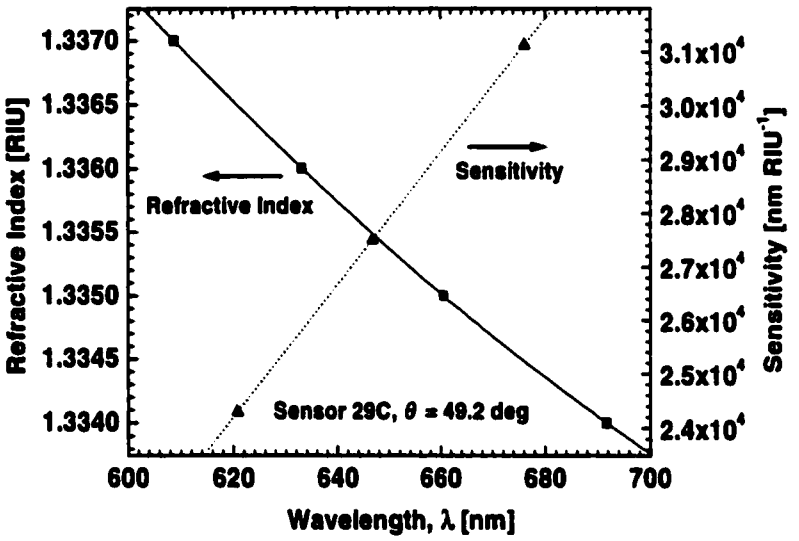

Fig. 5.7. Left axis: conversion between resonance wavelength and refractive index for an LRSPW sensor (Sensor 29C at an internal operating angle of 49.2 degrees). Right axis: relationship between wavelength and the sensitivity for this sensor.

As illustrated in Fig. 5.7, the sensitivity of the LRSPW sensor increases with wavelength. It is possible to modify the angular alignment of the instrument to increase the sensitivity for a given application. For example, most buffer liquids used in biosensing have a refractive index greater than water. If the LRSPW sensor is aligned in water, then the change in the resonant wavelength caused by a injection of the buffer liquid may be quite large due to the high sensitivity of the sensor. In the

case of the sensor of Fig. 5.7, injection of the buffer liquid would cause both the resonant wavelength and the sensitivity to decrease. For phosphate buffered saline (PBS), which has a refractive index near 1.336 RIU, the sensitivity would be reduced by 22 percent. Another concern is that the shape of the resonance may be quite different in the buffer than in water, as illustrated by the graph of Fig. 5.4, which shows spectra for various refractive indices for this sensor. As the refractive index was increased, the resonance become wider and had poorer resonance depth. This effect increased the noise level of the sensor and would combine with the decreased sensitivity to degrade the resolution of the instrument. The resolution of the biosensing experiment may be maximized by aligning the operating angle of the sensor to achieve the best sensitivity and narrowest resonance while the sensor is sensing the liquid buffer rather than water.

5.4 Long-Range Surface Plasma Wave Sensor Biosensing Experiments

All of the experimental measurements discussed above were measurements of the bulk refractive index of the analyte. As such, they do not demonstrate the key advantage of SPR sensors, which is the surface sensitivity of the sensor. Most SPR biosensing experiments use the surface sensitivity to an advantage by selectively binding target molecules to the surface of the sensor. For example, the bare gold sensor surface could be functionalized using antibodies to a target protein or toxin. If a solution containing the target molecule is subsequently flowed across the sensor surface, then the binding of the target to the functionalized surface will be observed as a change in the resonant wavelength of the sensor.

5.4.1 Long-Range Surface Plasma Wave Sensor Measurement of Protein–Antibody Binding

To demonstrate LRSPW biosensing, a simple protein-antibody interaction was observed. First, bovine albumin protein in buffer was used to functionalize the sensor surface. The bovine albumin bound to the bare gold. After a brief wash in buffer, anti-BSA antibodies in buffer were flowed across the sensor surface. The binding of the antibody to the protein was then observed.

The buffer was 1X Dulbecco's Phosphate Buffered Saline (PBS) (Bio-Whittaker, Wakersville, MD, USA). Bovine albumin was from Sigma Chemicals (St. Louis, MO, USA) and was prepared by dissolving in PBS to create a concentration of 1 $\mu g\ ml^{-1}$. The anti-BSA monoclonal antibody was also from Sigma Chemicals and was diluted in PBS to produce a 1 $\mu g\ ml^{-1}$ solution. Flow rate was 50 $\mu l\ min^{-1}$ using a peristaltic cartridge pump. The LRSPW sensor consisted of an SF14 substrate with an 1100 nm Teflon AF buffer layer and 20 nm gold layer. An internal operating angle of 49.5 degrees was used to produce an optimum resonance depth and sensitivity while in the PBS buffer.

Fig. 5.8 shows the response of an LRSPW sensor during the bovine albumin–anti-BSA immunoassay experiment. For this sensor and operating regime, a decrease in resonant wavelength indicates an increase in the refractive index at the surface of the sensor, so the binding curves are inverted relative to normal SPR conventions.

In Fig. 5.9, the LRSPW sensor response during the bovine albumin–anti-BSA immunoassay experiment has been converted to units of refractive index using a calibration for the sensor. Note in particular the LRSPW sensor's response to the bulk refractive index of the bovine albumin/PBS and the anti-BSA/PBS solutions, seen as a sudden increase in the measured refractive index when switching from buffer. A similar decrease in the measured refractive index occurs when returning to the PBS buffer.

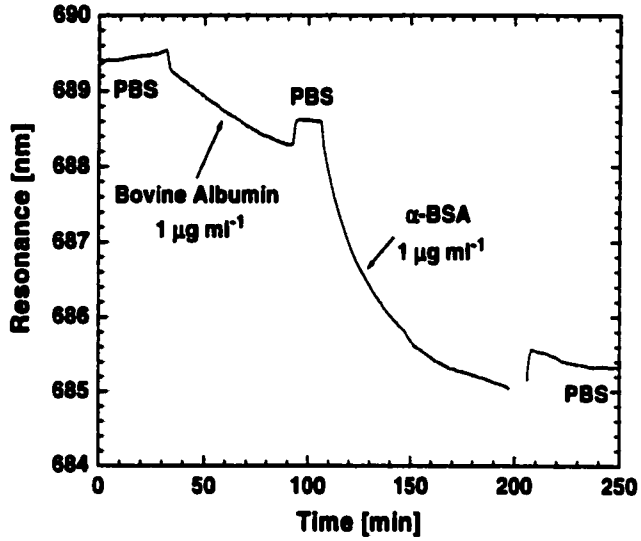

Fig. 5.8. LRSPW sensor response during a bovine albumin–anti-BSA immunoassay experiment. A decrease in resonant wavelength indicates an increase in the refractive index at the surface of the sensor.

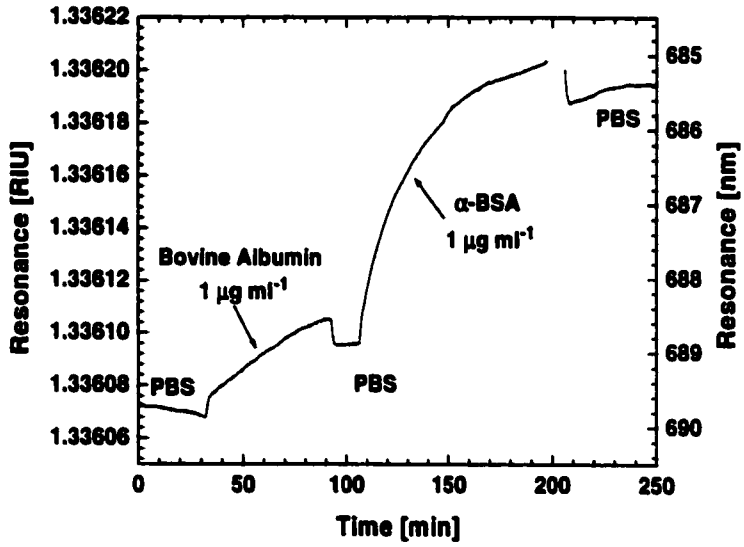

Fig. 5.9. LRSPW sensor response during a bovine albumin–anti-BSA immunoassay experiment. Sensor response has been converted to refractive index units using a sensor calibration.

5.4.2 Comparison Between SPR and LRSPW Sensor Performance

For comparison with the LRSPW sensor, Fig. 5.10 shows the response for a conventional SPR sensor during a during a bovine albumin–anti-BSA immunoassay experiment at a higher concentration of bovine albumin and anti-BSA. The sensor was an SPR planar lightpipe described in other papers [1, 2]. A graph of the normalized spectra for the SPR and LRSPW sensors used in these immunoassay experiments appears in Fig. 5.11. While conventional SPR resonances are usually deeper and narrower than this example, the LRSPW resonance would still be significantly narrower than a conventional SPR sensor using gold. Table 5.2 compares the performance of the LRSPW and SPR sensors during the experiments. Although the resolution of the resonant wavelength measurement is only improved by a factor of 1.6 in the LRSPW sensor, the sensitivity was 16 times higher. As a result, the final refractive index resolution was 25 times better for the LRSPW sensor than for the SPR sensor.

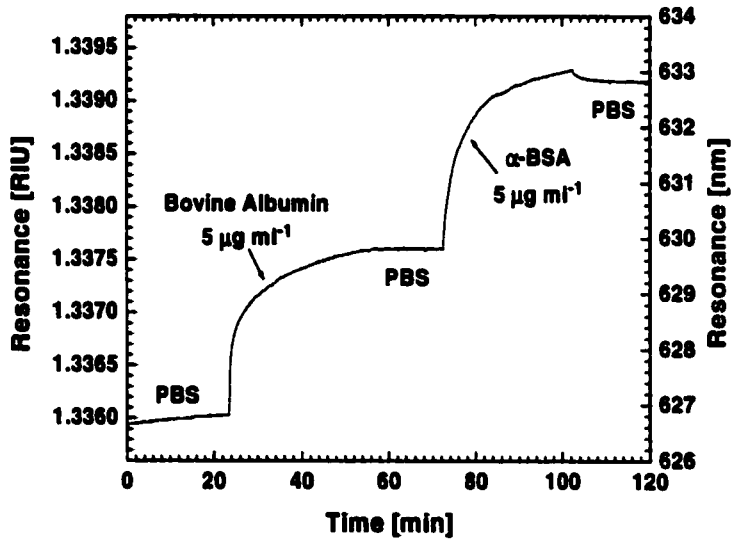

Fig. 5.10. Conventional SPR sensor response during a bovine albumin–anti-BSA immunoassay experiment. An SPR lightpipe configuration was used.

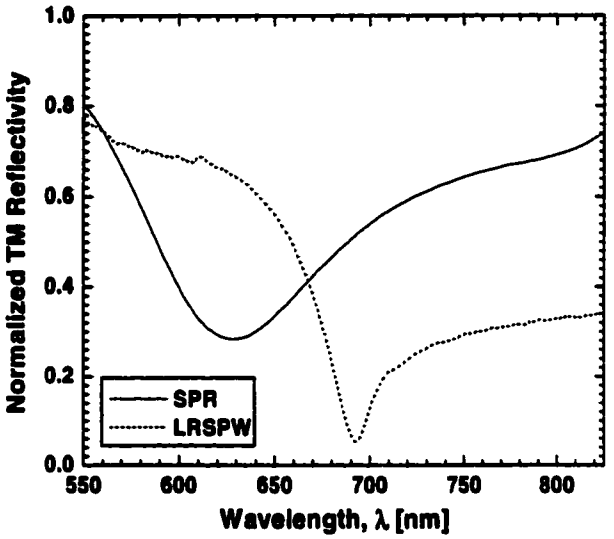

Fig. 5.11. Comparison of conventional SPR lightpipe and LRSPW sensor spectra used in the biosensing experiments described in the text. The SPR sensor spectrum was referenced to TE-polarized reflectivity; the LRSPW sensor, to TM-polarized reflectivity in air.

Table 5.2. Comparison of LRSPW and conventional SPR sensor performance during bovine albumin–anti-BSA immunoassay experiments.

Sensor Type	Resonance Width [nm]	Sensitvity nm RIU^{-1}	Averaging / Smoothing	Resolution nm	Resolution RIU
LRSPW	15	31 000	16 / 16	0.0058	1.9×10^{-7}
SPR	83	1 900	32 / 0	0.009	4.7×10^{-6}

5.5 Discussion of Experimental Results

The experimental results presented here demonstrate the use of long-range surface plasma waves to improve the resolution of SPR biosensing instruments. The combined effects of narrower resonance width and higher sensitivity provided an

order of magnitude improvement in the instrument resolution over a conventional SPR sensor.

Notes for Chapter 5

[1] G.G. Nenninger, Referenced Surface Plasmon Resonance Biosensor Using a Dual-Channel Planar Lightpipe, M.S. Thesis, University of Washington Department of Electrical Engineering (1998).

[2] G.G. Nenninger, J.B. Clendenning, C.E. Furlong, S.S. Yee, Reference-compensated biosensing using a dual-channel surface plasmon resonance sensor system based on a planar lightpipe configuration, Sensors and Actuators B 51 (1998) 38-45.

Chapter 6: Discussion of LRSPW Sensor Experimental Results

6.1 Sensor Resolution

Sensor resolution was determined based on the noise level of the resonance-locating algorithm over time. An interpolated tracking centroid method was used due to its good linearity and resistance to changes in light level and resonance depth during the course of the experiment. Averaging was set to the maximum level possible while still producing a new resonant wavelength value every 5 seconds. Thus, increased averaging was possible for higher light levels, improving the resolution of the sensor. In some cases, triangle-weighted smoothing of adjacent spectrometer pixels was used, which tended to improve resolution, although it may degrade the resonance shape by increasing the resonance width or raising the depth of the minimum. For a given smoothing value, s, the smoothing window was $2s - 1$ pixels wide, centered on the pixel to be smoothed. The central pixel value was weighted by s^{-1}, with the weighting reduced linearly to s^{-2} at the edge of the smoothing window.

The resolution of the resonant wavelength in nanometers was calculated by using a statistical analysis program to fit a second order polynomial to a stable or smoothly-varying section of the data, computing the standard deviation of the residuals from the curve fit. The resolution in nanometers was divided by the sensitivity to produce the resolution in RIU.

Table 6.1 summarizes the resolution of a number of LRSPW sensors. All of the sensors used gold layers 20 nm thick, resulting in a good balance between sensitivity and resonance width. The measured sensitivity for one sensor using a spectrometer with a photodiode detector array was roughly half that measured using a CCD detector. This degradation in the measured sensitivity resulted from the need to

use a large 50 micrometer diameter optical fiber rather than a single-mode fiber for the photodiode detector in order to produce sufficiently high light intensity. As a result, the wavelength resolution of the photodiode array spectrometer was not as good as that of the CCD spectrometer, causing the reflected spectrum to be broadened and appear to have lower sensitivity, as shown in Fig. 6.1.

Table 6.1. Summary of resolutions for experimental LRSPW sensors using 20 nm thick gold layers.

Teflon AF Buffer nm	Detector	Averaging and Smoothing		Resonance		Sensitivity nm RIU^{-1}	Resolution	
		Avg	Smooth	Depth	Width nm		nm	RIU
800	CCD	32	0	0.04	38	24 100	0.0062	2.6×10^{-7}
1000	Photodiode	4	0	0.17	43	19 700	0.0029	1.5×10^{-7}
1000	CCD	4	0	0.06	40	35 000	0.019	5.5×10^{-7}
1100	CCD	16	16	0.05	15	31 000	0.0058	1.9×10^{-7}
1200	CCD	16	0	0.25	53	30 200	0.023	7.9×10^{-7}
1400	CCD	1	16	0.57	14	23 300	0.055	2.3×10^{-6}
1600	CCD	8	0	0.70	14	32 900	0.042	1.3×10^{-6}

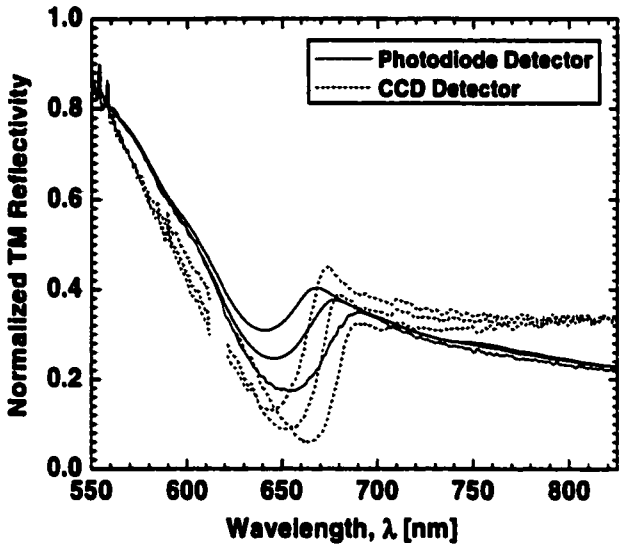

Fig. 6.1. Effect of degraded wavelength resolution of the spectrometer caused by a large-diameter optical fiber. A 50 μm diameter fiber was used for the photodiode detector, while a polarization-maintaining 3.4 μm (mode field diameter) single-mode fiber was used with the CCD detector.

6.2 Comparison Between Model and Experiment

Four characteristics of the LRSPW resonance were measured for LRSPW sensors with Teflon AF buffer layers varying in thickness from 800 nm to 1600 nm. The gold layer was 20 nm for these sensors. The characteristic measurements were the same as those of the design curves presented earlier in Chapter 3: resonance depth, resonance width, resonant wavelength, and sensitivity. Water was used as analyte, except for the sensitivity calibration, which used mixtures of water and ethylene glycol. The measurements listed in Table 6.2 were taken after adjusting the operating angle for the best resonance, as discussed in Section 5.2.

Table 6.2. Summary of resonance features for LRSPW sensors with various buffer layer thicknesses. A gold layer 20 nm thick was used for these sensors.

Teflon AF Buffer, nm	Resonance Depth	Resonance Width nm	Resonant Wavelength nm	Sensitivity nm RIU^{-1}
800	0.04	38	631	24 100
1000	0.06	40	660	35 000
1100	0.05	15	692	31 000
1200	0.25	53	741	30 200
1400	0.57	14	675	23 300
1600	0.70	14	737	32 900

Due to the difficulty of angular alignment, the optimum operating angle was not always achieved, causing possible variation from the design curves. However, in general the measurements of experimental LRSPW sensor approximated the trends of the design curves as the buffer layer thickness was varied. Experimental measurements are compared with design predictions in Fig. 6.2 through Fig. 6.5.

The resonance depth of the experimental LRSPW sensors was not as deep as predicted, a possible indication of poor coupling between the incident light and the surface plasmon (Fig. 6.2). However, the most likely sources of this discrepancy are angular spread of the beam and the finite spectral resolution of the spectrometer, which would tend to round off very narrow resonances, thereby limiting the depth of the resonance. Wider resonances, such as those for 800 - 1200 nm thick buffer layers, would tend not to be affected by the spectral resolution of the spectrometer. The very deep resonances for the sensors with 800 and 1100 nm buffer layers is an indication of good overall instrument performance, including sensor surface quality (primarily limited by the quality of the buffer layer), gold quality, and light collimation.

In Fig. 6.3, the resonance width of the experimental sensors compared favorably with predictions. However, in practice, experimental measurements of the resonance width were conducted using a method different than that used in the design

curves. In the design curves, the width was estimated using the side of the resonance toward shorter wavelengths and doubling the result, while both sides were used in the experimental measurements. Due to the asymmetry of the LRSP resonance minima seen in the experiments, the design curves would tend to over-predict the resonance width. No resonances narrower than 14 nm were observed experimentally. The ability of the instrument to measure narrower resonances is most likely limited by sensor surface quality and light collimation.

The resonant wavelength for the best resonance closely follows predictions as shown in Fig. 6.4. The single-mode fiber used in most of these measurements strongly attenuated wavelengths longer than 825 nm, limiting the ability to observe resonances at long wavelengths.

The sensitivity of the experimental LRSPW sensors followed the same variation over buffer thickness as the prediction of Fig. 6.5, although the magnitude was 40 percent lower than predicted. This difference may represent limitations in the refractive indices models for the materials used, since the sensitivity is highly dependent upon the relative dispersions of the materials used. Still, the experimental data shows good agreement with theory, considering the eight orders of magnitude covered by the predicted sensitivity.

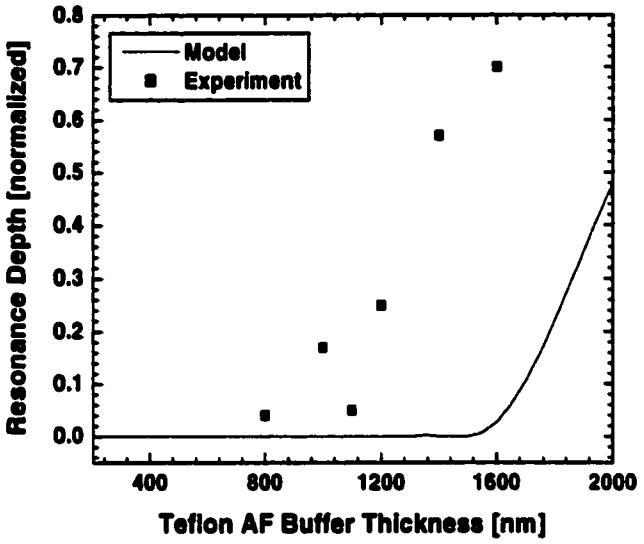

Fig. 6.2. Comparison between model and experiment for resonance depth as the buffer layer thickness was varied. Gold layer of the LRSPW sensor was 20 nm thick.

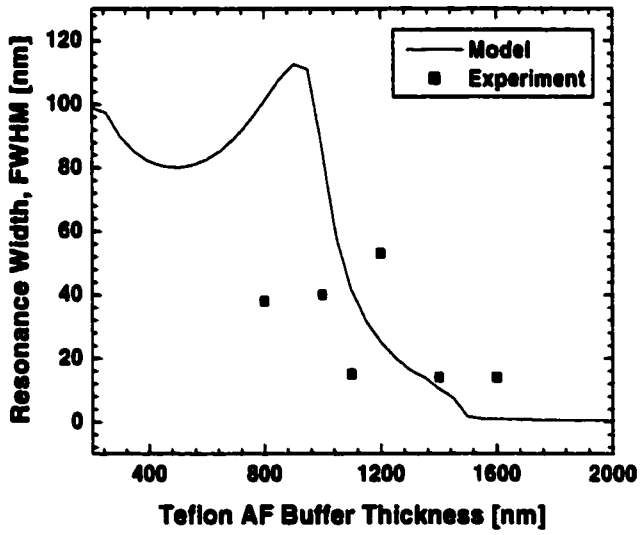

Fig. 6.3. Comparison between model and experiment for resonance width as the buffer layer thickness was varied. Gold layer of the LRSPW sensor was 20 nm thick.

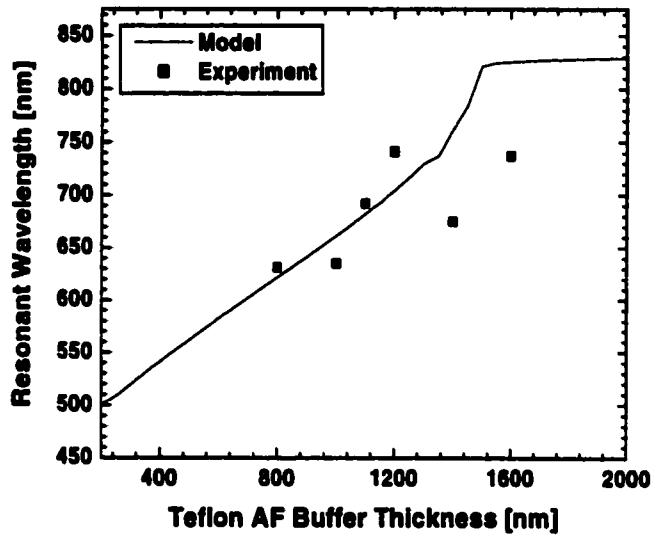

Fig. 6.4. Comparison between model and experiment for resonant wavelength as the buffer layer thickness was varied. Gold layer of the LRSPW sensor was 20 nm thick.

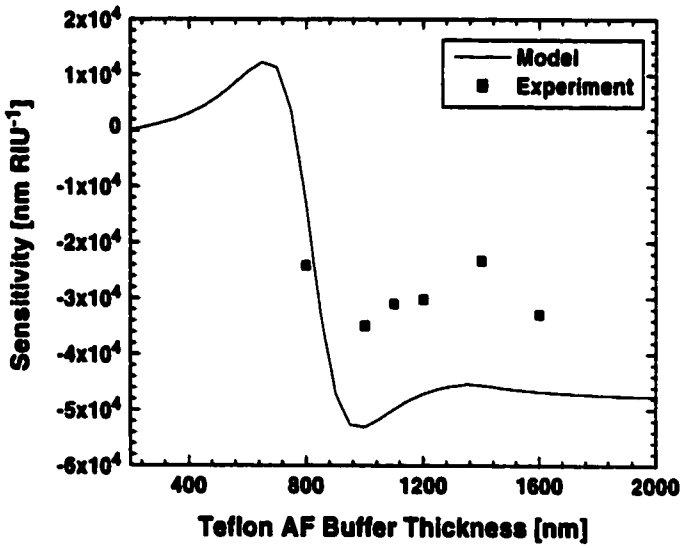

Fig. 6.5. Comparison between model and experiment for sensitivity as the buffer layer thickness was varied. Gold layer of the LRSPW sensor was 20 nm thick. The sensitivity was listed as a negative value for this figure when an increase in refractive index causes a decrease in resonant wavelength.

Chapter 7: SPR Sensor Data Analysis

Data analysis for a surface plasmon resonance sensor involves the conversion of raw spectral data into a resonant wavelength, angle, or other quantity modulated by the surface plasmon resonance. Generally, this process involves using an algorithm to determine the position (*e.g.* in wavelength or angle) of the resonance absorption feature. From there, a sensor calibration may be used to convert the sensor output to refractive index units, salinity, surface coverage, or another desired unit. The methods used for the SPR data analysis can have a large impact on the quality of the final data. Improper use of resonance-position determining algorithms can lead to effects such as increased noise levels or poor linearity.

7.1 Basic SPR Data Processing

The purpose of SPR sensor data processing is to use the spectral data to calculate the value of the desired output quantity, such as refractive index, generally over time. The goal of this data processing should be to produce an output with the lowest possible noise and lowest level of algorithm error achievable while still attaining the desired output rate. The resolution of SPR sensor systems is generally stated as the standard deviation of the output data, so that the resolution of a system producing an output in refractive index might be given as 1.0×10^{-6} RIU. If we consider the standard deviation to be the minimum resolvable change in the output of the sensor, then the noise level of the output data has direct implications for the detection limit of SPR-based biosensors, since the resolution will directly affect the lowest detectable amount of binding in a biosensing experiment. Improving the resolution of the SPR instrument will therefore allow for the detection of a lower concentration of the target agent present in the analyte.

7.1.1 Collecting Spectral Data

The first step in data processing of SPR sensor data is to load individual spectra for analysis. Conversion from the analog detector signal to a digital value is generally performed using an analog-to-digital (A/D) converter, which may be interfaced to a data processing computer in any of a number of methods. A/D converters are currently available which feature direct bus interfaces (such as ISA or PCI bus), serial interfaces (RS-232, USB, Ethernet), or other computer ports (PC-Card). In general, high-speed interfaces are desirable, as they reduce the overhead processing and time required to transfer the spectra from the spectrometer to the data processing computer, allowing more spectra to be collected in a given amount of time. Because data processing such as averaging uses more than one raw input spectrum per output value, the spectrometer sampling rate is usually faster than the output data frequency.

The frequency of the output data depends to a large part upon the use of the processed data. For instance, the purpose of many protein-protein interaction experiments is to calculate the kinetic constants for the on and off binding rates of the proteins, often on a time scale of seconds. For these calculations, there must be a sufficient number of output data points during the binding and unbinding curves to provide for calculation of kinetic constants with sufficiently low statistical uncertainty.

Many of our own experiments involve the detection of biological agents or antigen-antibody binding over a time scale of 5 to 60 minutes. In general, we have found an output data rate of 12 values per minute (5 seconds each) to be sufficient for our applications. Therefore, our data processing settings are generally set to produce an output value every five seconds. This requirement limits the amount of averaging and other time-consuming processing that we are able to use. Therefore, the use of higher light levels, which reduce the integration time needed to produce a full-scale

reading in the spectrometer detector, allows more time for other processing, such as collecting multiple samples for averaging, and can ultimately allow us to achieve a higher sensor resolution.

7.1.2 Averaging

Averaging is one of the most effective methods for reducing the noise level of the output data. In averaging spectra, the value of each pixel of the spectrum is averaged over a number of spectra taken sequentially over time. Absent some source of harmonic or correlated noise, the output spectra of the spectrometer are independent from each other. We have found no measurable noise correlation from one spectrum to the next in our own SPR sensor system. Therefore, averaging n spectra results in a decrease in the noise of the averaged spectra by a factor of $n^{-0.5}$, as given by the following relationship between the number of samples and the variance of each averaged pixel for independent noise [1]:

$$M_n = \frac{1}{n}\sum_{i=1}^{n} x_i$$
$$\sigma_{M_n} = \frac{\sigma_x}{\sqrt{n}} \tag{7.1}$$

where: x_i = sample of the value of one pixel

n = number of samples

M_n = sample mean of pixel

σ_x = variance of the pixel value

σ_{M_n} = variance of the sample mean

Averaging has a direct influence on the noise level of the output data, and by extension, the resolution of the instrument, improving the resolution by reducing its value by the same factor of $n^{-0.5}$. The amount of averaging possible will be limited by

the desired update rate of the output data. The total time required to average *n* spectra will be equal to *n* times the sum of the integration time plus the overhead time required to transfer the spectral data to the data processing computer. Depending on the interface protocol, the overhead time may not vary linearly with the number of spectra to be transferred, and may depend upon the speed of the processor used and the processor load.

7.1.3 Dark Current Correction and Referencing

Since the SPR minimum is generally observed as an attenuated reflection, the raw reflection spectrum must be adjusted for variations in the source light level and detector response across the spectrum.

The first correction needed is one for the dark current of the detector. Dark current, which is caused by leakage current in the detector itself, is the current which flows in the absence of illumination. The dark spectrum is the spectral signal resulting from the dark current. The dark current depends primarily upon the integration time and the temperature of the detector. Therefore, it is particularly important to take a new dark spectrum following a change in the integration time. The dark spectrum may be recorded by interrupting the light source to the SPR sensor and recording the spectral output after the detector signal has stabilized. It is generally better to use a shutter than to turn off a halogen white light source to make this measurement, since the light source will drift for some time following reapplication of power to the lamp. Some linear detectors include dark pixels which are masked from illumination. These pixels may be read with each spectrum, averaged, and then applied to the illuminated portion of the spectrum as a real-time dark current correction.

The reference spectrum compensates for a number of effects, including the spectrally-dependent intensity of the source, absorption or losses in the optical system, and spectral variation in the detector efficiency. Because a surface plasma

wave is TM-polarized, it is common to use a TE-polarized spectrum for the reference. However, it is also possible to use other non-resonant spectra, such as the TM-polarized spectra for an analyte with a refractive index high or low enough to shift the resonant wavelength out of the operating range of the spectrometer. An air reference would be one example, since the refractive index of air is near 1.0. The reference spectrum should be corrected for dark current by subtracting the dark spectrum.

The averaged raw spectra from the spectrometer are normalized by first subtracting the dark spectrum and then dividing by the reference spectrum. Fig. 7.1 shows the relationship between these spectra.

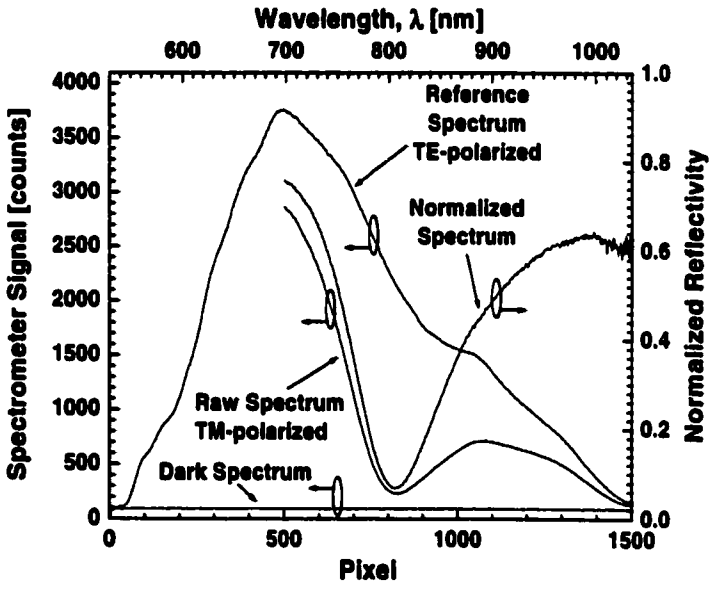

Fig. 7.1. Example of how the dark and reference spectra are used to correct the raw spectrum and produce a normalized spectrum.

7.1.4 Spectral Smoothing

Spectral smoothing is the application of a smoothing algorithm to each spectrum. Assuming that the noise on each pixel is independent, the noise of each

pixel in the smoothed spectra will be less. However, the noise of the smoothed spectrum is correlated from pixel to pixel as a result of the smoothing algorithm. In many instances, the reduction in noise resulting from smoothing will be offset by an increase in the noise of the output data caused by the correlation of the noise between pixels. Smoothing may be useful and may reduce the overall noise of the output data for some resonance-position finding algorithms, particularly those which use a small number of pixels for some portion of their calculation. Smoothing effectively reduces the noise level of these few pixels, reducing the level of the noise propagating through the algorithm.

Smoothing may also have undesirable effects depending on the implementation of the smoothing algorithm and the spectrum. For very narrow resonances, such as those occurring for sensors based on long-range surface plasma waves, smoothing may change the shape of the spectrum and reduce the spectral depth. To reduce distortion of the spectrum, we have used a triangle weighting algorithm which weights the pixels near the pixel being smoothed more heavily than those further away. For a given smoothing value, s, the smoothing window is $2s - 1$ pixels wide, centered on the pixel to be smoothed. The central pixel value is weighted by s^{-1}, with the weighting reduced linearly to s^{-2} at the edge of the smoothing window. The algorithm is described by:

$$x_{sm,i} = \frac{\sum_{j=-(s-1)}^{s-1} \left(s - |j|\right) x_{i+j}}{s^2} \tag{7.2}$$

where: x_i = value of pixel i

$x_{sm,i}$ = smoothed value of pixel i

s = smoothing value

7.1.5 Determining the Resonance Position

A variety of data-processing algorithms have been used to determine the position of the SPR minimum. These methods include quadratic or other regression curve fits [2, 3], a center-of-mass or centroid method [4], locally weighted parametric regression [5], and optimal linear data analysis [6].

The centroid method for determining the resonance position of an SPR-modulated spectrum is a simple method which finds the geometric center of the resonance minimum. The centroid algorithm is given by:

$$C = \frac{\sum_i i(x_{thresh} - x_i)}{\sum_i (x_{thresh} - x_i)} \tag{7.3}$$

where: C = centroid

x_i = spectrum pixel value i

x_{thresh} = threshold value

Note that only pixels with values falling below the threshold value x_{thresh} should be used in the calculation of the centroid. The threshold is an important parameter which affects the noise level of the centroid output. A higher threshold value will generally reduce the centroid noise by including more pixels in the calculation of the resonance position.

One disadvantage of the simple centroid algorithm is that it is susceptible to changes in the spectrum which cause the spectrum to be raised or lowered relative to the threshold, such as changes in the light level. To reduce this sensitivity, we have developed a modified centroid algorithm we call the interpolated tracking centroid

algorithm. This algorithm consists of two interrelated portions: a tracking algorithm and an interpolation routine.

The tracking algorithm uses a tracking span set by the operator to follow a resonance as it moves in the spectrum. The tracking span is the distance between two pixels on opposite sides of the resonance dip. The algorithm looks in the vicinity of the last known resonance position and positions the tracking span such that the endpoints have equal values. Linear interpolation is used between pixels so that the tracking span position does not have to fall on a discrete pixel position. A narrower resonance feature would be tracked using a shorter tracking span. In general, we set the tracking span to be roughly equal to the full width at half minimum.

The tracking algorithm provides a general method for tracking arbitrary resonance features. For instance, it has been used to track multiple resonances within the same spectrum simultaneously [7, 8, 9].

The second portion of the interpolated tracking centroid algorithm takes advantage of the continuous positioning of the tracking span within the discrete spectrum. The linearity of the centroid calculation is improved by weighting the end pixels less than a full pixel. The weighting corresponds to the fraction of the pixel included within the tracking span. Fig. 7.2 illustrates this interpolation process, which eliminates an algorithm jump which would otherwise occur when the tracking span moves to the next discrete pixel.

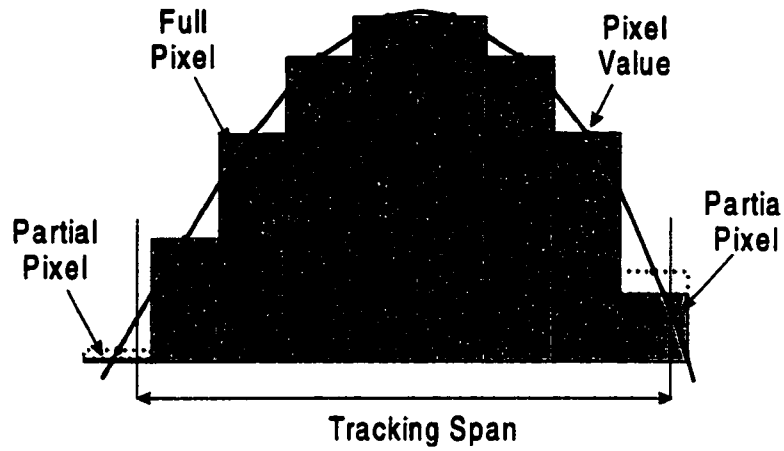

Fig. 7.2. Interpolated centroid method used in the interpolated tracking centroid algorithm. The contributions of the end pixels are reduced according to their fraction contained within the tracking span.

Notes for Chapter 7

[1] A.W. Drake, Fundamentals of Applied Probability Theory. McGraw-Hill Book Company, New York, 1967.

[2] E. Stenberg, B. Persson, H. Roos, C. Urbaniczky, Quantitative determination of surface concentration of protein with surface plasmon resonance using radiolabeled proteins, Journal of Colloid and Interface Science 143 (1991) 513-526.

[3] S. Sjölander, C. Urbaniczky, Integrated fluid handling system for biomolecular interaction analysis, Analytical Chemistry 63 (1991) 2338-2345.

[4] K. Kukanskis, J. Elkind, J. Melendez, T. Murphy, G. Miller, Detection of DNA hybridization using the TISPR-1 surface plasmon resonance biosensor, Analytical Biochemistry 274 (1999) 7-17.

[5] K.S. Johnston, K.S. Booksh, T.M. Chinowsky, S.S. Yee, Performance comparison between high and low resolution spectrophotometers used in a white light surface plasmon resonance sensor, Sensors and Actuators B 54 (1999) 80-88.

[6] T.M. Chinowsky, L.S. Jung, S.S. Yee, Optimal linear data analysis for surface plasmon resonance biosensors, Sensors and Actuators B 54 (1999) 89-97.

[7] J. Homola, H.B. Lu, S.S. Yee, Dual-channel surface plasmon resonance sensor with spectral discrimination of sensing channels using dielectric overlayer, Electronics Letters 35 (1999) 1105-1106.

[8] J. Homola, H.B. Lu, G.G. Nenninger, S.S. Yee, C.T. Campbell, Novel approach to multichannel SPR sensing, SPIE Conference on Microsensors and Applications II, Proceedings of the SPIE 3857 (1999) 198-206.

[9] J. Homola, H.B. Lu, G.G. Nenninger, J. Dostálek, S.S. Yee, A novel multichannel surface plasmon resonance biosensor, Sensors and Actuators B 76 (2001) 403-410.

Chapter 8: Evaluating the Noise-Based Performance of SPR Sensor Data Analysis Methods

With all of the methods available for SPR sensor data analysis, a standard method for optimizing and evaluating the performance of data analysis methods is useful. In this chapter, we evaluate the performance of two closely related algorithms for determining the position of an SPR resonance: the simple centroid algorithm and the interpolated tracking centroid algorithm. The specific algorithm descriptions were provided in Chapter 7. This chapter is not intended to serve as a side-by-comparison of all available methods; rather, it is intended to provide a model for objectively evaluating the performance of SPR data processing algorithms.

The performance of the simple centroid and interpolated tracking centroid algorithms will be evaluated on the basis of linearity, noise, and susceptibility to instrument drift effects.

8.1 Linearity

The linearity error for the simple centroid and tracking centroid algorithms was determined using an analytical fit to an experimental SPR minimum. A Lorentzain curve fit was modified by the addition of a linear term so as to better fit the asymmetrical SPR minimum. The analytical curve was used as a noiseless input to the SPR data analysis system and was gradually shifted in resonant wavelength as the outputs of each algorithm were recorded. The error between the actual position of the minimum and the position computed by the algorithms was then plotted, as in Fig. 8.1. As this figure shows, the simple centroid algorithm has a larger linearity error than the tracking centroid algorithm.

The linearity of the tracking centroid algorithm could be further improved by using a higher order fit to the end pixels in the tracking span when interpolating to find the position of the tracking span. The use of a linear interpolation introduces a

linearity error which propagates through the algorithm. However, the error is two orders of magnitude below typical noise levels and so is not likely to be problematic for some applications. The effect of linearity errors on the sensitivity deviation of sensors used for biomolecular interaction kinetic analyses is described in Reference [1].

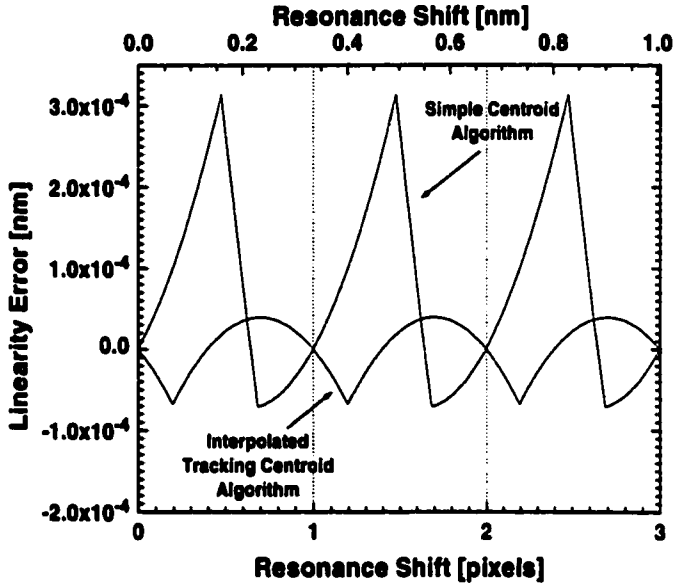

Fig. 8.1. Linearity error for the simple centroid and tracking centroid algorithms.

The linearity errors are continuous for both algorithms, with no sudden jumps in error as the resonance is shifted. Discontinuities in the linearity error of a resonance-locating algorithm are a particular concern, as they can result in the output of the algorithm jumping between widely-separated output values as the input noise forces solutions on opposite sides of the step. The resulting resonance data shows a hashed appearance, as in Fig. 8.2. The noise level will show a sudden increase as the algorithm shifts through the region of the discontinuity. These effects will appear periodically with resonance shift, as they are usually related to the method for

selecting pixels to be considered by the algorithm. Artifacts caused by algorithm discontinuities have been demonstrated in a number of papers [2, 3, 4].

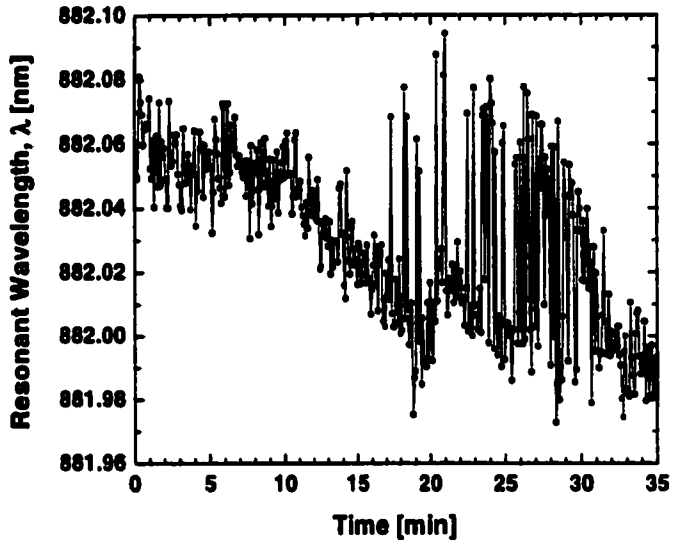

Fig. 8.2. Sudden increase in noise level caused by discontinuities in the resonance-locating algorithm. A tracking centroid algorithm with no interpolation between pixels was used for this example.

The simple centroid algorithm is continuous because the pixels at the edge of the window considered in the calculation are given a very low value by subtracting the pixel value from the cutoff, which is close in value to the end pixels. The interpolated tracking centroid interpolates between pixels to provide a smooth transition as the tracking span moves with the resonance minimum, thereby avoiding discontinuities.

It is important to ensure that any attempts to improve the linearity of an algorithm do not increase the output noise level, unless the trade-off is necessary for the experiment. For instance, a weighted centroid algorithm presented in one paper as a way to improve linearity causes the noise level to be doubled [4]. The noise

increase occurs because the value of each pixel is squared, thereby doubling the standard deviation of each pixel value:

$$C_w = \frac{\sum_i i(x_{thresh} - x_i)^2}{\sum_i (x_{thresh} - x_i)^2} \tag{8.1}$$

where: C_w = weighted centroid

x_i = spectrum pixel value i

x_{thresh} = threshold value

8.2 Characterizing Noise in SPR Sensors

Prior to any analysis of noise in SPR sensors, the sources of noise must be identified and quantified. There are many sources of variation in the measured output of an SPR sensor, including actual changes in the refractive index of the analyte caused by binding or temperature changes, drift caused by mechanical or thermal instability, and noise caused by the detector and electronics. We will discuss the sources of instrument noise, defined as short-term random variations in the measured spectra.

8.2.1 Sources of Noise

The largest source of noise for the SPR sensor system is typically the detector noise. Photons arrive at the spectrometer detector with a Poisson distribution, resulting in shot noise which increases with the square root of the intensity [5]. Other sources of noise in the detector circuitry include the readout noise of the electronics processing the signal from the detector as well as noise caused by random variations in the detector dark current.

8.2.2 Magnitude of Noise

The magnitude and standard deviation of the spectral noise may be measured by recording spectra over time and calculating the distribution of the noise versus the mean detector level. Fig. 8.3 shows an example of detector noise for a CCD detector. As expected, the standard deviation of the noise increases with the square root of the intensity, as is typical of shot noise.

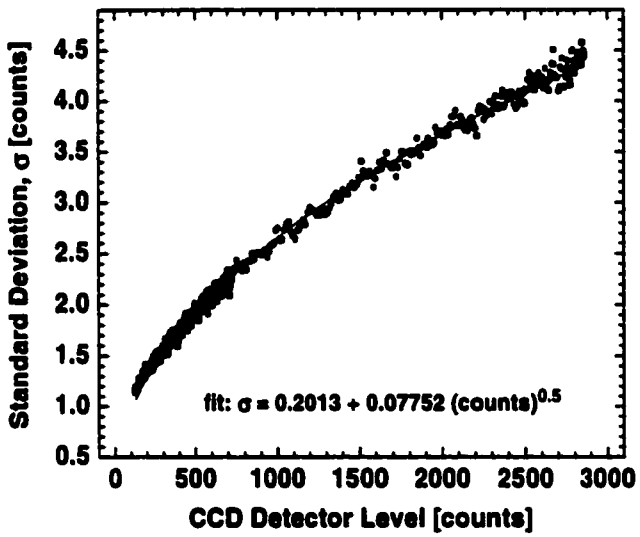

Fig. 8.3. Measured CCD detector noise level with averaging set to 16 spectra. The noise increases with the square root of the intensity, characteristic of detector shot noise. Spectrometer: Ocean Optics S2000 model.

If the noise of the normalized spectra is measured, then the effect of the signal-to-noise ratio can be seen. The lower source light level for the right side of the resonance dip (see Fig. 7.1) produces a lower signal-to-noise and an increased noise level. If the spectral noise is plotted against the value of the normalized reflectivity, as in Fig. 8.4, the noise bifurcates into two different branches, corresponding to the two sides of the resonance minimum.

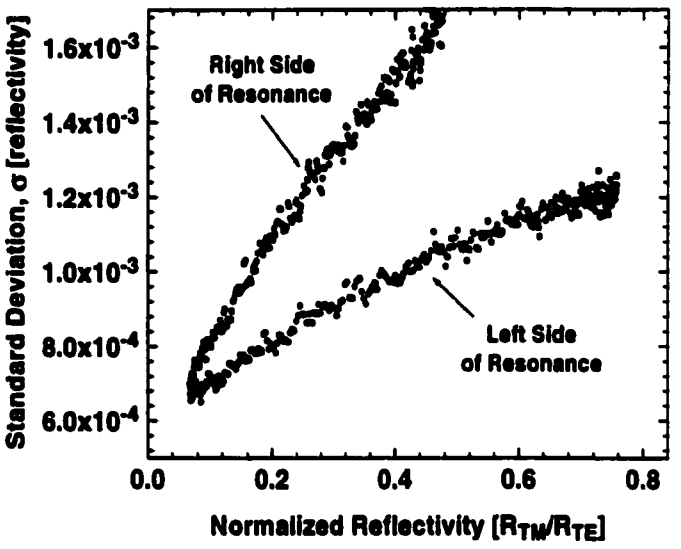

Fig. 8.4. Measured spectral noise for an SPR spectrum, plotted versus the normalized spectral level. Due to a decrease in the source light level toward longer wavelengths, the noise of the right side of the resonance is higher than the left side. Averaging was 16 spectra.

8.2.3 Statistical Distribution and Correlation

Since the detector shot noise is the dominant source of the overall spectral noise, and the shot noise is comprised of a large number of independent random events, we would expect the distribution of the spectral noise to be normal or Gaussian due to the Central Limit Theorem [6]. As shown in Fig. 8.5, the distribution is indeed Gaussian.

Fig. 8.6 demonstrates that there is no significant correlation between spectra taken at different times. Therefore, averaging of spectra should reduce the noise level with the square root of the number of spectra averaged, as discussed earlier.

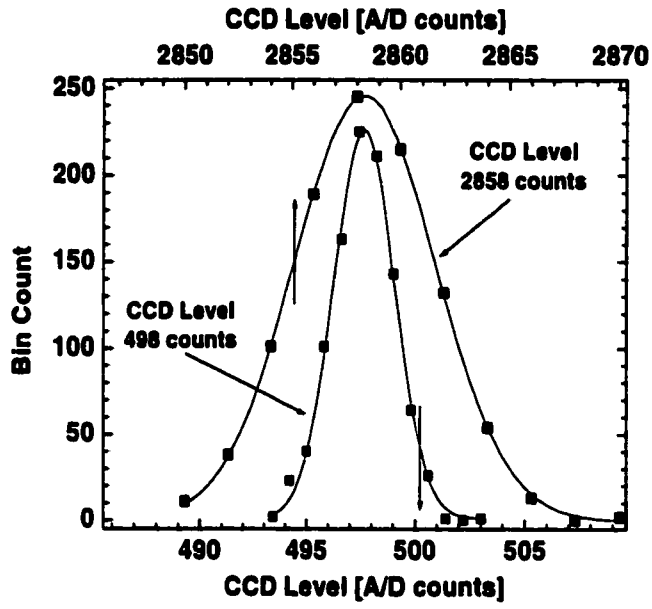

Fig. 8.5. Measured statistical distribution of noise from a CCD detector at two different light levels, fit with Gaussian curves.

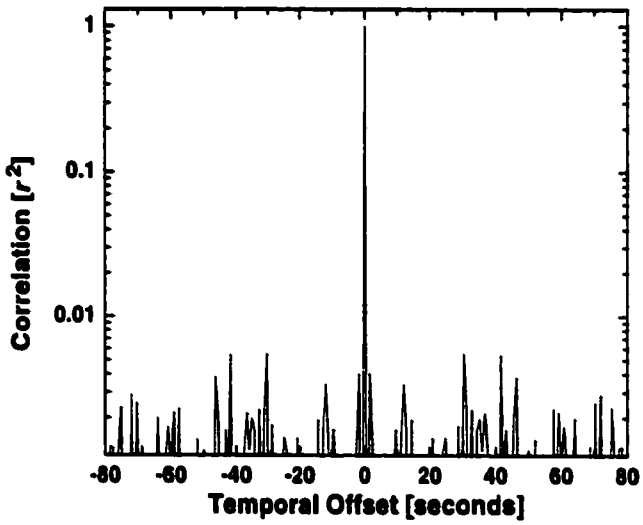

Fig. 8.6. Autocorrelation of the noise for a single detector element, showing no correlation over time.

8.3 Predicting SPR Data Analysis Algorithm Performance

It is possible to predict the response of SPR data analysis algorithms to detector and other sources of noise, as well as the response to drift causing a real or apparent shift in the light level through the detector. Prediction of the overall noise-based resolution of the SPR sensor involves propagating the measured instrument noise (*e.g.*, dark current, detector noise) through the algorithm to determine the effect on the algorithm output. Predictions of the drift response of SPR data analysis algorithms may be performed by changing the shape of the resonance minimum to simulate changes in the instrument light levels or other effects and noting the effect on the calculated resonant wavelength or angle.

8.3.1 Predicting SPR Sensor Measurement Noise

The noise of the resonance position data for an SPR sensor is an important measure, as it is the noise-based resolution of the instrument. In this section, we will derive an expression for calculating the noise of the centroid algorithm based on the measured noise levels of the spectrometer and data processing system.

The variance of the centroid, given by the definition of variance [6], is expressed as:

$$\sigma_c^2 = E\{C^2\} - E\{C\} \tag{8.2}$$

If we use the change in the centroid, dC, and assume that the expected value of dC is zero because the noise is zero-centered and Gaussian, then Eq. (8.2) simplifies to:

$$\sigma_c^2 = E\{dC^2\} \tag{8.3}$$

The differential dC is made up of contributions from each discrete pixel i:

$$dC = \sum_i \frac{\partial C_i}{\partial x_i} dx_i \tag{8.4}$$

Therefore, Eq. (8.3) can be rewritten in terms of x_i:

$$\begin{aligned} \sigma_c^2 &= E\left\{\left(\sum_i \frac{\partial C_i}{\partial x_i} dx_i\right)^2\right\} \\ &= \int_{-\infty}^{\infty} \left(\sum_i \frac{\partial C_i}{\partial x_i} dx_i\right)^2 f(x)\, dx \end{aligned} \tag{8.5}$$

where f is the statistical distribution of the noise. The partial derivative of the centroid for the change caused by the change of value x_i of pixel i is given by:

$$\frac{\partial C_i}{\partial x_i} = \frac{\sum_i i(x_{thresh} - x_i)}{\left(\sum_i (x_{thresh} - x_i)\right)^2} - \frac{i}{\sum_i (x_{thresh} - x_i)} \tag{8.6}$$

We can assume that the magnitudes of the cross products in the square of the summation in Eq. (8.5) are much less than the squared terms because the noise is independent, so that the square of the summation is approximated by the summation of the squares, giving:

$$\begin{aligned} \sigma_c^2 &= \sum_i \left(\frac{\partial C_i}{\partial x_i}\right)^2 \int_{-\infty}^{\infty} x_i^2 f(x_i)\, dx_i \\ &= \sum_i \left(\frac{\partial C_i}{\partial x_i}\right)^2 \sigma_{x_i}^2 \end{aligned} \tag{8.7}$$

where $\sigma_{x_i}^2$ = variance of the noise of pixel x_i

Since the variance of the pixel noise is measurable or can be estimated based on the measured detector noise and estimated light levels for a given resonance

spectrum, Eq. (8.7) provides a method for estimating the noise of the centroid algorithm. The standard deviation of the centroid noise, σ_c, is simply the square root of the variance.

Fig. 8.7 shows a comparison between predictions made using Eq. (8.7) and data measured from an actual SPR experiment using the simple centroid algorithm. As the number of pixels included in the centroid calculation is increased by raising the threshold value, the standard deviation of the noise decreases, since a better estimate of the resonance position is provided by more pixels. As the span of the centroid continues to increase, the statistical advantage of an increased number of samples is offset by the increasing noise levels of the higher-noise pixels away from the center of the resonance (see Fig. 8.4), causing the noise of the centroid to increase slightly. The predicted noise levels are slightly lower than experimental values due to the fact that independent noise was assumed in the predictions. Instrument readout noise in the spectrometer system as well as motion of the SPR minimum over time will cause a slight amount of correlation between the data for nearby pixels.

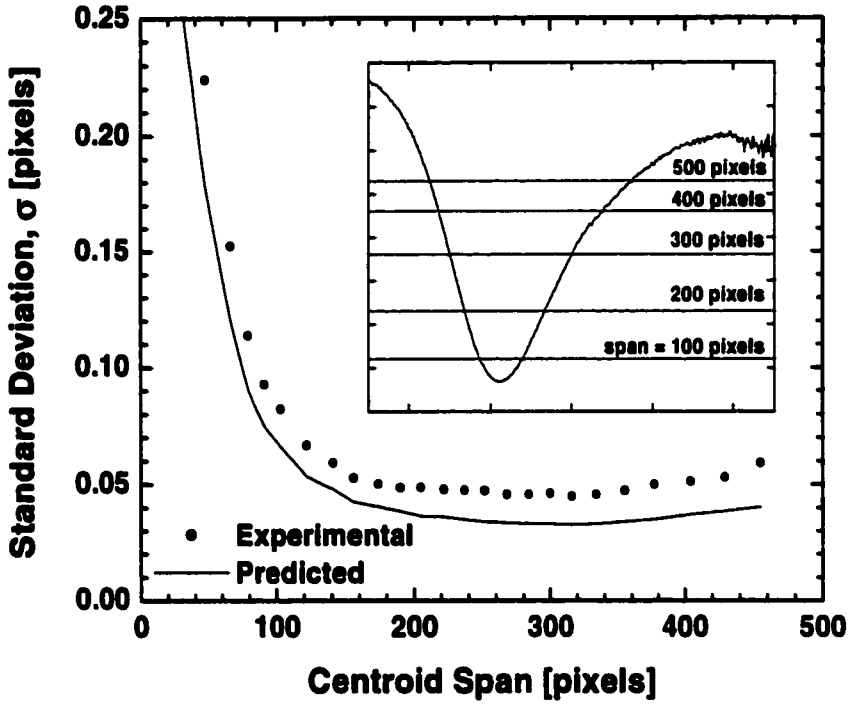

Fig. 8.7. Comparison between experimental noise levels of the measured resonance position and predictions using Eq. (8.7) as the number of pixels included in the algorithm is increased by raising the threshold value. Inset graph shows pixel spans in relation to the resonance minimum.

8.3.2 Predicting Effects of Instrument Drift

Variations in the SPR signal over a longer time period than noise is often referred to as instrument drift. Drift in SPR measurements results from a number of sources, some of which can be reduced or compensated for in the design of the experiment. These sources of drift may be divided into two major types: those which cause a true change in the refractive index near the sensor surface, and those which cause apparent changes in the sensor response actually due to optical, mechanical, or

thermal instabilities. We will refer to these two categories as first-order and second-order sources.

8.3.2.1 First-Order Sources of Drift

Non-specific binding between the sensor surface and a non-target molecule may produce a false indication of binding during a biosensing experiment by increasing the refractive index of the analyte at the surface of the sensor in the same way that a target molecule would. As non-specific interactions are less tightly bound than true antibody-antigen binding, the non-target material may gradually wash off during the experiment, producing a drifting baseline. From the standpoint of a single SPR sensor channel, non-specific interaction is indistinguishable from specific interaction without additional corrections to the experiment. A wash step may be used to flush less-tightly bound material from the surface following binding of the target analyte, thereby producing a measure of the material tightly bound to the functionalized sensor. The use of a reference channel may be helpful in providing real-time compensation for non-specific binding effects [7, 8, 9, 10]. Such reference channels become vital with complex samples, such as milk containing a toxin or pesticide, where the refractive index change from non-specific interaction of complex proteins and fats with the sensor is much higher than the change caused by a low concentration of the target.

Temperature changes may cause instrument drift both through changes in the refractive index of the analyte or through second-order effects such changes to the spectral characteristics of the light source or efficiency of the detector. Referencing may be used to correct first-order effects of temperature, namely the 1×10^{-4} RIU/C thermal sensitivity of the refractive index of water [8]. However, residual drift error will remain in the measurement, so it may also be helpful to attempt to control the temperature of the sensor and its temperature-sensitive components.

In our own SPR sensor system, we have the option of using one or more systems for reducing the thermal sensitivity of the measurements. First, enclosing the entire sensor in a large, thermally-insulating enclosure can greatly reduce the effect of temperature changes caused by circulating air. A light-level controller using a feedback system maintains the intensity and spectral characteristics of the light source despite changes in ambient temperature. For tighter control of the temperature of the SPR sensor, a Peltier junction with thermal controller is used to keep the sensor prism and substrate at a near-constant temperature. A heat exchanger is used to equalize the temperature of the incoming analyte with the sensor before entering the flow cell.

8.3.2.2 Second-Order Sources of Drift

Since first-order sources of drift cause an actual change in the refractive index of the analyte, there is little that can be done to improve the data processing algorithm for determining the location of the SPR minimum to be less susceptible to these effects without using more advanced techniques such as referencing. However, second-order sources of drift, such as changes in the spectral characteristics of the light source and detector as the temperature varies, often change the SPR spectrum in ways that are distinguishable from a true change in the refractive index. Some of these sources of spectral drift could be compensated for through the use of a real-time light reference, such as the use of separate spectrometer channels to measure the TM-polarized SPR-modulated spectrum and the unmodulated TE-polarized spectrum. However, even without real-time spectral referencing, the algorithm for determining the resonant wavelength or angle can be designed to minimize susceptibility to these effects.

For simpler analysis, we have combined all sources of spectral variation into one factor and have considered it as a change in the intensity of the light source. We have assumed that real-time spectral referencing is not used, as it is common to take a reference spectrum measurement at the beginning of the experiment. Fig. 8.8

illustrates two scenarios for changes to the intensity of the light source in an SPR sensor: a uniform increase in intensity, and a linear fractional change in the intensity as a function of wavelength. To separate the contributions of uniform and linear changes in the light intensity, the two linear change scenarios have been selected to be unity at the centroid of the SPR spectrum.

The interaction between the contributions of spectral changes and the resonance-locating algorithm may be complex. For instance, the geometric centroid of the spectrum does not change with scaling of the light level (such as the uniform increase in intensity in Fig. 8.9), but the threshold method used by the simple centroid algorithm for selecting pixels to be included in the calculation will include fewer and fewer pixels as the light level increases. Due to the asymmetry of the resonance curve, the simple centroid will show an artificial drift of the resonance position. The interpolated tracking centroid algorithm discussed earlier is immune from this effect because the tracking span will be positioned in the same position relative to the overall resonance minimum.

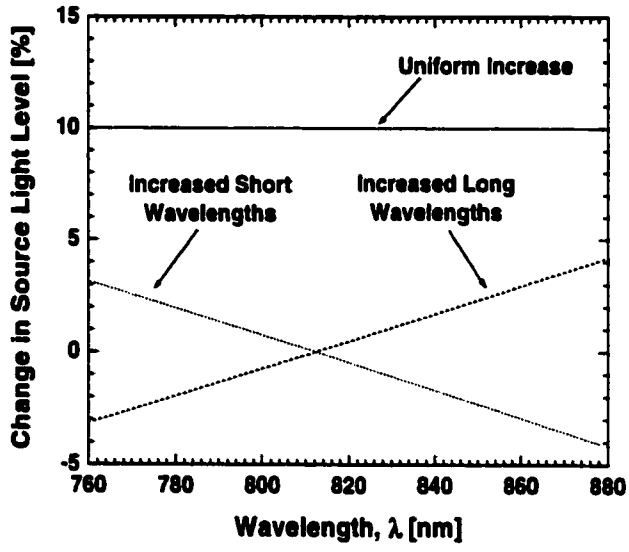

Fig. 8.8. Scenarios for changes to the source light level in an SPR sensor system.

The spectral effects of changes in the light source intensity which vary linearly with wavelength are illustrated in Fig. 8.10. The effects of the spectral changes of Fig. 8.8 on the simple centroid and tracking centroid algorithms are summarized in Table 8.1. These effects are specific to the case of the spectra used here, and are not necessarily general effects.

Table 8.1. Summary of the effects of light source spectral changes on the simple centroid and interpolated tracking centroid algorithms for given scenarios.

Type of Spectral Change	Effect on the Apparent Resonant Wavelength (scenarios of Fig. 8.8, spectra of Fig. 8.9 and Fig. 8.10)			
	Simple Centroid Algorithm		Tracking Centroid Algorithm	
	direction	magnitude	direction	magnitude
uniform increase	decrease	1.17 nm	no change	--
linear increase with wavelength	decrease	1.12 nm	decrease	0.97 nm
linear decrease with wavelength	increase	1.23 nm	increase	0.90 nm

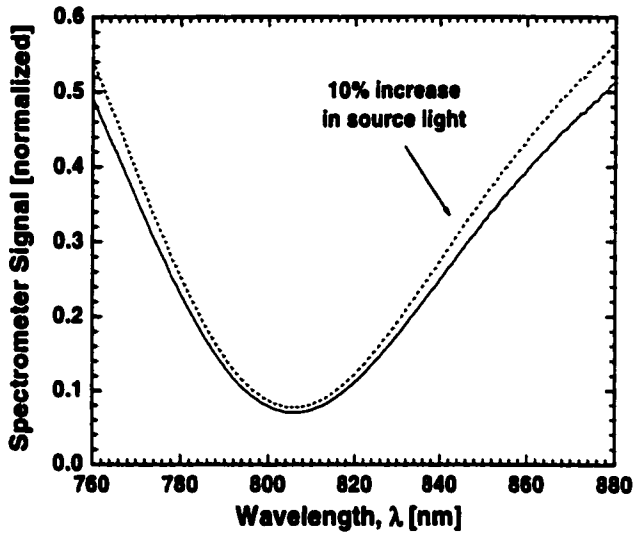

Fig. 8.9. Effect of a uniform increase in source light level on the output spectrum of an SPR sensor.

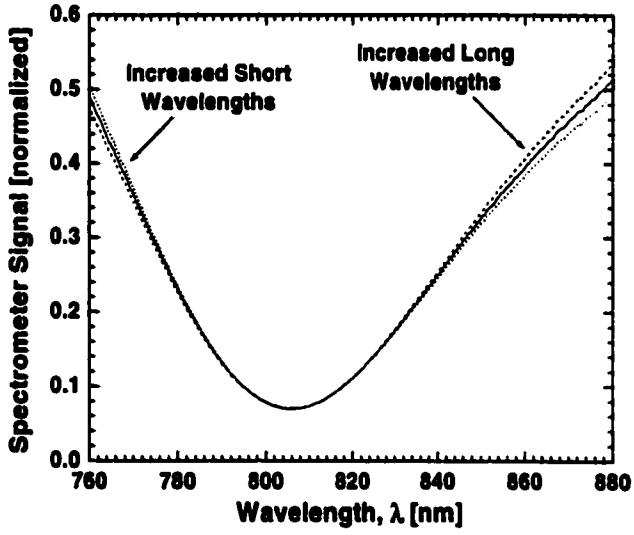

Fig. 8.10. Changes to an SPR spectrum caused by the addition of a constant light intensity across the spectrum.

8.4 Experimental Evaluation of SPR Data Analysis Algorithms

We have shown how the effect of noise and drift on SPR data analysis algorithms can be predicted. In this section, we use experiments to validate the predictions and further evaluate the performance of the algorithms.

8.4.1 Measured SPR Sensor Noise

The most basic goal for SPR data processing algorithms is to produce as an output the position of the resonance minimum over time with the lowest possible noise consistent with the required data update rate and processing requirements. To evaluate the performance of the simple centroid and tracking centroid algorithms for a variety of parameter settings, a standard data set consisting of spectra collected during an SPR experiment was constructed. The SPR sensor was temperature-stabilized and used a feedback-controlled light source to reduce sources of drift. A sequence of 1000 spectra, collected at a rate of one sample per 0.8 seconds with each spectrum consisting of the average of 16 raw spectra, was saved to a data file for use in the analyses. A plot of the resonant wavelength of this data set over the 1000 spectra is provided in Fig. 8.11, demonstrating the low drift of the data set.

This standard spectral data set was used as the input for the same data analysis software used in our real-time experiments, with the saved data substituting for averaged spectral data from the spectrometer and analog-to-digital converter. The data set was analyzed multiple times, with each case using a different number of pixels within the span of the centroid. The simple centroid threshold value was set to select the same number of pixels as the tracking span of the tracking centroid algorithm.

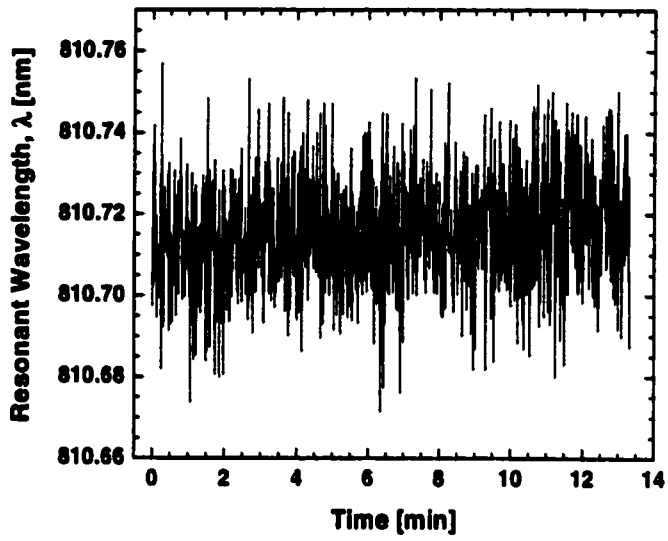

Fig. 8.11. Measured resonant wavelength for an SPR sensor using a standard saved spectral data set. This data set was used to compare the performance of SPR data processing algorithms.

The results of the noise performance of the simple centroid and tracking centroid algorithms are summarized in Fig. 8.12. With the exception of the unsmoothed tracking centroid, the lowest noise levels occur when the centroid span is approximately 300 pixels, roughly the full width at half minimum (FWHM) for the SPR minimum.

The increased noise of the tracking centroid when smoothing is not used is indicative of the way in which the values of the end pixels of the tracking span are used, as they set the position of the tracking span as well as the threshold used in the centroid calculations. Smoothing the spectrum improves the noise response of the tracking centroid by reducing the noise of these end pixels. A similar improvement in the noise level of the tracking centroid could be achieved without smoothing by using

more pixels when determining the position of the tracking span and the threshold value.

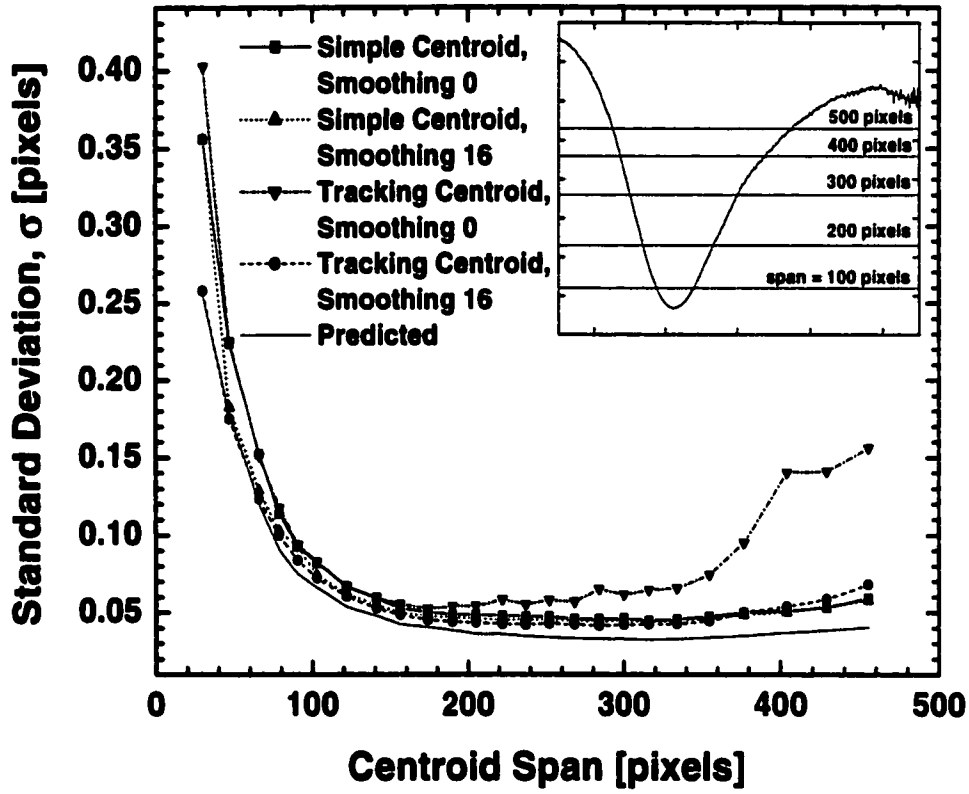

Fig. 8.12. Measured noise levels of the resonant wavelength for the simple centroid and tracking centroid algorithms as the centroid span increases. The effect of triangle smoothing, set to either 0 or 16, is also shown.

8.4.2 Measured Experimental Drift

In practice, changes in the spectral characteristics of the SPR spectrum caused by drift may be the convolution of several sources. To test the drift predictions of the preceding section, the spectral characteristics of an experimental SPR sensor were modified and the effects on the simple centroid and tracking centroid algorithms were measured.

Fig. 8.13 shows the effect of a change in the light source power, increasing from 31 W to 38 W and then returning to 31W, as well as an interval in which the integration time was changed from 3 ms to 5 ms. The effect of these changes on the spectrum of the SPR sensor is shown in Fig. 8.14. Back-calculating the equivalent light intensity changes produces the plots of Fig. 8.15.

From Fig. 8.15, the increase in the lamp power has caused a blue-shift in the emission characteristics of the lamp, so that the shorter wavelengths show a larger increase in intensity than longer wavelengths. Using Fig. 8.15 and the theoretical predictions of Table 8.1, we would expect the lamp power increase to have a effect combining a uniform increase in intensity and a linear decrease in intensity with wavelength. These effects should cause an increase in the resonant position calculated by the tracking centroid algorithm, while the effect on the simple centroid will depend upon the magnitude of the contributions, which have opposing effects. In this case, the effect of the uniform increase in intensity overwhelms the linear decrease in intensity with wavelength, so the calculated resonant wavelength decreases.

The integration time change of Fig. 8.13 is equivalently a uniform increase in the source light intensity, and therefore should have little or no effect on the tracking centroid, while causing the calculated resonant wavelength of the simple centroid algorithm to drop.

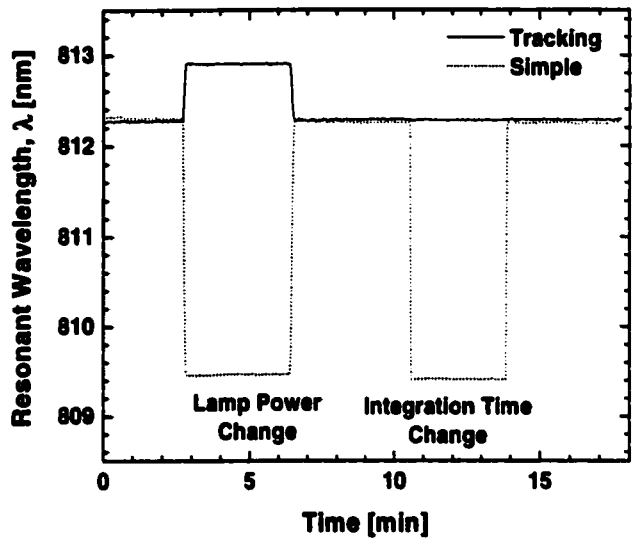

Fig. 8.13. Effect of a change in the light source power (from 31 W to 38 W) and a change in the integration time (from 3 ms to 4 ms) on the response of the simple centroid and tracking centroid algorithms.

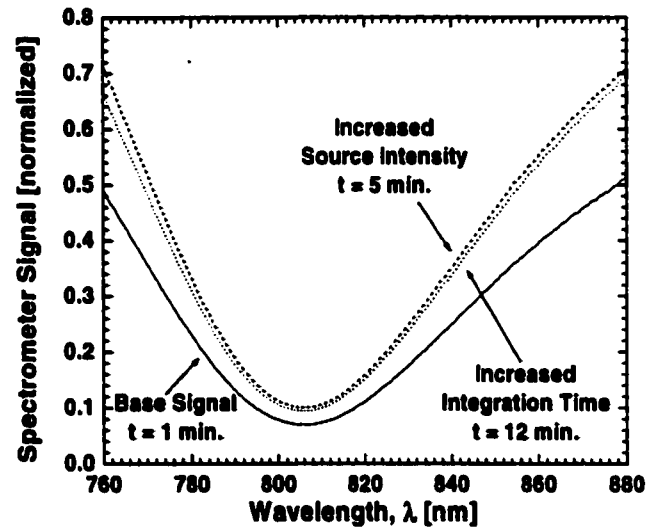

Fig. 8.14. Spectral change corresponding to the lamp power and integration time changes of Fig. 8.13.

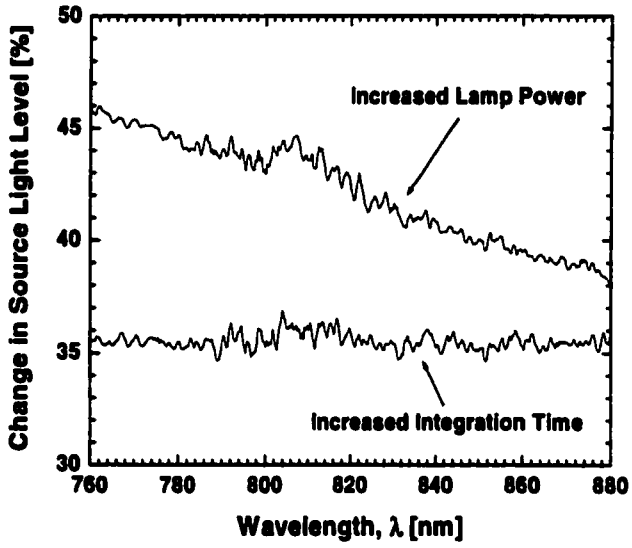

Fig. 8.15. The equivalent change in the light source intensity for the lamp power (t = 5 min.) and integration time changes (t = 12 min.) of Fig. 8.13, compared with baseline at t = 1 min.

A more challenging scenario is presented in Fig. 8.16, which shows the effect of raising the temperature of the light source housing from 44.4 C to 48.9 C. The intensity-feedback light intensity controller was disabled for this experiment to allow the spectral characteristics of the light source to drift. The minor effect of this change on the SPR spectrum is shown in Fig. 8.17. The change in the light source spectral intensity is illustrated by Fig. 8.18, and shows an overall decrease in light intensity combined with a blue-shift of the lamp emission, so the intensity of shorter wavelengths has decreased less than longer wavelengths. Again, using Table 8.1, we expect the lamp power change to have a effect combining a uniform decrease in intensity and a linear decrease in intensity with wavelength. The latter effect will cause an increase in the resonant position calculated by the tracking centroid

algorithm. The effect of both factors on the simple centroid is to increase the calculated resonant wavelength.

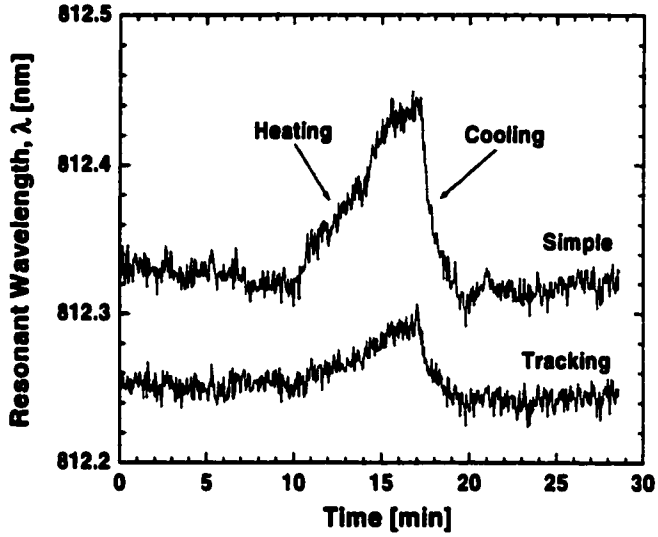

Fig. 8.16. Effect of heating the light source housing from 44.4 C to 48.9 C on the measured SPR wavelength calculated by the simple centroid and tracking centroid algorithms.

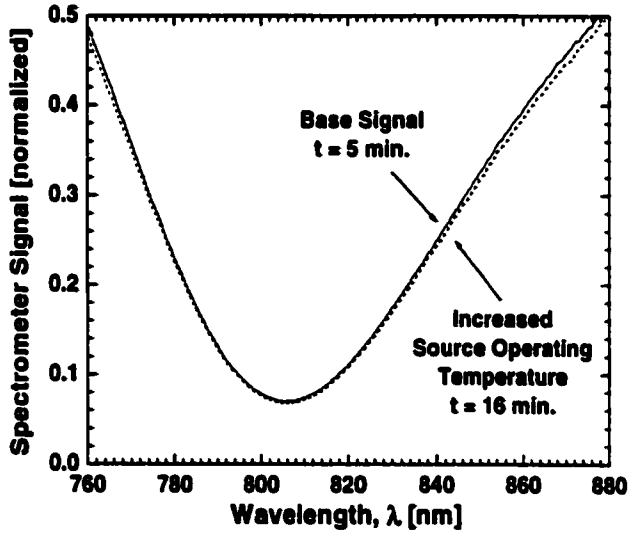

Fig. 8.17. Spectral change corresponding to the light source housing temperature changes of Fig. 8.16.

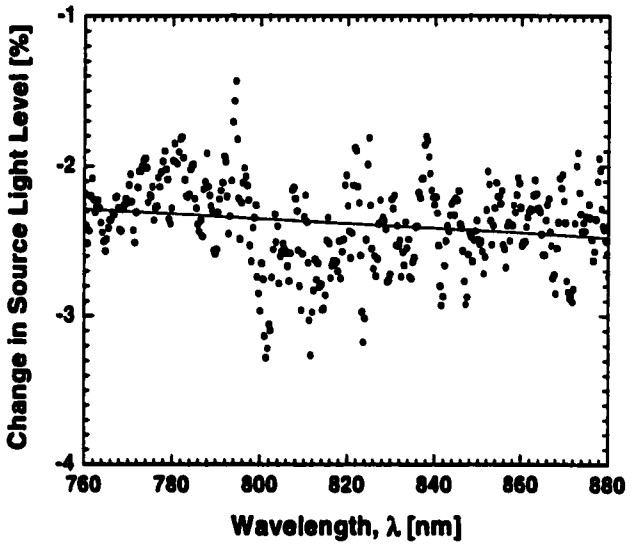

Fig. 8.18. The change in the light source intensity for the light source housing temperature changes of Fig. 8.16 from t = 5 min. to t = 16 min.

8.5 Discussion

In this chapter, we have presented methods for the objective evaluation of SPR data processing algorithms. By evaluating the noise level, linearity, and immunity from common sources of drift of several algorithms, the most effective algorithm for a given experimental system can be determined.

Using these methods of evaluation, the interpolated tracking centroid was shown to be superior to the simple centroid algorithm in terms of noise level, linearity, and reduced susceptibility to common sources of spectral drift. While the improvements in noise level and linearity are minimal, the interpolated tracking centroid algorithm is far more immune from spectral changes than the simple centroid algorithm and represents a substantial improvement in the quality of the data produced.

Notes for Chapter 8

[1] K. Johansen, I. Lundström, B. Liedberg, Sensitivity deviation: instrumental linearity errors that influence concentration analyses and kinetic evaluation of biomolecular interactions, Biosensors and Bioelectronics 15 (2000) 503-509.

[2] T. M. Chinowsky, L.S. Jung, S.S. Yee, Optimal linear data analysis for surface plasmon resonance biosensors, Sensors and Actuators B 54 (1999) 89-97.

[3] K.S. Johnston, K.S. Booksh, T. M. Chinowsky, S.S. Yee, Performance comparison between high and low resolution spectrophotometers used in a white light surface plasmon resonance sensor, Sensors and Actuators B 54 (1999) 80-88.

[4] K. Johansen, R. Stålberg, I. Lundström, B. Liedberg, Surface plasmon resonance: instrumental resolution using photo diode arrays, Measurement Science and Technology 11 (2000) 1630-1638.

[5] B.E.A. Saleh, M.C. Teich, Fundamentals of Photonics, John Wiley & Sons, New York, 1991.

[6] A. Papoulis, Probability, Random Variables, and Stochastic Processes, McGraw-Hill, Inc., New York, 1991.

[7] G.G. Nenninger, J.B. Clendenning, C.E. Furlong, S.S. Yee, Reference-compensated biosensing using a dual-channel surface plasmon resonance sensor system based on a planar lightpipe configuration, Sensors and Actuators B 51 (1998) 38-45.

[8] J. Homola, H.B. Lu, G.G. Nenninger, S.S. Yee, C.T. Campbell, Novel approach to multichannel SPR sensing, Proceedings of the SPIE Conference on Microsensors and Applications II, SPIE 3857 (1999) 198-206.

[9] D.G. Myszka, Improving biosensor analysis, Journal of Molecular Recognition 12 (1999) 279-284.

[10] J. Homola, H.B. Lu, G.G. Nenninger, J. Dostálek, S.S. Yee, A novel multichannel surface plasmon resonance biosensor, Sensors and Actuators B 76 (2001) 403-410.

Chapter 9: Future Work

Future work for improving the resolution of surface plasmon resonance sensors will likely involve a number of parallel efforts, with improvements made to the sensor chip design and manufacturing quality, the instrumentation system, and the data analysis methods. We therefore propose the following approach to future improvements in surface plasmon resonance sensor resolution:

9.1 Long-Range Surface Plasma Wave Sensor Chip Improvements

Materials and processing improvements will be a key part of future development of long-range surface plasma wave (LRSPW) sensors. In particular, a method for increasing the adhesion of the gold layer to the fluoropolymer buffer layer would be a key improvement to the robustness of the sensor chips. The adhesion of the buffer layer and the quality of the final sensor surface should also be studied and optimized.

Further exploration of alternate buffer materials would also be useful. For instance, certain grades of CYTOP fluoropolymer contain an adhesion promoter and therefore could be applied to the glass substrate without silane pretreatment, reducing the number of processing steps required. Accurate spin curves, both for Teflon AF and for any alternate fluoropolymer, need to be produced to ensure the repeatability of sensor chip manufacturing as well as the accuracy of theoretical predictions of sensor performance.

Improved modeling accuracy of the Teflon AF-based LRSPW sensor could be achieved with more complete measurements of the refractive index of Teflon AF 1600-series fluoropolymer, especially in the infrared region. Refractive index measurements of the refractive index of CYTOP fluoropolymer from 500 to 1000 nm are also required if CYTOP is to be evaluated as a buffer material. In addition, a thorough evaluation of refractive index data for water and gold is needed, as there is a

significant variation among published refractive index models for both water and gold. New refractive index models for the materials actually used in the sensor construction and experiments would further improve the modeling accuracy.

Ultimately, a combination of improved sensor design and modeling tools, together with better process information and control would allow for the production of optimized LRSPW sensor chips. These sensors would provide the highest resolution by using the best combination of narrow resonance width and high sensitivity.

9.2 Long-Range Surface Plasma Wave Sensor Instrumentation Improvements

The most significant improvement to the long-range surface plasma wave sensor instrumentation would come from the implementation of multiple sensor channels. Research in conventional surface plasmon resonance biosensors has demonstrated the need for stable and accurate reference sensor channels. These reference channels have used parallel or overlayer architectures, both of which are technically feasible for LRSPW sensors. The design and implementation of a parallel channel architecture for LRSPW sensors will be challenging due to a limited light budget, resulting primarily from the need to maximize the angular and wavelength resolution of the light detected by the spectrometer. Proper selection of optical components and spectrometer performance will allow for sufficient light levels with sufficient wavelength resolution to measure narrow LRSPW resonance minima.

A dramatic decrease in the detector noise levels can be achieved by the use of a photodiode array detector instead of a CCD detector. However, the light sensitivity of a photodiode array detector is less than that of a CCD detector, requiring that light levels through the sensor instrumentation be as high as possible. Therefore, improving the light levels through the LRSPW sensor system could make the use of the photodiode array practical.

9.3 Data Analysis Improvements

The evaluation of other data processing algorithms using the methods described in this work would be extremely useful in designing an algorithm with the best overall performance for the system being studied. In particular, evaluation of the robustness of the various methods under non-ideal conditions, such as environmental drift or light level changes, could lead to improved methods producing higher-quality data.

The use of real-time referencing and dark current correction will help to reduce the complex effects of environmental drift such as temperature changes, perhaps providing better compensation using a reference channel.

Chapter 10: Conclusion

We have presented the design, modeling, and implementation of an improved surface plasmon resonance (SPR) biosensor based on long-range surface plasma wave (LRSPW) spectroscopy. The LRSPW sensor has improved resolution over conventional SPR due to a narrower absorption minimum in the sensor spectral response and increased sensitivity to changes in the refractive index of the analyte.

Theoretical design curves presented for an LRSPW sensor using a Teflon AF buffer layer and gold metal layer predict that the sensor can have sensitivity as high as 1×10^{5} nm RIU^{-1}, an order of magnitude or more improvement over conventional SPR sensors. Results of a biosensing experiment conducted with the LRSPW sensor showed a resonance width of only 15 nm (full-width at half-minimum), a sensitivity of 3.1×10^{4} nm RIU^{-1}, and a corresponding resolution of 1.9×10^{-7} RIU. Compared with a similar experiment conducted using a conventional SPR sensor, the LRSPW sensor had 25 times better resolution.

We have also presented methods for evaluating the performance of data-processing algorithms for analyzing SPR spectra, including a method for predicting the instrument resolution based on measured system and detector noise. A new interpolated tracking centroid data-processing algorithm was described, and its performance in terms of resolution, linearity, and resistance to environmental drift was shown to be superior to that of a simple centroid algorithm.

Bibliography

Asahi Glass Company, CYTOP Amorphous Fluorocarbon Polymer Technical Information.

Asahi Glass Company, ARCTOP anti-reflection film, http://www.agc.co.jp.

R. Altkorn, I. Koev, M.J. Pelletier, Raman Performance Characteristics of Teflon-AF 2400 Liquid-Core Optical-Fiber Sample Cells, Applied Spectroscopy 53 (1999) 1169-1176.

D.E. Aspnes, Fourier transform detection system for rotating-analyzer ellipsometers, Optics Communications 8 (1973) 222-225.

M. Bass (ed.), Handbook of Optics, McGraw-Hill, New York, 1995, Ch. 33.

N. Bazin, J.E. Andrew, H.A. McInnes, Formation of Teflon AF Polymer Thin Films as Optical Coatings in the High Peak Power Laser Field, Proceedings of the SPIE 3492 (1999) 964-969.

J.J. Burke, G.I. Stegeman, T. Tamir, Surface-polariton-like waves guided by thin, lossy metal films, Physical Review B 33 (1986) 5186-5201.

T.M. Chinowsky, L.S. Jung, S.S. Yee, Optimal linear data analysis for surface plasmon resonance biosensors, Sensors and Actuators B 54 (1999) 89-97.

J. Čtroký, J. Homola, P.V. Lambeck, S. Musa, H.J.W.M. Hoekstra, R.D. Harris, J.S. Wilkinson, B. Usievich, N.M. Lyndin, Theory and modelling of optical waveguide sensors utilising surface plasmon resonance, Sensors and Actuators B 54 (1999) 66-73.

A.W. Drake, Fundamentals of Applied Probability Theory. McGraw-Hill Book Company, New York, 1967.

DuPont Fluoroproducts, Adhesion Information for Teflon AF, Teflon AF Amorphous Fluoropolymers Product Information, H-44585-3 (1998).

DuPont Fluoroproducts, Properties of Amorphous Fluoropolymers Based on 2,2-Bistrifluoromethyl-4,5-Difluoro-1,3-Dioxole, H-5245-2 (1997).

E. Hecht, Optics, Addison-Wesley Publishing Company, Reading, MA, 1987.

J. Homola, S.S. Yee, G. Gauglitz, Surface plasmon resonance sensors: review, Sensors and Actuators B 54 (1999) 3-15.

J. Homola, H.B. Lu, S.S. Yee, Dual-channel surface plasmon resonance sensor with spectral discrimination of sensing channels using dielectric overlayer, Electronics Letters 35 (1999) 1105-1106.

J. Homola, H.B. Lu, G.G. Nenninger, S.S. Yee, C.T. Campbell, Novel approach to multichannel SPR sensing, SPIE Conference on Microsensors and Applications II, Proceedings of the SPIE 3857 (1999) 198-206.

J. Homola, University of Washington Department of Electrical Engineering, personal communication, 2000.

J. Homola, H.B. Lu, G.G. Nenninger, J. Dostálek, S.S. Yee, A novel multichannel surface plasmon resonance biosensor, Sensors and Actuators B 76 (2001) 403-410.

P.D.T. Huibers, Models for the wavelength dependence of the index of refraction of water, Applied Optics 36 (1997) 3785-3787.

J.D. Jackson, Classical Electrodynamics. Wiley, New York, 1975.

K. Johansen, R. Stålberg, I. Lundström, B. Liedberg, Surface plasmon resonance: instrumental resolution using photo diode arrays, Measurement Science and Technology 11 (2000) 1630-1638.

K. Johansen, I. Lundström, B. Liedberg, Sensitivity deviation: instrumental linearity errors that influence concentration analyses and kinetic evaluation of biomolecular interactions, Biosensors and Bioelectronics 15 (2000) 503-509.

K.S. Johnston, K.S. Booksh, T.M. Chinowsky, S.S. Yee, Performance comparison between high and low resolution spectrophotometers used in a white light surface plasmon resonance sensor, Sensors and Actuators B 54 (1999) 80-88.

R.C. Jorgenson, S.S. Yee, A fiber-optic chemical sensor based on surface plasmon resonance, Sensors and Actuators B 12 (1993) 213-220.

P. J. Kajenski, Tunable optical filter using long-range surface plasmons, Optical Engineering 36 (1997) 1537-1541.

E. Kaltenbacher, E.T. Steimle, R.H. Byrne, A compact, in-situ, spectrophotometric sensor for aqueous environments: design and applications, IEEE Proceedings of the 2000 International Symposium on Underwater Technology, Tokyo, Japan, May 23-26, 2000.

R. Karlsson, R. Stahlberg, Surface Plasmon Resonance Detection and Multispot Sensing for Direct Monitoring of Interactions Involving Low-Molecular-Weight Analytes and for Determination of Low Affinities, Analytical Biochemistry 228 (1995) 274-280.

M. Khoo, Process Instructions: Teflon AF1601S-40, Micro Actuators, Sensors and Systems Group, University of Illinois at Urbana-Champaign, http://mass.micro.uiuc.edu/.

E. Kretschmann, H. Raether, Radiative decay of non-radiative surface plasmons excited by light, Zeitschrift für Naturforsch 23A (1968) 398-410.

E. Kretschmann, Die bestimmung optisher konstanten von metallen durch anregung von oberflächenplasmaschwingungen, Zeitschrift für Physik 241 (1971) 313-324.

A.A. Kruchinin, Y.G. Vlasov, Surface plasmon resonance monitoring by means of polarization state measurement in reflected light as the basis of a DNA probe biosensor, Sensors and Actuators B 30 (1996) 77-80.

K. Kukanskis, J. Elkind, J. Melendez, T. Murphy, G. Miller, Detection of DNA hybridization using the TISPR-1 surface plasmon resonance biosensor, Analytical Biochemistry 274 (1999) 7-17.

S.P. Langley, C.G. Abbot, Annals of the Astrophysical Observatory of the Smithsonian Institution, U.S. Government Printing Office, Washington, 1900, p. 253-254.

B. Liedberg, C. Nylander, I. Lundström, Surface plasmon resonance for gas detection and biosensing, Sensors and Actuators 4 (1995) 299-304.

J.H. Lowry, J.S. Mendlowitz, N.S. Subramanian, Optical characteristics of Teflon AF fluoroplastic materials, Optical Engineering 31 (1992) 1982-1984.

N.M. Lyndin, I.F. Salakhutdinov, V.A. Sychugov, B.A. Usievich, F.A. Pudonin, O. Parriaux, Long-range surface plasmons in asymmetric layered metal-dielectric structures, Sensors and Actuators B 54 (1999) 37-42.

A. Macleod, Thin film optical materials, in A.A. Elshabini-Riad, F.D. Barlow III (eds.), Thin Film Technology Handbook, McGraw-Hill, New York, 1998, Ch. 8, pp. 1-41.

K. Matsubara, S. Kawata, S. Minami, Optical chemical sensor based on surface plasmon measurement, Applied Optics 27 (1988) 1160-1163.

K. Matsubara, S. Kawata, S. Minami, Multilayer system for a high-precision surface plasmon resonance sensor, Optics Letters 15 (1990) 75-77.

W.M. Mullet, E.P.C. Lai, J.M. Yeung, Surface Plasmon Resonance-Based Immunoassays, Methods 22 (2000) 77-91.

D.G. Myszka, Kinetic analysis of macromolecular interactions using surface plasmon resonance biosensors, Current Opinions in Biotechnology 8 (1997) 50-57.

D.G. Myszka, Survey of the 1998 optical biosensor literature, Journal of Molecular Recognition 12 (1999) 390-408.

D.G. Myszka, Improving biosensor analysis, Journal of Molecular Recognition 12 (1999) 279-284.

D.G. Myzka, R.L. Rich, Implementing surface plasmon resonance biosensors in drug discovery, Pharmaceutical Science and Technology Today 3 (2000) 310-317.

S.G. Nelson, K.S Johnston, S.S. Yee, High sensitivity surface plasmon resonance sensor based on phase detection, Sensors and Actuators B 35, (1996) 187-191.

G.G. Nenninger, Referenced Surface Plasmon Resonance Biosensor Using a Dual-Channel Planar Lightpipe, M.S. Thesis, University of Washington Department of Electrical Engineering (1998).

G.G. Nenninger, J.B. Clendenning, C.E. Furlong, S.S. Yee, Reference-compensated biosensing using a dual-channel surface plasmon resonance sensor system based on a planar lightpipe configuration, Sensors and Actuators B 51 (1998) 38-45.

G.G. Nenninger, P. Tobiška, J. Homola, S.S. Yee, Long-range surface plasmons for high-resolution surface plasmon resonance sensor, Sensors and Actuators B 74 (2001) 145-151.

P.I. Nikitin, A.A. Belaglazov, V.E. Kochergin, M.V. Valeiko, T.I. Kzenevich, Surface plasmon resonance interferometry for biological and chemical sensing, Sensors and Actuators B 54 (1999) 43-50.

C. Nylander, B. Liedberg, T. Lind, Gas detection by means of surface plasmon resonance, Sensors and Actuators 3 (1982) 79-88.

A. Otto, Excitation of nonradiative surface plasma waves in silver by the method of frustrated total reflection, Zeitschrift für Physik 216 (1968) 398-410.

J.I. Pankove, Optical Processes in Semiconductors, Dover Publications, New York, 1985.

A. Papoulis, Probability, Random Variables, and Stochastic Processes, McGraw-Hill, Inc., New York, 1991.

C. Plumereau, A. Bouchoux, A. Cachard, Electrooptic light modulator using long-range surface plasmons, Novel Optoelectronic Devices, Proceedings of the SPIE 800 (1987) 79-83.

J.C. Quail, J.G. Rako, H.J. Simon, Long-range surface-plasmon modes in silver and aluminum films, Optics Letters 8 (1983) 377-379.

R.L. Rich, D.G. Myszka, Survey of the 1999 surface plasmon resonance biosensor literature, Journal of Molecular Recognition 13 (2000) 388-407.

B.E.A. Saleh, M.C. Teich, Fundamentals of Photonics, John Wiley & Sons, New York, 1991.

D. Sarid, Long-range surface-plasma waves in very thin metal films, Physical Review Letters 47 (1981) 1927-1930.

P. Scheibener, J. Strab, J.M.H. Levelt Sengers, J.S. Gallagher, Refractive Index of Water and Steam as Function of Wavelength, Temperature and Density, Journal of Physical and Chemical Reference Data 19 (1990) 677-716.

J.S. Schildkraut, Long-range surface plasmon electrooptic modulator, Applied Optics, 27 (1988) 4587-4590.

Schott Glass Technologies, Schott Optical Glass, Schott Glass Technologies, Inc., Duryea, PA, 1992.

S. Sjölander, C. Urbaniczky, Integrated fluid handling system for biomolecular interaction analysis, Analytical Chemistry 63 (1991) 2338-2345.

G.I. Stegeman, J.J. Burke, D.G. Hall, Nonlinear optics of long-range surface plasmons, Applied Physics Letters 41 (1982) 906-908.

E. Stenberg, B. Persson, H. Roos, C. Urbaniczky, Quantitative determination of surface concentration of protein with surface plasmon resonance using radiolabeled proteins, Journal of Colloid and Interface Science 143 (1991) 513-526.

N. Sugiyama, Perfluoropolymers Obtained by Cyclopolymerization and Their Applications, in J. Scheirs (ed.), Modern Fluoropolymers, John Wiley and Sons, Ltd., New York, 1997, Ch. 28.

R.W. Waynant, M.N. Ediger (eds.), Electro-Optics Handbook, McGraw-Hill, Inc., New York, 1994, Ch. 11.

L. Wendler, R. Haupt, An improved virtual mode theory of ATR experiments on surface polaritons, Physica Status Solidi B 143 (1987) 131-148.

R.K. Yonkoski, D.S. Soane, Model for spin coating in microelectronic applications, Journal of Applied Physics 72 (1992) 725-740.

Y.G. Zhao, W.K. Lu, Y. Ma, S.S. Kim, S.T. Ho, T.J. Marks, Polymer waveguides useful over a very wide wavelength range from the ultraviolet to infrared, Applied Physics Letters 77 (2000) 2961-2963.

VITA

GARET GLENN NENNINGER

EDUCATION:

University of Washington — Seattle, Washington
Department of Electrical Engineering
Master of Science in Electrical Engineering, June 1998.

Massachusetts Institute of Technology — Cambridge, MA
Department of Electrical Engineering
Bachelor of Science in Electrical Engineering, Minor in Political Science, June 1991.

EXPERIENCE:

SonoSite, Inc. — Bothell, Washington
June 2001 – Present
Systems Engineer, Product Development Division.

Department of Electrical Engineering, University of Washington — Seattle, Washington
August 1996 – August 2001
Research Assistant responsible for developing and testing new optically-interrogated biological and chemical sensors based on surface plasmon resonance.

Naval Nuclear Propulsion Program Headquarters — Arlington, Virginia
June 1991 – July 1996
Lieutenant, United States Navy. Lead Instrumentation and Control Engineer in the New Submarine Design Branch.

MIT Lincoln Laboratory — Lexington, Massachusetts
September 1990 – June 1991
Research Assistant responsible for designing diffractive microlens arrays for a laser beam-steering system.